

# Search for displaced leptons

## Dissertation

Presented in Partial Fulfillment of the Requirements for the Degree  
Doctor of Philosophy in the Graduate School of The Ohio State  
University

By

Bryan Cardwell, B.S., M.S.

Graduate Program in Physics

The Ohio State University

2021

Dissertation Committee:

Christopher Hill, Advisor

Stanley Durkin

Linda Carpenter

Andrew Heckler

© Copyright by

Bryan Cardwell

2021

## **Abstract**

Search for displaced leptons

For Cristiana and Montague.

## Acknowledgments

## Vita

2015 .....	B.S. Physics, North Central College
2015-2017 .....	Graduate Teaching Associate, The Ohio State University
2017 .....	M.S. Physics, The Ohio State University
2017-present .....	Graduate Research Associate, The Ohio State University

## Publications

### Research Publications

Included in author list of **FIXME** publications from CMS.

## Fields of Study

Major Field: Physics

## Table of Contents

	Page
Abstract . . . . .	ii
Dedication . . . . .	iii
Acknowledgments . . . . .	iv
Vita . . . . .	v
List of Tables . . . . .	ix
List of Figures . . . . .	xii
1. Introduction . . . . .	1
1.1 The Standard Model . . . . .	1
1.1.1 Quantum chromodynamics . . . . .	3
1.1.2 The electroweak theory . . . . .	3
1.1.3 The Higgs mechanism . . . . .	4
1.1.4 Current status . . . . .	6
1.2 Beyond the Standard Model . . . . .	8
1.2.1 Supersymmetry . . . . .	8
1.2.2 Long-lived particles . . . . .	10
1.2.3 Displaced supersymmetry . . . . .	12
2. The Large Hadron Collider and Compact Muon Solenoid experiment . .	13
2.1 The Large Hadron Collider . . . . .	13
2.1.1 Injection chain . . . . .	14
2.1.2 Main ring . . . . .	15
2.2 The Compact Muon Solenoid experiment . . . . .	19
2.2.1 Solenoid magnet . . . . .	21

2.2.2	Tracker . . . . .	22
2.2.3	Electromagnetic calorimeter . . . . .	25
2.2.4	Hadronic calorimeter . . . . .	27
2.2.5	Muon system . . . . .	28
2.2.6	Trigger . . . . .	31
2.2.7	Physics object reconstruction . . . . .	31
3.	Search for displaced leptons . . . . .	36
3.1	Overview . . . . .	36
3.2	Data and simulated samples . . . . .	37
3.2.1	Experimental data . . . . .	37
3.2.2	Simulated background events . . . . .	37
3.2.3	Simulated signal events . . . . .	38
3.3	Event selection . . . . .	40
3.3.1	Triggers . . . . .	40
3.3.2	Preselection . . . . .	42
3.3.3	Prompt control region . . . . .	51
3.3.4	Inclusive signal region . . . . .	52
3.4	Background estimation . . . . .	56
3.4.1	Background sources . . . . .	56
3.4.2	Data-driven ABCD method . . . . .	58
3.4.3	Closure tests in control regions . . . . .	61
3.4.4	ABCD correction and systematic uncertainty . . . . .	63
3.4.5	Testing full background estimation procedure . . . . .	68
3.4.6	Additional background checks . . . . .	68
3.5	Corrections to simulation . . . . .	74
3.5.1	Event pileup . . . . .	74
3.5.2	Lepton ID . . . . .	74
3.5.3	Lepton $d_0$ resolution . . . . .	74
3.5.4	Trigger efficiency . . . . .	79
3.6	Systematic uncertainties . . . . .	80
3.6.1	Integrated luminosity . . . . .	80
3.6.2	Pileup . . . . .	80
3.6.3	Trigger efficiency . . . . .	80
3.6.4	Lepton ID and isolation . . . . .	82
3.6.5	Muon pixel hit efficiency . . . . .	82
3.6.6	Lepton $d_0$ resolution . . . . .	83
3.6.7	Summary of systematic uncertainties in the signal efficiency . . . . .	84
3.7	Results . . . . .	85
3.7.1	Observed events . . . . .	87
3.7.2	Limits . . . . .	88

3.7.3	Additional likelihood tests . . . . .	89
4.	Conclusion . . . . .	103
Appendices		104
A.	Impact of APV saturation on displaced tracking . . . . .	104
B.	Poorly measured lepton $ d_0 $ at large $ \eta $ . . . . .	105
C.	Displaced tracking efficiency . . . . .	107
Bibliography . . . . .		108

## List of Tables

<b>Table</b>	<b>Page</b>
2.1 Luminosity parameters used in Eq. (2.1). . . . .	16
3.1 The $e\mu$ preselection criteria. The electron and muon $p_T$ thresholds increased in 2017 because the HLT electron and muon $p_T$ thresholds increased. . . . .	43
3.2 The ee preselection criteria. The electron $p_T$ threshold increased in 2017 and 2018 because the HLT electron $p_T$ threshold increased at the start of 2017. . . . .	44
3.3 The $\mu\mu$ preselection criteria. The muon $p_T$ threshold increased in 2017 and 2018 because the HLT muon $p_T$ threshold increased at the start of 2017. . . . .	45
3.4 The electron tight ID requirements. They are identical to the tight cut-based ID from the egamma POG, except we remove any requirements on $d_0$ or the longitudinal impact parameter [27]. . . . .	46
3.5 The muon tight ID requirements. They are identical to the tight cut-based ID from the muon Physics Object Group, except we remove any requirements on $d_0$ or $d_z$ [41]. . . . .	47
3.6 Closure test results in background simulation (with and without $Z \rightarrow \tau\tau \rightarrow ll$ events) and in data, in the 100–500 $\mu\text{m}$ region. The average extrapolated ratios and their statistical uncertainties are given. The A, B, C, and D regions are defined as follows: A is 20–30 $\mu\text{m}$ in prompt lepton $ d_0 $ and 20–100 $\mu\text{m}$ in displaced lepton $ d_0 $ , B is 20–30 $\mu\text{m}$ in prompt-lepton $ d_0 $ and 100–500 $\mu\text{m}$ in displaced lepton $ d_0 $ , C is always 20–100 $\mu\text{m}$ in displaced lepton $ d_0 $ , D (the test region) is always 100–500 $\mu\text{m}$ in displaced lepton $ d_0 $ , and we perform repeated tests while simultaneously varying the C and D prompt lepton $ d_0 $ s within the 30–100 $\mu\text{m}$ range.	62

3.7 Closure test results in in data and background simulation (with and without $Z \rightarrow \tau\tau \rightarrow ll$ events), in the $500 \mu\text{m}$ – $10 \text{ cm}$ region. The ratios of the actual yield to the estimated yield and their statistical uncertainties are given. The A, B, C, and D regions are defined as follows: A is $20$ – $30 \mu\text{m}$ in prompt lepton $ d_0 $ and $20$ – $100 \mu\text{m}$ in displaced lepton $ d_0 $ , B is $20$ – $30 \mu\text{m}$ in prompt lepton $ d_0 $ and $500 \mu\text{m}$ – $10 \text{ cm}$ in displaced lepton $ d_0 $ , C is $30$ – $100 \mu\text{m}$ in prompt lepton $ d_0 $ and $20$ – $100 \mu\text{m}$ in displaced lepton $ d_0 $ , and D (the test region) is $30$ – $100 \mu\text{m}$ in prompt lepton $ d_0 $ and $500 \mu\text{m}$ – $10 \text{ cm}$ in displaced lepton $ d_0 $ . . . . .	95
3.8 The correction factors and the uncorrected and corrected background estimates in SR I. The correction factor uncertainty includes both the uncertainty in the average and the additional uncertainty obtained from varying the fit extrapolation point. The total uncertainty (statistical plus systematic) is given for the corrected background estimate.	96
3.9 The systematic uncertainty and the background estimates in SRs II, III, and IV. The total uncertainty (statistical plus systematic) is given for each estimate. . . . .	96
3.10 Closure test results in background simulation in the SRs, with the correction applied. The estimated number of events, the actual number of events, and their total uncertainties (statistical plus systematic) are given. For cases where an uncertainty is not listed, it is negligibly small ( $<0.005$ ). . . . .	97
3.11 Some properties of the seven events found in data with the material interactions selection inverted. . . . .	97
3.12 Background estimates in data while applying the 2018 $\mu\mu$ preselection and the additional requirement of at least one medium $b$ -tagged jet. The estimates with at least one $b$ jet are about an order of magnitude below the nominal prediction. . . . .	98
3.13 A closure test of the ABCD method in 2018 QCD simulation in the $\mu\mu$ channel with the muon isolation criterion inverted. The estimates from the ABCD method, the actual yields in simulation, and the ratios of the actual to the estimated yields are shown. . . . .	98

3.14 The average $\sigma_{align}$ for electrons and muons, for the 2017 and 2018 analyses. . . . .	98
3.15 The unprescaled MET triggers used to create an orthogonal data sample for the trigger efficiency calculation. . . . .	99
3.16 Systematic uncertainties in the signal efficiency for all three years and the three channels. The mean is provided in cases where the uncertainty varies by signal sample. Uncertainties in the same row are treated as correlated among the years of data taking, except for the displaced tracking and muon pixel hit efficiencies, where the 2016 uncertainty is treated as uncorrelated with the 2017 and 2018 uncertainties.	100
3.17 The number of estimated background and observed events in each channel and SR. For each estimate, the total uncertainty is given. . . . .	101
3.18 The pre- and post-fit predictions for each signal region bin. . . . .	102

## List of Figures

Figure	Page
1.1 The SM particle content. . . . .	2
1.2 Higgs mass (left) corrected by fermion loop and fermion mass (right) corrected by photon loop. . . . .	8
1.3 Corrections to the Higgs boson mass from the top quark (left) and top squark (right) cancel in exact SUSY. The top quark and top squark contributions are enhanced by the large top–Higgs coupling. . . . .	9
1.4 Long-lived decays of the neutron (left) and muon (right). . . . .	10
2.1 Layout of the LHC experiments [30]. . . . .	14
2.2 A diagram of the CERN accelerator complex. The analysis presented in Chapter 3 utilizes protons accelerated by LINAC 2, BOOSTER (also known as PSB), PS, SPS, and finally the LHC before their ultimate collision inside CMS [40]. . . . .	15
2.3 The peak instantaneous (top) and integrated (bottom) luminosity delivered by the LHC during proton operation between 2011 and 2018 [54]. . . . .	17
2.4 Diagram of an LHC dipole magnet in cross-section [52]. . . . .	18
2.5 The CMS detector [44]. . . . .	20
2.6 Left: the stored-energy-over-mass ratio E/M, for several detector magnets. Right: cross section of the four-layer winding of reinforced conductor in the CMS superconducting solenoid [18]. . . . .	22

2.7	Comparison of the original and Phase-1 CMS pixel detector layouts in $y - z$ plane [7]. . . . .	24
2.8	Layout of the CMS silicon tracker. TIB, TOB, TID, and TEC refer to subdetectors of the strip detector while PIXEL refers to the original pixel detector. The Phase-1 pixel detector is contained within the same volume [18]. . . . .	25
2.9	The observed local p-value for the five decay modes and the overall combination as a function of the SM Higgs boson mass showing the importance of the ECAL mass resolution in the discovery of the Higgs boson with the CMS experiment. The dashed line shows the expected local p-values for a SM Higgs boson with a mass $m_H$ [19]. . . . .	26
2.10	Layout of the hadron calorimeter barrel (HB), outer (HO), endcap (HE), and forward (HF) subdetectors [18]. . . . .	28
2.11	Muon momentum resolution as a function of momentum using the CMS muon system, the CMS inner tracker, and the combination of the two subdetectors in two different $\eta$ ranges [15]. . . . .	29
2.12	Sketch of a CMS muon system drift cell showing drift lines and isochrones. The plates at the top and bottom of the cell are at ground potential while the voltages applied to the electrodes are +3600 V for wires, 1800 V for strips, and -1200 V for cathodes [18]. . . . .	30
2.13	A sketch of a transverse slice of the CMS detector showing representative particle interactions [45]. . . . .	35
3.1	The muon isolation pileup correction term, for the standard muon isolation and the modified muon isolation in simulated $t\bar{t}$ events that pass the $e\mu$ preselection in 2018 conditions. The plot on the left is for muon $ d_0  < 100 \mu\text{m}$ , and the plot on the right is for muon $500 <  d_0  < 1000 \mu\text{m}$ . . . . .	48
3.2	The electron $ d_0 $ versus the muon $ d_0 $ , for $t\bar{t}$ simulated events that pass the $e\mu$ preselection and where at least one lepton comes from a heavy-flavor meson. The plot on the left uses the standard isolation, and the plot on the right uses the modified isolation. . . . .	49

3.3	The muon custom isolation distribution for $t\bar{t}$ background simulation and signal simulation in 2018 conditions. . . . .	49
3.4	The lepton $p_T$ (upper), $\eta$ (middle), and $ d_0 $ (lower) distributions in the $e\mu$ prompt control region, for electrons (left) and muons (right), for 2016 data and MC simulation. The rightmost bin in each plot contains the overflow entries. . . . .	53
3.5	The electron $p_T$ (left), $\eta$ (lower), and $ d_0 $ (right) distributions in the ee prompt control region for 2016 data and MC simulation. The rightmost bin in each plot contains the overflow entries. . . . .	54
3.6	The muon $p_T$ (left), $\eta$ (lower), and $ d_0 $ (right) distributions in the $\mu\mu$ prompt control region for 2016 data and MC simulation. The rightmost bin in each plot contains the overflow entries. . . . .	55
3.7	The fraction of electrons (left) and muons (right) from different parents as a function of lepton $ d_0 $ , for simulated $t\bar{t}$ events that pass the 2018 $e\mu$ channel preselection. . . . .	57
3.8	The fraction of muons from different parents as a function of muon $ d_0 $ , for simulated DY events that pass the 2018 $\mu\mu$ channel preselection. . . . .	58
3.9	A diagram of the ABCD method overlaid on simulated background events passing the 2018 $e\mu$ preselection. A, B, and C are control regions, and D is the inclusive SR, which includes SRs I, II, III, and IV. Underflow events are included in the bins along the left and bottom edges. . . . .	59
3.10	Background estimation closure tests in data, in the one-prompt (20–100 $\mu\text{m}$ )/one-displaced (100–500 $\mu\text{m}$ ) sidebands, in the $e\mu$ channel. The prompt leading electron/ displaced leading muon sideband is shown in the upper row, and the prompt leading muon/ displaced leading electron sideband is shown in the lower row. The plots on the left show the results for 2016 data, and the plots on the right are for combined 2017 and 2018 data. The plots show the ratio of the actual to the estimated number of events as a function of the prompt lepton $ d_0 $ . The data are fitted with a straight line, where the slope and y-intercept are allowed to vary. The $1\sigma$ and $2\sigma$ confidence intervals are shown in the green and yellow bands, respectively. . . . .	65

3.11 Background estimation closure tests in data, in the one-prompt (20–100 $\mu\text{m}$ )/one-displaced (100–500 $\mu\text{m}$ ) sidebands, in the ee channel. The prompt leading electron/ displaced subleading electron sideband is shown in the upper row, and the prompt subleading electron/ displaced leading electron sideband is shown in the lower row. The plots on the left show the results for 2016 data, and the plots on the right are for combined 2017 and 2018 data. The plots show the ratio of the actual to the estimated number of events as a function of the prompt lepton $ d_0 $ . The data are fitted with a straight line, where the slope and y-intercept are allowed to vary. The $1\sigma$ and $2\sigma$ confidence intervals are shown in the green and yellow bands, respectively. . . . .	66
3.12 Background estimation closure tests in data, in the one-prompt (20–100 $\mu\text{m}$ )/one-displaced (100–500 $\mu\text{m}$ ) sidebands, in the $\mu\mu$ channel. The prompt leading muon/ displaced subleading muon sideband is shown in the upper row, and the prompt subleading muon/ displaced leading muon sideband is shown in the lower row. The plots on the left show the results for 2016 data, and the plots on the right are for combined 2017 and 2018 data. The plots show the ratio of the actual to the estimated number of events as a function of the prompt lepton $ d_0 $ . The data are fitted with a straight line, where the slope and y-intercept are allowed to vary. The $1\sigma$ and $2\sigma$ confidence intervals are shown in the green and yellow bands, respectively. . . . .	67
3.13 The dimuon invariant mass distribution in the $\mu\mu$ channel with the muon isolation criterion inverted, for 2018 data and QCD simulation. . . . .	71
3.14 The dimuon invariant mass distribution in 2018 data in the $\mu\mu$ channel, in the prompt control region (black), SR I (blue), SR IV (red), with the muon isolation and $\Delta R$ criteria inverted. The equivalent distribution from the prompt control region is also shown in green. . . . .	72
3.15 The uncorrected lepton $ d_0 $ distributions in the $e\mu$ prompt control region, for electrons (left) and muons (right), for 2017 data and simulation (upper), and 2018 data and simulation (lower). The rightmost bin in each plot contains the overflow entries. . . . .	76
3.16 The average lepton $ d_0 $ as a function of $\phi$ in the $e\mu$ prompt control region, for electrons (left) and muons (right), for 2017 data and simulation. . . . .	77

3.17 The lepton $d_0$ distributions with Gaussian fits in data (left) and background simulation (right) for electrons (upper) and muons (lower) in the 2017 $e\mu$ prompt control region. The widths of the Gaussian fits are used to determine the width of the Gaussian distribution used to smear the $d_0$ . . . . .	77
3.18 The lepton $d_0$ distributions with Gaussian fits in data (left) and background (right) for electrons (upper) and muons (lower) in the 2018 $e\mu$ prompt control region. The widths of the Gaussian fits are used to determine the width of the Gaussian distribution used to smear the $d_0$ . . . . .	78
3.19 Trigger efficiency as a function of lepton $ d_0 $ , for the $e\mu$ channel (upper row), the $ee$ channel (lower left), and the $\mu\mu$ channel (lower right) in 2018 signal, for events in the trigger $p_T$ plateau. . . . .	81
3.20 The pixel hit efficiency as a function of muon $ d_0 $ , for cosmic simulation and NoBPTX data in 2016 (left), 2017 (middle), and 2018 (right) conditions. . . . .	83
3.21 Two-dimensional distributions of $ d_0^a $ and $ d_0^b $ , for the events in data that pass the $e\mu$ (left), $ee$ (middle), and $\mu\mu$ (right) preselection. If a $ d_0 $ value is less than unity, it is set to unity in order to plot in log scale. The inclusive signal region covers the region between $100\ \mu\text{m}$ and $10\ \text{cm}$ in each $ d_0 $ variable shown. . . . .	85
3.22 Two-dimensional distributions of $ d_0^a $ and $ d_0^b $ , for data events in the inclusive SR in the $e\mu$ (left), $ee$ (middle), and $\mu\mu$ (right) channels. . . . .	86
3.23 The two-dimensional distribution of the leading electron and leading muon $ d_0 $ , for the events in data (colors) and signal (black boxes) that pass the $e\mu$ preselection. The size of the black boxes are proportional to the size of the bin content. If a $ d_0 $ value is less than unity, it is set to unity in order to plot in log scale. The inclusive signal region covers the region between $100\ \mu\text{m}$ and $10\ \text{cm}$ in each $ d_0 $ variable shown. . . . .	86
3.24 The 95% C.L. upper limits on the long-lived particle mass ( $m_{\tilde{t}}$ ) as a function of its lifetime ( $c\tau$ ), for the $e\mu$ , $ee$ , and $\mu\mu$ channels. The $\tilde{t}\bar{t} \rightarrow \bar{l}b\ l\bar{b}$ (left) and $\tilde{t}\bar{t} \rightarrow \bar{l}1\ l\bar{1}$ (right) processes are shown. . . . .	90



# Chapter 1: Introduction

## 1.1 The Standard Model

The Standard Model of particle physics (SM) describes all known particles and their non-gravitational interactions. Developed and experimentally verified over the past six decades, the SM posits the existence of twelve spin- $\frac{1}{2}$  particles, the fermions, that make up all observed matter; twelve spin-1 particles, the gauge bosons, that communicate the electromagnetic, weak, and strong forces; and one fundamental scalar, the Higgs boson, which breaks electroweak symmetry, giving mass to the gauge bosons and fermions.

The fermions and gauge bosons can be classified according to the forces with which they interact. The fermions are further divided into six quarks, which carry color and interact via the strong force, and six leptons, which do not. Furthermore, all six quarks and three of the leptons carry electric charge and interact electromagnetically (the neutral leptons are called neutrinos). All fermions interact via the weak force. The gauge bosons include the photon, which communicates the electromagnetic force; the  $W^+$ ,  $W^-$ , and  $Z^0$ , which communicate the weak force; and eight gluons that communicate the strong force. Of these, only the  $W^+$  and  $W^-$  are electrically charged and only the gluons carry color charge. Finally, the fermions are grouped

into three generations, each with two quarks, one charged leptons, and one neutral lepton. Figure 1.1 diagrams the grouping of the SM particles and lists some of their properties.

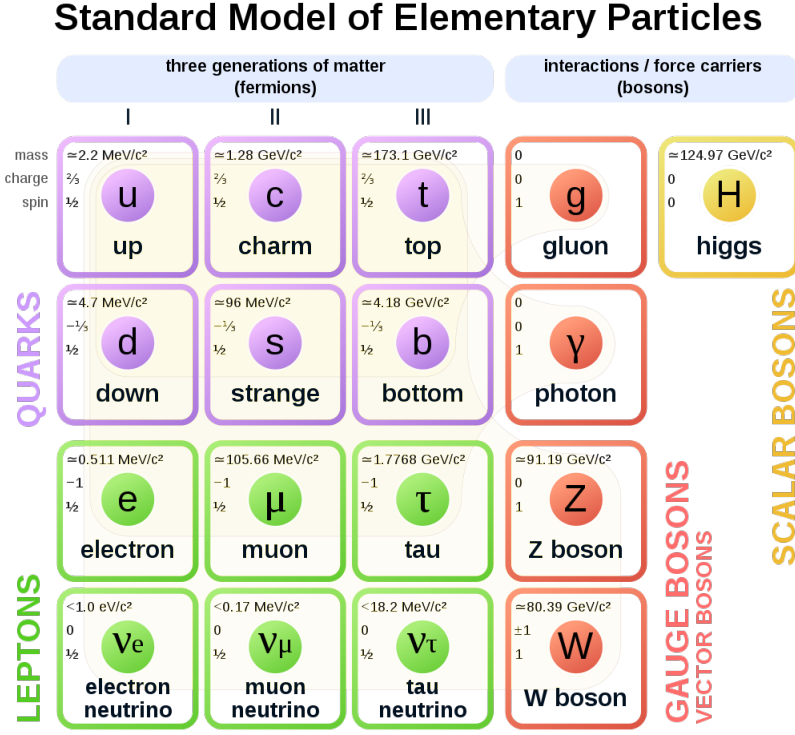


Figure 1.1: The SM particle content.

In the SM, the interactions between particles are governed by two theories: quantum chromodynamics (QCD), which describes the strong force, and the electroweak theory, which describes the electromagnetic and weak forces. The following sections will provide a brief overview of these theories.

### 1.1.1 Quantum chromodynamics

QCD describes the strong interactions between quarks and gluons and is based on the  $SU(3)_c$  symmetry group, where the subscript c refers to color charge. In QCD, all quarks and gluons carry color charge, which allows interactions between two quarks of the same generation and a gluon, three gluons, or four gluons. QCD is responsible for the formation of all hadrons (such as protons and neutrons), and leads to two unique phenomena: confinement and asymptotic freedom.

Confinement refers to the experimental fact that an isolated particle with color charge has never been directly observed. Composite particles composed of quarks and gluons are always neutral under color, and attempts to separate the constituent particles will only produce new hadrons. This phenomenon is the result of the unique running of the strong coupling constant, which increases with decreasing energy (and therefore increasing distance).

Asymptotic freedom shows up at the opposite end of the energy spectrum. In high energy interactions (such as those at the Large Hadron Collider), the strong coupling constant is small enough to render the quarks nearly free. In this regime, the small coupling constant enables perturbative calculations.

### 1.1.2 The electroweak theory

The electroweak theory unifies the electromagnetic and weak interactions and is based on the  $SU(2)_L \otimes U(1)_Y$  symmetry group. It posits two new charges: weak isospin, which has three components  $T_{1,2,3}$ , and hypercharge,  $Y$ .  $T_3$  is  $\pm\frac{1}{2}$  for all left-handed fermions and 0 otherwise, while  $Y$  varies according to  $Q = T_3 + \frac{1}{2}Y$ , where  $Q$  is the familiar electric charge. Each generation of left-handed quarks or leptons forms

an  $SU(2)$  doublet. The first generation doublets, for example, are:

$$\begin{pmatrix} \nu_e \\ e^- \end{pmatrix}_L, \quad \begin{pmatrix} u \\ d \end{pmatrix}_L \quad (1.1)$$

where, as in  $SU(2)_L$ , the L denotes left-handed chiral states. The three generators of  $SU(2)_L$  result in three massless spin-1 bosons:  $W^1$ ,  $W^2$ , and  $W^3$ , while  $U(1)_Y$  gives rise to one massless spin-1 boson,  $B^0$ . When all is said and done, the physical  $W^\pm$  bosons are identified as superpositions of  $W^1$  and  $W^2$  while  $Z^0$  and the photon are identified as superpositions of  $W^3$  and  $B^0$ .

Terms in the electroweak Lagrangian involve either two left-handed fermions and a  $W^\pm$  or  $Z^0$ , two electrically charged particles and a photon, or charge-conserving combinations of  $W^\pm$ s,  $Z^0$ s, and photons that include three or four particles. Conspicuously missing, however, are mass terms for the electroweak gauge bosons or fermions.

### 1.1.3 The Higgs mechanism

As shown in Fig. 1.1, the fermions and  $W^\pm$  and  $Z^0$  bosons all have nonzero mass. Accounting for this fact within the context of QCD and the electroweak theory is difficult because explicit mass terms violate the gauge and chiral symmetry of  $SU(3)_c \otimes SU(2)_L \otimes U(1)_Y$ . For example, a term such as

$$\frac{1}{2}m_A^2 A^\mu A_\mu, \quad (1.2)$$

which assigns mass  $m_A$  to gauge boson  $A$ , becomes

$$\frac{1}{2}m^2(A^\mu - \partial^\mu\alpha)(A_\mu - \partial_\mu\alpha) \neq \frac{1}{2}m^2 A^\mu A_\mu \quad (1.3)$$

under a  $U(1)$  gauge transformation, and a term such as

$$m_f \bar{f} f = m_f (\bar{f}_R f_L + \bar{f}_L f_R), \quad (1.4)$$

which assigns mass  $m_f$  to fermion  $f$ , breaks chiral symmetry by coupling the right- and left-handed components of the fermion.

If the gauge and chiral symmetries of  $SU(3)_c \otimes SU(2)_L \otimes U(1)_Y$  truly are symmetries of nature and the fermions and  $W^\pm$  and  $Z^0$  bosons truly have nonzero mass, then another mechanism must be at work. Spontaneous symmetry breaking, which occurs when the vacuum state does not exhibit all of the symmetries of the underlying theory. In such a situation, each spontaneously broken continuous symmetry gives rise to a massless scalar particle [34]. In the case of spontaneously broken continuous *gauge* symmetries, however, there exists a mechanism by which the massless bosons are removed and some of the gauge bosons associated with the generators of the symmetries acquire mass [28, 36, 35]. In the SM, this mechanism, known as the Higgs mechanism, breaks electroweak symmetry, gives mass to the fermions and  $W^\pm$  and  $Z^0$  bosons, and results in one massive scalar particle, the Higgs boson.

The Higgs mechanism adds the scalar doublet

$$\Phi = \begin{pmatrix} \phi^+ \\ \phi^0 \end{pmatrix}, \quad (1.5)$$

whose potential is given by

$$V(\Phi^\dagger \Phi) = \mu^2 \Phi^\dagger \Phi + \lambda (\Phi^\dagger \Phi)^2, \quad (1.6)$$

to the SM. If  $\mu^2 < 0$  and  $\lambda > 0$ , then  $\Phi^\dagger \Phi = -\frac{\mu^2}{2\lambda}$  defines a circle of minima in the  $\phi^+ - \phi^0$  plane. Even though the potential remains invariant under  $SU(2)_L \otimes U(1)_Y$ , nature must spontaneously choose a vacuum state somewhere along this circle. Because the vacuum state does not respect  $SU(2)_L \otimes U(1)_Y$ , the symmetry is said to be spontaneously broken.

This procedure has three significant consequences. First, three of the four degrees of freedom originally associated with  $\Phi$  are now associated with the longitudinal components of the  $W^\pm$  and  $Z^0$  bosons, which causes them to acquire mass while the photon remains massless. Second,  $\Phi$ 's remaining degree of freedom adds a single massive scalar, the Higgs boson, to the theory. Third, the interaction between the fermions and the nonzero vacuum state of the scalar field produces fermion mass terms that obey chiral symmetry.

#### 1.1.4 Current status

The SM is remarkable successful. It describes all known particles and their non-gravitational interactions, and experiments over the last several decades have repeatedly verified every major prediction it makes. In 2012, the CMS and ATLAS experiments verified its last major untested prediction by independently discovering an approximately 125 GeV scalar particle with properties consistent with the SM Higgs boson [19, 6]. Further measurements in 7, 8, and 8 TeV proton-proton collisions at the Large Hadron Collider continue to agree with SM predictions of the Higgs boson properties . We finally have meaningful evidence as to the origin of electroweak symmetry breaking, and all current evidence indicates that SM Higgs mechanism is indeed responsible.

Despite this remarkable success, the SM is not without problems. For one, it cannot be the whole story: it says nothing on the subjects of gravity, dark matter, or dark energy, which implies that it only describes about 5% of the energy content of the universe and that a more complete theory must take over at or below the energy scale where gravity becomes important ( $M_P \approx 10^{16}$  GeV) . Furthermore, many aspects of

the SM seem arbitrary and unmotivated. It offers no explanation, for example, for why three generations of fermions are necessary or why its many parameters take the values they do. It could be that these unmotivated values are simply experimental facts of nature without explanation, but the history of science implies that a deeper understanding is likely hiding beneath the surface. Finally, the observed value of the Higgs boson mass is not only unexplained, it is unnatural. This final issue, which is explained in the following paragraphs, is a powerful motivation to search for new physics at currently accessible energy scales.

## Naturalness

The naturalness criterion states that an effective theory such as the SM must not be overly sensitive to the details of the underlying higher energy theory. Put another way, it requires that any dimensionless parameter much smaller than one must be protected by a custodial symmetry . Such a criterion may or may not be respected by nature, but history and simple probability are on its side.

The dimensionless parameter in question is the mass of the Higgs boson, which is quadratically sensitive to  $\Lambda$ , the energy scale at which a new theory takes over. All SM parameters are affected by interactions with virtual particles through loop diagrams such as those shown in Fig. 1.2, but the Higgs mass is particularly sensitive. As a fundamental scalar, the Higgs boson lacks the chiral and gauge symmetries enjoyed by the fermions and gauge bosons. These symmetries, known as custodial symmetries, protect the fermion and gauge boson masses by guaranteeing that all corrections are proportional to the bare masses themselves. If the SM is indeed valid up  $M_P$ , then the bare mass of the Higgs boson must be coincidentally equal and opposite to the sum of the terms that correct it to approximately one part in  $10^{30}$ . Such miraculous

fine tuning is technically possible, but it could also be strong evidence that a deeper physical mechanism is at work.

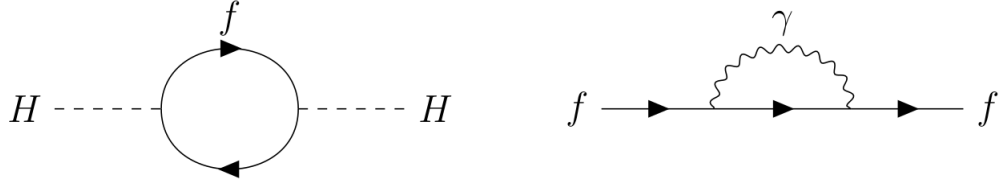


Figure 1.2: Higgs mass (left) corrected by fermion loop and fermion mass (right) corrected by photon loop.

## 1.2 Beyond the Standard Model

Many beyond the SM (BSM) theories have been proposed to address the issues discussed in Section 1.1.4. Theories such as large extra dimensions address the unnatural Higgs boson mass by allowing gravity to spread across more than three spatial dimensions, which lowers  $M_P$  and therefore the size of the Higgs boson mass corrections. Other theories, such as supersymmetry, posit new symmetries that protect the Higgs boson mass from large corrections.

### 1.2.1 Supersymmetry

Supersymmetry (SUSY) introduces a new symmetry in which every SM particle fits into a larger multiplet with an inherent symmetry between bosons and fermions. In its simplest form, SUSY predicts one new boson for every SM fermion, one new fermion for every SM boson, and one new Higgs doublet. The increase in particle multiplicity necessitates a new naming convention: the spin-0 superpartners of the SM

fermions are called sfermions (e.g. sleptons or squarks) while the spin- $\frac{1}{2}$  superpartners to the SM bosons add "ino" to the end of their SM counterpart (e.g. Higgsino or wino).

When calculating contributions to the Higgs boson mass from loop diagrams, one finds that fermion loops differ in sign from boson loops, which means that in SUSY every bosonic correction to the Higgs mass is cancelled by a fermionic correction and vice versa. If SUSY were an exact symmetry of nature, the cancellation would be perfect, and the observed Higgs boson mass would match the bare Higgs boson mass exactly. Figure 1.3 shows a sample leading-order cancellation.

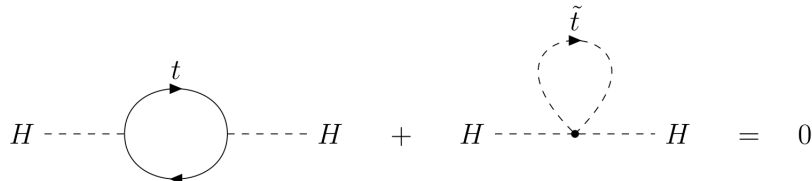


Figure 1.3: Corrections to the Higgs boson mass from the top quark (left) and top squark (right) cancel in exact SUSY. The top quark and top squark contributions are enhanced by the large top–Higgs coupling.

Exact SUSY also requires that SUSY particles have the same mass as their SM counterparts, so the uniformly null results in collider searches imply that if SUSY exists, it must be a broken symmetry. In broken SUSY, the diagrams in Fig. 1.3 no longer exactly cancel. Instead, the resulting correction is proportional to the mass of the top squark, which means that broken SUSY can still resolve the naturalness problem if the SUSY particles that correct the Higgs boson mass are relatively light.

## 1.2.2 Long-lived particles

In the context of collider physics, long-lived particles (LLPs) are particles whose lifetimes are such that they decay a measurable distance from the collision point. This category includes everything from particles that decay less than 1 mm away from the collision to particles that propagate through the entire detector.

SM particles are long lived for many reasons. First, symmetries such as charge and baryon number conservation ensure that particles such as electrons and protons are absolutely stable. Second, small coupling constants and highly virtual intermediate states decrease the decay rate of particles such as muons, whose  $2.2\text{ }\mu\text{s}$  lifetime is the product of a weak decay through a virtual  $W$  boson (the  $W$  boson mass is about 760 times that of the muon). Finally, limited decay phase space increases the lifetime of particles such as the neutron, whose decay into a proton, an electron, and an electron neutrino is slowed by the near mass degeneracy of the neutron and the proton. The mass difference between the neutron and its decay products is less than 1 MeV. The muon and neutron decays are diagrammed in Fig. 1.4.

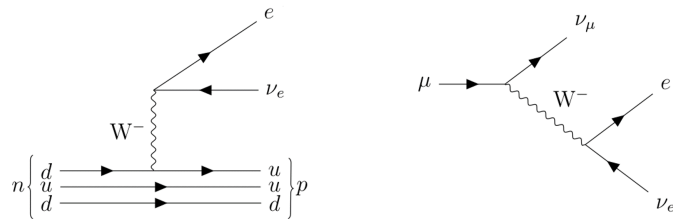


Figure 1.4: Long-lived decays of the neutron (left) and muon (right).

In BSM physics, the same fundamental mechanisms have the potential to produce new long-lived particles. Many SUSY scenarios, for example, introduce a symmetry known as R parity that prevents proton decay. In models with exact R-parity conservation, SM particles are assigned R-parity 1 and SUSY particles are assigned R-parity  $-1$ . Conserving the product of R-parity at each vertex has two phenomenological consequences: SUSY particles must be produced in pairs, and the lightest SUSY particle (LSP) must be absolutely stable. A neutral, weakly interacting LSP would therefore pass through detectors such as the CMS detector described in Section 2.2 without interacting. The resulting momentum imbalance is a standard signature in SUSY searches .

On the other hand, SUSY models with weakly coupled R-parity violating (RPV) terms produce long-lived but not perfectly stable LSPs . A similar situation arises in gauge-mediated SUSY breaking models where the gravitino is the LSP. The strength of the coupling between the next-to-LSP (NLSP) and the gravitino is inversely proportional to the energy scale at which SUSY is broken. A high SUSY breaking scale therefore suppresses the NLSP decay rate, making it long lived .

LLPs also arise from particular SUSY mass spectra. Models in the Split SUSY paradigm, for example, propose that the spin-0 SUSY particles are significantly more massive than the spin- $\frac{1}{2}$  SUSY particles. In these models, the gluino becomes long lived when its decay to two quarks and a neutral  $spin - \frac{1}{2}$  SUSY particle is suppressed by a highly virtual intermediate squark . Other SUSY models produce long-lived particles by limiting decay phase space. Some anomaly-mediated SUSY breaking models, for example, predict that the NLSP and LSP are nearly degenerate in mass. Just like

the neutron decaying into a proton, the lack of available phase space suppresses the decay and produces a long-lived NLSP .

In summary, LLPs are a general feature of the SM, and it is reasonable to assume that the same mechanisms that produce SM LLPs will also manifest in BSM physics. The following subsection gives an overview of the phenomenology of the SUSY model most relevant to the analysis presented in Chapter 3, while the experimental details of this model and LLP searches at the LHC will be saved until after presenting the LHC and CMS experiment in Chapter 2.

### 1.2.3 Displaced supersymmetry

## **Chapter 2: The Large Hadron Collider and Compact Muon Solenoid experiment**

### **2.1 The Large Hadron Collider**

The Large Hadron Collider (LHC) is the highest-energy particle collider ever constructed. Located at the European Organization for Nuclear Research (CERN) and housed in a 27 km ring approximately 100 m below the French/Swiss countryside, the LHC is designed to accelerate two counter-rotating beams of protons to 7 TeV (and sometimes beams of heavy ions to 2.8 TeV) and collide them at four points around the ring. Each collision point is instrumented with a dedicated detector: the ATLAS (A Toroidal LHC ApparatuS) and CMS (Compact Muon Solenoid) experiments are general purpose detectors designed to reconstruct the remnants of proton collisions at the highest collision rates offered by the LHC, LHCb (LHC beauty) studies b-quark decays from proton collisions produced at lower collision rates, and ALICE (A Large Ion Collider Experiment) studies heavy-ion collisions [30]. Figure 2.1 shows the location of each experiment around the LHC ring. The analysis presented in Chapter 3 utilizes proton-proton collision data collected by the CMS experiment, and the following discussion is focused accordingly.

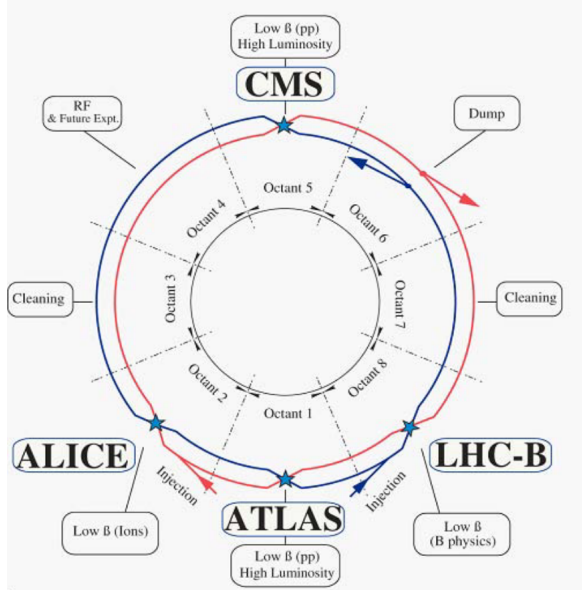


Figure 2.1: Layout of the LHC experiments [30].

### 2.1.1 Injection chain

The protons ultimately collided by the LHC must first travel through much of the CERN accelerator complex, which is diagrammed in Fig. 2.2. The 6.5 TeV proton beams relevant to this thesis start their journey as the nuclei of hydrogen atoms in a bottle of hydrogen gas. After stripping away the electrons with an electric field, the protons are accelerated to an energy of 50 MeV with the Linac 2 linear accelerator [3]. The Proton Synchrotron Booster (PSB) next accelerates the protons to an energy of 1.4 GeV before injecting them into the Proton Synchrotron (PS) [4]. The PS was the first synchrotron constructed at CERN and was the highest-energy particle accelerator in the world at the time of its first operation [2]. Today, it accelerates protons to an energy of 25 GeV before passing them along to the Super Proton Synchrotron (SPS), which is the 7 km proton-antiproton collider at which the W and Z bosons were

discovered in 1983 [5]. As the final step in the LHC injection chain, SPS accelerates protons to an energy of 450 GeV before injecting them into the LHC [30].

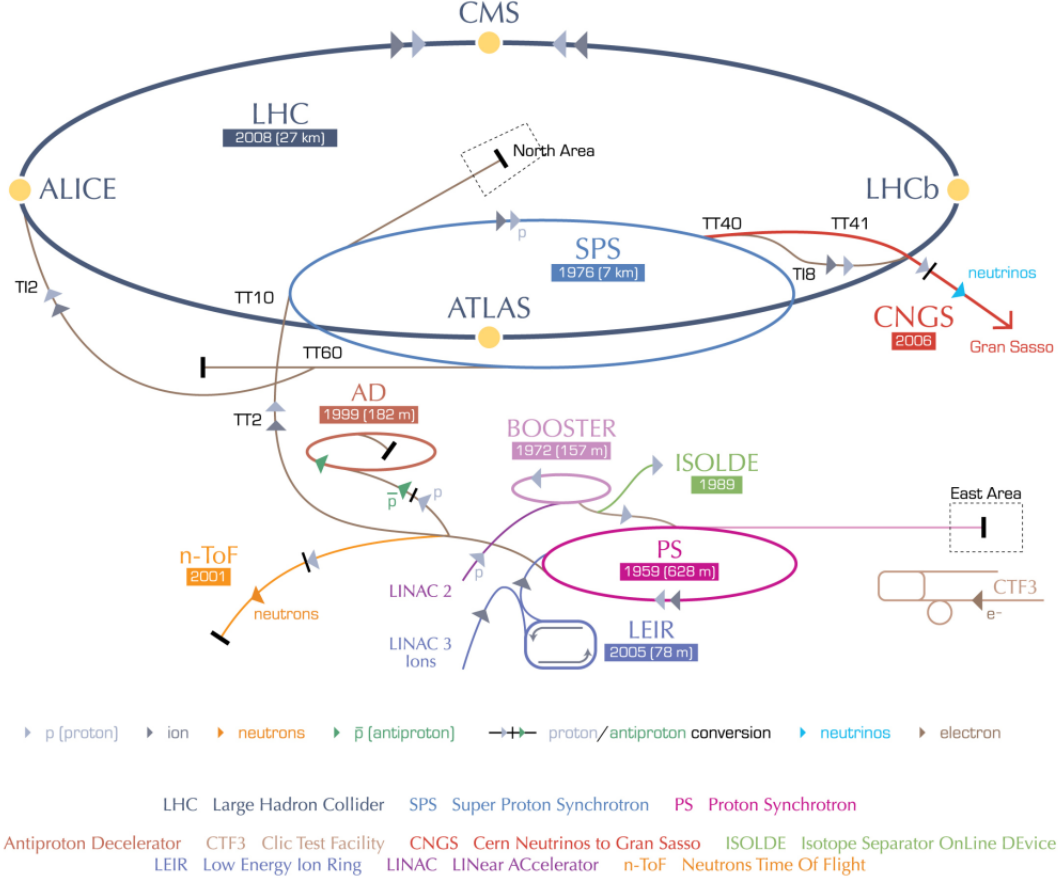


Figure 2.2: A diagram of the CERN accelerator complex. The analysis presented in Chapter 3 utilizes protons accelerated by LINAC 2, BOOSTER (also known as PSB), PS, SPS, and finally the LHC before their ultimate collision inside CMS [40].

### 2.1.2 Main ring

Maximizing the physics potential of the LHC requires simultaneously maximizing the collision energy and the number of interesting collisions per unit time. The main LHC ring is therefore designed to accelerate the 450 GeV protons it receives from

SPS to 7 GeV and collimate them into intense beams to be collided at high rates. The number of interesting collisions per unit time is ultimately the product of the total cross-section of the processes one deems interesting,  $\sigma$ , and the instantaneous luminosity,  $L$ , which is given by:

$$L = \frac{N_b^2 n_b f_{rev} \gamma_r}{4\pi \epsilon_n \beta^*} F \quad (2.1)$$

where the parameters are defined as in Table 2.1 [30].

Table 2.1: Luminosity parameters used in Eq. (2.1).

Parameter	Description
$N_b$	Number of particles per bunch
$n_b$	Number of bunches per beam
$f_{rev}$	Revolution frequency
$\gamma_r$	Relativistic gamma factor
$\epsilon_n$	Normalized transverse beam emittance
$\beta^*$	Beta function at collision point
$F$	Geometric luminosity reduction factor

The LHC is designed to deliver a maximum instantaneous luminosity of  $10^{34} \text{ cm}^{-2} \text{ s}^{-1}$  to ATLAS and CMS, but operational improvements, mostly notably a reduction in  $\epsilon_n$  and  $\beta^*$ , have allowed the LHC to exceed this goal by up to a factor of approximately two in the 2016, 2017, and 2018 data-taking periods. [54]. As shown in Fig. 2.3, the total integrated luminosity delivered during this period is approximately a factor of five times greater than that of the 2011–2012 period. The ability to produce high-energy proton collisions at such high rates depends on several impressive technological feats, notably the superconducting magnets that steer the and shape the beams and

the superconducting radio-frequency (RF) cavities that accelerate the protons and determine their bunch structure.

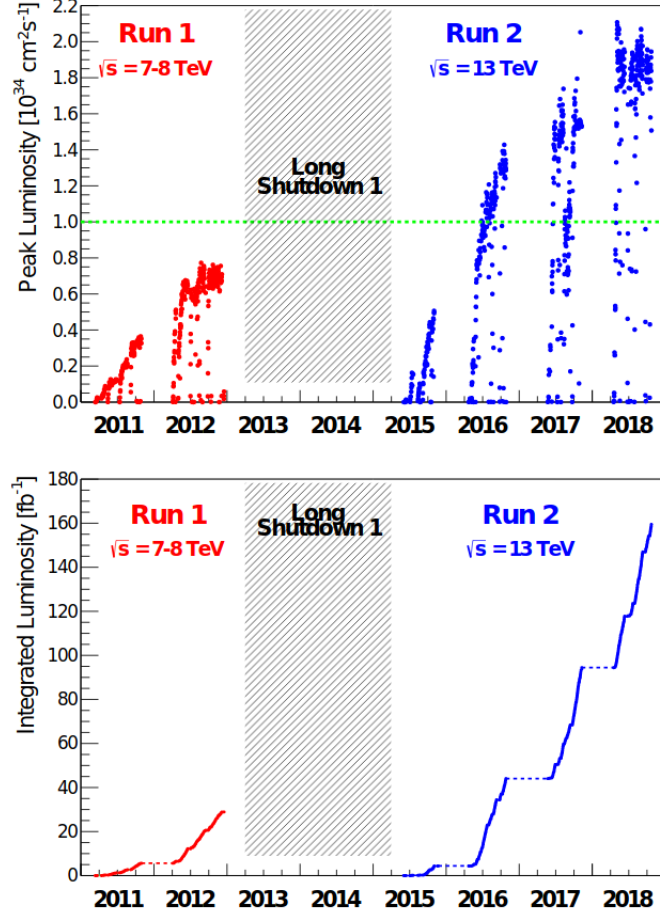


Figure 2.3: The peak instantaneous (top) and integrated (bottom) luminosity delivered by the LHC during proton operation between 2011 and 2018 [54].

## Superconducting magnets

The LHC magnet system relies on superconducting NbTi magnets that are cooled to below 2 K with superfluid helium and capable of producing fields in excess of 8 T. The design of the main dipole magnets that are responsible for keeping the beams in

a circular trajectory is heavily influenced by the size of the LHC tunnel, which originally housed the Large Electron-Positron Collider (LEP). Unlike LEP, which collided particles and antiparticles, the LHC requires two separate beam pipes, each with its own dipole magnetic field. This requirement, along with the limited tunnel cross section, motivates the "two-in-one" magnet design in which both superconducting magnets share a common cold mass and cryostat, as shown in Fig. 2.4 [30].

In addition to the main dipole magnets, the LHC also employs quadrupole magnets for beam focusing and sextupole, octupole, and decapole magnets to correct the field at the edges of the dipoles [30].

### LHC DIPOLE : STANDARD CROSS-SECTION

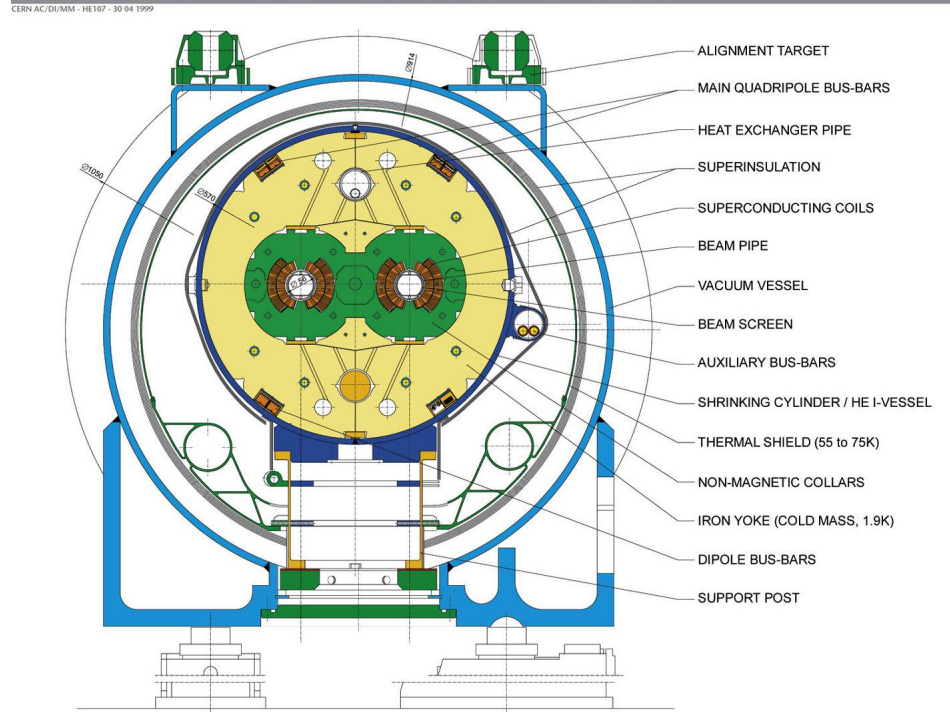


Figure 2.4: Diagram of an LHC dipole magnet in cross-section [52].

## Radio-frequency cavities

An RF superconducting cavity system is responsible for capturing the 450 GeV protons injected into the LHC from SPS, accelerating them to the full collision energy, defining their bunch structure, and storing them. The main RF system operates at 400 MHz and is located in Octant 4 (see Fig.2.1). Each RF cavity contains an oscillating electromagnetic field whose phase is synchronized with the arrival of the proton bunches such that the protons passing through the cavity always feel a force in the direction of their motion. The applied force will naturally vary for protons that are slightly out of phase in such a way as to keep the protons tightly bunched in the longitudinal direction [30].

## 2.2 The Compact Muon Solenoid experiment

The Compact Muon Solenoid experiment (CMS) is designed for the general study of the highest-energy, highest-luminosity proton-proton (and heavy ion) collisions the LHC can provide. The detector design is driven by the particular goals of exploring physics at the TeV scale and discovering the origin of electroweak symmetry breaking [16]. More than 4000 collaborators from intuitions across more than forty countries work together to collect and analyze the data using a global computing grid [1].

To reconstruct the variety of particles that emerge from high-energy proton-proton collisions, CMS uses several complimentary subdetectors nested radially about the collision point. A 4 T superconducting solenoid magnet provides a powerful magnetic field to bend the trajectories of charged particles, thus enabling the determination of their momenta. Working from the center out, the CMS detector consists of an all-silicon tracker, a lead-tungstate scintillating crystal electromagnetic calorimeter,

a sampling hadronic calorimeter composed of brass absorber and plastic scintillator tiles, the superconducting solenoid magnet, and a muon system with three varieties of gaseous detectors. Figure 2.5 shows the detector layout, and the remainder of this chapter is devoted to a brief overview of each subsystem as well as the triggering and reconstruction strategies employed by CMS.

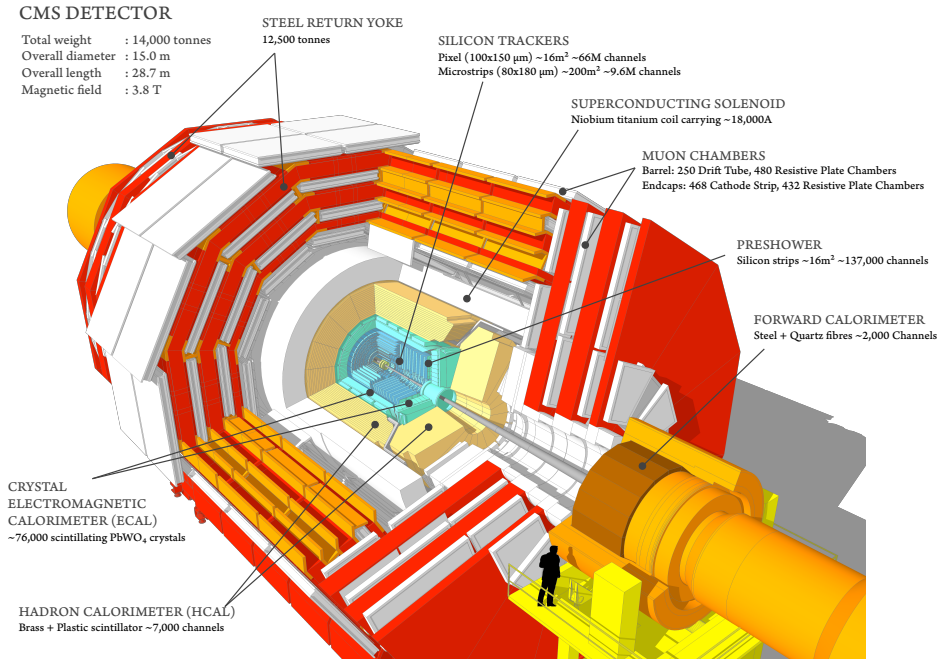


Figure 2.5: The CMS detector [44].

CMS uses a right-handed coordinate system centered on the nominal collision point with positive  $x$  direction pointing towards the center of the LHC ring and the positive  $y$  direction pointing vertically upward. The azimuthal angle in the  $x$ - $y$  plane, denoted  $\phi$ , is measured from the positive  $x$  axis, and the polar angle  $\theta$  is measured from the positive  $z$  axis. The angle from the  $z$  axis is more commonly described in

terms of the pseudorapidity  $\eta$ , which is defined as  $\eta = -\ln \tan(\theta/2)$ . The component of the momentum that is transverse to the beam direction (i.e., in the x–y plane) is denoted  $p_T$ , and the magnitude of the negative vector sum of the  $p_T$  of all the reconstructed particles in an event is denoted  $p_T^{miss}$  [15, 18].

The CMS detector has undergone several upgrades since its initial construction. The description presented here will focus on the detector conditions relevant to the analysis presented in Section 3.

### 2.2.1 Solenoid magnet

The superconducting solenoid produces a 4 T magnetic field throughout the 6.3 m diameter, 12.5 m long cylindrical volume that contains the tracker and calorimeters. The magnetic field is produced by running 19 kA through 2168 turns of NbTi superconducting cable that are cooled with liquid helium. The flux returns through an iron yoke that also houses the muon system [18].

The strong magnetic field is critical to CMS’s ability to unambiguously distinguish muons and anti-muons with transverse momenta up to 1 TeV [15], and much of the overall detector design is guided by the choice of a large superconducting solenoid. The uniform magnetic field alters the trajectories of charged particles immediately upon their production, which results in significant bending power within a relatively small radius and therefore enables a compact detector.

The CMS solenoid stores a uniquely large amount of energy in its magnetic field when compared to other collider detector magnets without requiring a uniquely large mass. To avoid deforming in its own magnetic field, the superconducting coils are reinforced with an aluminium alloy so that the coil layers themselves handle 70% of

the magnetic hoop stress. Figure 2.6 compares several collider detector magnets in the energy/mass vs energy plane and shows a cross-sectional view of the reinforced conductor coils in cross section. This approach allows for a relatively thin solenoid that is less likely to scatter muons before they reach the muon system [18].

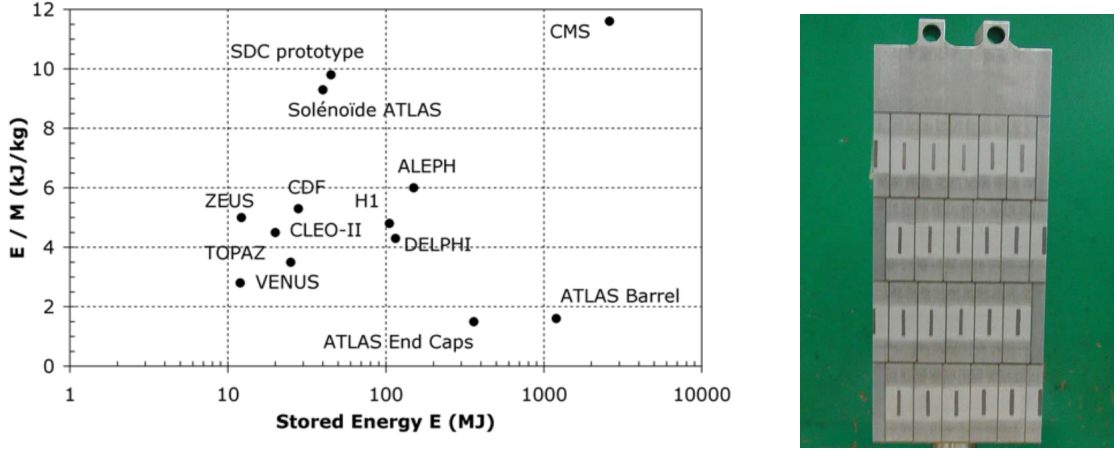


Figure 2.6: Left: the stored-energy-over-mass ratio  $E/M$ , for several detector magnets. Right: cross section of the four-layer winding of reinforced conductor in the CMS superconducting solenoid [18].

### 2.2.2 Tracker

In the region closest to the proton collisions, CMS employs a silicon tracker to reconstruct particle trajectories along with primary and secondary vertices. Efficiently and accurately performing these tasks allows CMS to measure charged particle momenta, distinguish particles from the primary and pileup vertices, and identify heavy flavor decays. The high-particle-flux environment necessitates a highly granular, fast, and radiation hard detector that simultaneously introduces the smallest

possible amount of material to the region inside the calorimeters. The resulting detector contains over  $200\text{ m}^2$  of active silicon, making it the largest silicon tracker ever built.

The tracker has a length of 5.8 m, a diameter of 2.5 m, and is composed of two subdetectors. Inside 20 cm from the beamline, the large particle flux demands the use of silicon pixel detectors, while silicon micro-strip detectors suffice in the region beyond 20 cm [18]. The original pixel detector was replaced between the 2016 and 2017 data-taking periods in preparation for higher luminosities [7]. As the analysis presented in Section 3 uses data collected in 2016–2018 and is particularly dependent on tracker measurements, the original pixel detector, 2017–2018 (Phase-1) pixel detector, and strip detector are described separately below.

### Original pixel detector

The original CMS pixel detector covers the  $|\eta| < 2.5$  region and is composed of three cylindrical barrel layers at  $r = 4.4$ , 7.3, and 10.2 cm and four endcap disks 34.5 and 46.5 cm up and down the beamline from the nominal collision point. Each layer or disk is instrumented with several pixel modules that are composed of a silicon sensor bump bonded to custom ASIC read-out chips (ROCs). Each sensor is 285  $\mu\text{m}$  thick and typically comprises 66560  $100 \times 150\,\mu\text{m}$  pixels. The nearly square pixel shape enables approximately 15  $\mu\text{m}$  hit resolution in both the  $r - \phi$  and  $z$  directions [15, 18].

The original pixel detector was designed for a maximum instantaneous luminosity of  $10^{34}\,\text{cm}^{-2}\,\text{s}^{-1}$ , which corresponds to approximately 25 pileup collisions per bunch crossing at the LHC.

## Phase-1 pixel detector

The Phase-1 pixel detector represents an incremental improvement over the original CMS pixel detector: the same fundamental technology fills the same physical footprint and reuses many of the existing services but nevertheless achieves higher rate capabilities, improved radiation tolerance, and more robust tracking [7]. This is achieved by adding one additional layer to the barrel and each endcap, decreasing the radius of the innermost barrel layer to 2.9 cm, upgrading the ROCs, and reducing the material budget of the cooling system and mechanical structure [7, 26]. Figure 2.7 compares the geometries of the original and Phase-1 pixel detectors.

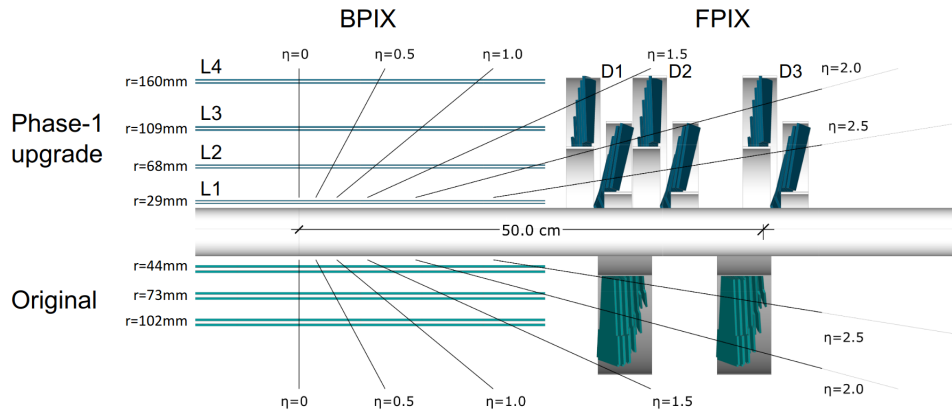


Figure 2.7: Comparison of the original and Phase-1 CMS pixel detector layouts in  $y - z$  plane [7].

## Strip tracker

The strip tracker surrounds the pixel detector with silicon micro-strip sensors in 10 cylindrical barrel layers between  $r = 20$  cm and  $r = 110$  cm and 12 disks on each side of the barrel detector that extend to  $|z| < 282$  cm and cover up to  $|\eta| < 2.5$ .

The strip pitch generally increases with radius and results in hit resolutions that vary from 23 to 530  $\mu\text{m}$  [18]. Figure 2.8 shows the layout of the entire silicon tracker.

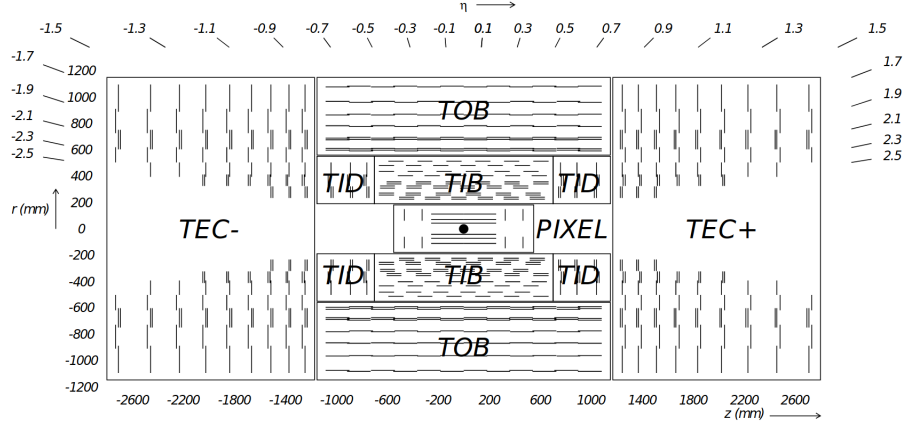


Figure 2.8: Layout of the CMS silicon tracker. TIB, TOB, TID, and TEC refer to subdetectors of the strip detector while PIXEL refers to the original pixel detector. The Phase-1 pixel detector is contained within the same volume [18].

### 2.2.3 Electromagnetic calorimeter

After traversing the inner tracker, particles next encounter the electromagnetic calorimeter (ECAL). As a homogeneous scintillation calorimeter, ECAL uses 61 200 lead tungstate crystals in the barrel and 7324 in each endcap to reconstruct the energy deposited during electromagnetic showers. Lead tungstate crystals allow for a fast (80 % of light emitted within 25 ns), compact (radiation length = 0.89 cm), fine-grained (Molière radius = 2.2 cm), and radiation hard (up to 10 Mrad) calorimeter. The main drawback is the relatively low light yield (30 photon/MeV), which necessitates photodetectors with intrinsic gain that work in magnetic fields[18, 15].

The ECAL performance requirements were heavily influenced by the possibility to reconstruct the decays of Higgs bosons to two photons [16]. Despite the small branching fraction and irreducible background, this decay channel provides a clean signature of a narrow mass peak on top of a smoothly falling background. Thanks in large part to the excellent ECAL energy resolution, the diphoton channel indeed provided the largest significance and best mass resolution (approximately 1 GeV resolution at 125 GeV) in the CMS Higgs boson discovery in 2012 (see Fig. 2.9 [19]).

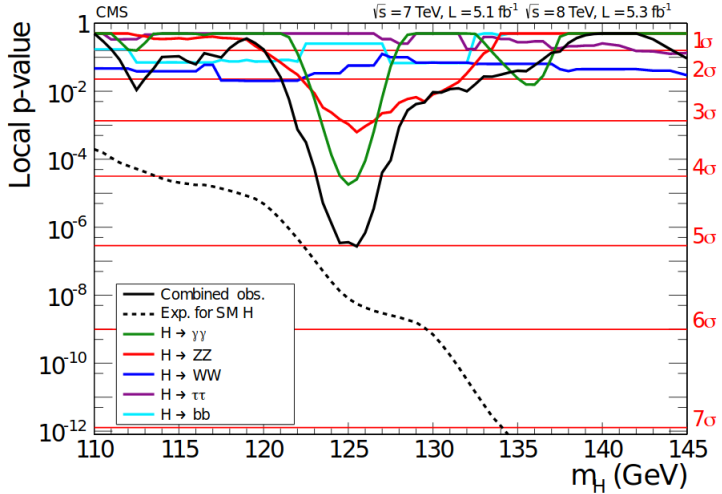


Figure 2.9: The observed local p-value for the five decay modes and the overall combination as a function of the SM Higgs boson mass showing the importance of the ECAL mass resolution in the discovery of the Higgs boson with the CMS experiment. The dashed line shows the expected local p-values for a SM Higgs boson with a mass  $m_H$  [19].

The barrel section extends radially from 129 to 177 cm and covers up to  $|\eta| < 1.479$ . The crystals are tapered to approximately project back to the IP but not so perfectly that likely particle trajectories align with cracks. Each crystal is approximately one

Moli  re radius wide and 25 radiation lengths deep. The crystals in each endcap section are arranged in an x-y grid that starts at  $|z| = 315$  cm and covers  $1.479 < \eta < 3.0$ .

### 2.2.4 Hadronic calorimeter

Particles that survive the ECAL will next encounter the hadronic calorimeter (HCAL). As the ECAL constitutes approximately 25 radiation lengths but only one interaction length, only particles that decay through the strong force will make it to the HCAL. In addition to reconstructing the decays of hadrons, the HCAL plays a particularly important role in measuring  $p_T^{miss}$ . By maximizing the coverage in  $\eta$  and overall amount of material in terms of interaction lengths, HCAL ensures that nearly all particles (other than muons, neutrinos, and hypothetical BSM particles) decay and deposit all their energy before reaching the solenoid. The muon momentum is reconstructed using the tracker and muon system, so only neutrinos and hypothetical BSM particles will contribute to  $p_T^{miss}$ . Reliable  $p_T^{miss}$  measurements are particularly important when searching for new weakly interacting particles with large lifetimes such as those predicted by many dark matter and SUSY models.

With these goals and the constraint of fitting within the solenoid volume in mind, HCAL is designed as a sampling calorimeter that uses 3.7 mm thick plates of plastic scintillator interspersed within approximately 5 cm thick brass absorber plates to reconstruct the energy deposited during hadronic showers. Embedded wavelength-shifting fibers capture the scintillation light and transfer it to clear fibers to be read out by hybrid photodiodes.

The barrel section ( $|\eta| < 1.4$ ) is segmented into 32 towers in  $\eta$  and 64 in  $\phi$  that each contain 17 active scintillator layers. In addition, an extra layer (or two at  $\eta = 0$ ) of

scintillator tiles sits just outside the solenoid. This extra layer spans covers  $|\eta| < 1.26$  and increases the minimum effective HCAL interaction length to greater than 11.8. Each endcap spans a pseudorapidity range of 1.3 to 3.0 with 14 towers in eta and 5 to  $10^\circ \phi$  segmentation. Also, a steel and quartz fiber forward calorimeter (HF) sits 11.2 m from the interaction point and covers  $3 < |\eta| < 5$ . In HF, particles produce Cherenkov light when traversing the quartz fibers that run parallel to the beamline. Figure 2.10 shows the layout of the barrel, endcap, and forward HCAL subdetectors.

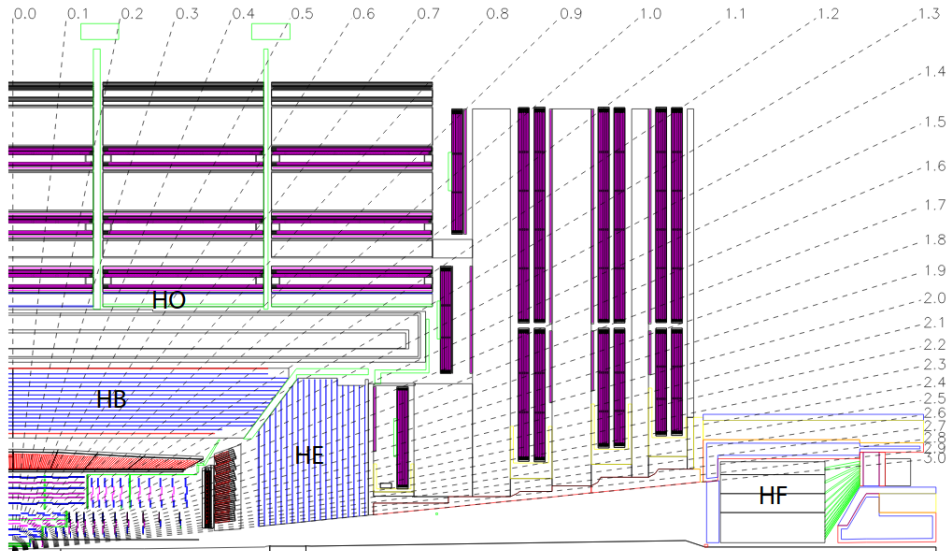


Figure 2.10: Layout of the hadron calorimeter barrel (HB), outer (HO), endcap (HE), and forward (HF) subdetectors [18].

### 2.2.5 Muon system

The CMS muon system is composed of three varieties of gaseous detectors embedded in the iron return yoke outside the superconducting solenoid. In the central region ( $|\eta| < 1.2$ ), the low muon and neutron rates along with the lower magnetic field,

allow the use of drift tube (DT) chambers. At higher  $\eta$  ( $0.9 \leq |\eta| < 2.4$ ), cathode strip chambers (CSCs) are required to handle the higher rates and larger magnetic field. Finally, resistive plate chambers (RPCs), which provide more accurate time measurements and worse spatial resolution than the DTs and CSCs, complement the other detectors out to  $|\eta| < 1.9$  [15, 50].

As shown in Fig. 2.11, the muon momentum resolution of the inner tracker is about an order of magnitude better than that of the muon system for low- $p_T$  muons. The muon system is critical, however, for maintaining the  $< 10\%$  momentum resolution that is necessary to unambiguously differentiate muons and anti-muons up to 1 TeV. In addition to improving muon reconstruction, the muon system provides information to the L1 trigger (see Section 2.2.6) and is capable of triggering on the muons with good efficiency, high background rejections, and about 15–25%  $p_T$  resolution without input from the rest of the detector.

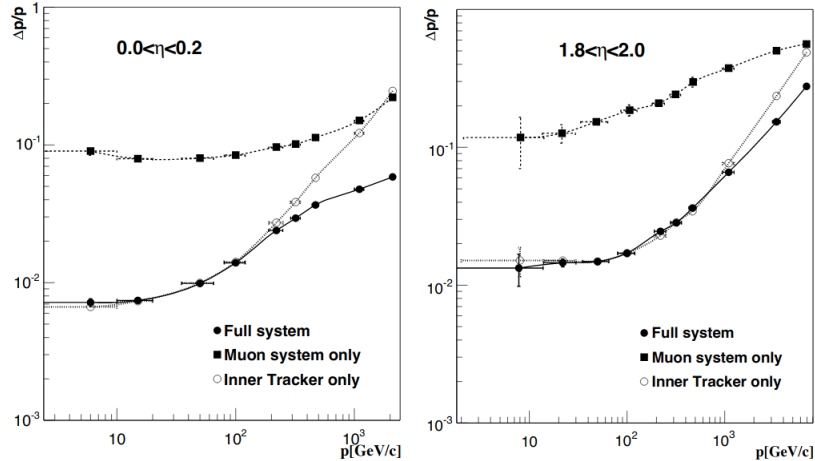


Figure 2.11: Muon momentum resolution as a function of momentum using the CMS muon system, the CMS inner tracker, and the combination of the two subdetectors in two different  $\eta$  ranges [15].

The DTs are organized into four stations, each of which contain up to 70 DT chambers that each measure the muon hit position in either the  $r\phi$  or longitudinal direction. Each chamber is composed of two or three collections of four-layer groupings of 13 by 42 mm drift cells. As shown in Fig. 2.12, a 2–4 m anode wire runs down the center of each drift cell while electrode and cathode strips line the top, bottom, and walls of the cell. The cells are filled with an Ar/CO<sub>2</sub> gas mixture that is ionized by charged particles traversing the cell. The liberated electrons cause avalanches in the large electric fields before being collected by the anode wire.

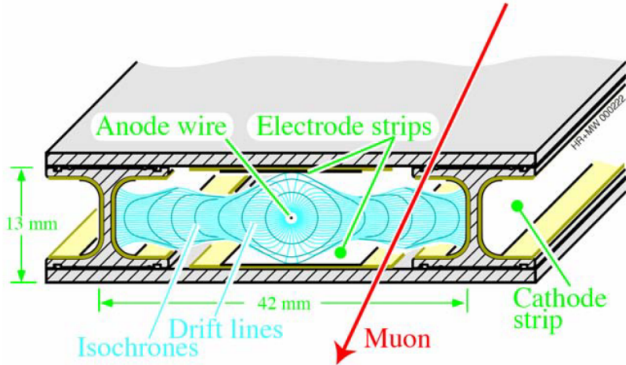


Figure 2.12: Sketch of a CMS muon system drift cell showing drift lines and isochrones. The plates at the top and bottom of the cell are at ground potential while the voltages applied to the electrodes are +3600 V for wires, 1800 V for strips, and -1200 V for cathodes [18].

Each endcap contains four CSC stations, each with six layers of CSCs whose cathode strips run radially outward to provide muon hit position measurements in the  $r\phi$  plane while the anode wires run in the azimuthal direction to provide measurements in  $\eta$ . As in the DTs, charged particles ionize a gas mixture inside each chamber (this

time an Ar/CO<sub>2</sub>/CF<sub>4</sub> mixture), which leads to an avalanche of electrons that are collected by an anode wire. In the CSCs, however, several anode wires share the same chamber and a two-coordinate position measurement is obtained by also reading out the induced charge on the perpendicular cathode strips.

The RPCs are composed of parallel resistive plates separated by two 2 mm gas gaps.

### 2.2.6 Trigger

The trigger reduces the data writing rate from the 40 MHz collision rate to less than 1 kHz so that events can be written to tape. The rate reduction happens in two stages: Level-1 (L1) and High-Level Trigger (HLT). L1 analyzes input from ECAL, HCAL, and the muon system with custom electronics to reduce the rate to approximately 100 kHz in 3.8  $\mu$ s. With input from all subdetectors, the HLT then uses a dedicated processor farm to further reduce the rate to the desired < 1 kHz [18, 17].

### 2.2.7 Physics object reconstruction

CMS uses a particle-flow (PF) algorithm to reconstruct the properties of individual particles by combining measurements from all subdetectors. Starting from charged particle tracks from the tracker and muon system and clusters of energy deposited in the ECAL and HCAL, CMS’s PF algorithm aims to reconstruct all final-state electrons, muons, photons, and charged and neutral hadrons in a given event. This section first describes the reconstruction of tracks and energy clusters before moving on to individual particle identification and reconstruction. [45] is cited throughout.

## Charged particle tracks

Charged particle tracks are reconstructed with an iterative procedure. Despite the middling reconstruction efficiency of each individual step, starting with the highest-purity algorithms and masking the hits associated with each reconstructed track before moving on to the next step results in higher efficiency than could be achieved with any single tracking algorithm without increasing the rate of misreconstruction. This general principle applies to all charged particle tracks, but the tracks associated with candidate electrons and muons receive special consideration.

To better handle electron trajectories affected by radiative energy loss, CMS employs a special iterative tracking procedure that includes a Gaussian-sum filter (GSF) [8]. This approach improves the overall reconstruction efficiency, allows reconstruction of lower-pT electrons, helps identify electrons from photon conversions, and helps distinguish electrons from charged hadrons.

Muon track reconstruction benefits from measurements in the tracker and the muon system. Candidate muon tracks are placed in one of three categories depending on which subdetectors are used in their reconstruction: standalone muon tracks only use muon system hits, tracker muon tracks only use tracker hits and the requirement of at least one consistent muon system hit, and global muon tracks are reconstructed from a global fit of tracker and muon system hits.

## Calorimeter energy clusters

Energy deposits in the calorimeters are clustered separately in ECAL and HCAL with a Gaussian-mixture model that assumes the energy deposits arise from an arbitrary number of Gaussian energy deposits whose amplitude and location are allowed

to vary while the width is determined by the calorimeter properties. The clusters are first seeded by cells with energy above some threshold and greater than the energy of the surrounding cells. Nearby clusters are then merged before being fed to the Gaussian-mixture algorithm. Finally, several corrections are applied to the cluster energies to ensure accurate responses to photons and hadrons.

### Particle-flow reconstruction

The tracks and clusters are then identified with and used to reconstruct all individual particles in an event. The first step is to link tracks and clusters together into groups that correspond one or a few particles. Tracker tracks are extrapolated outwards and linked with the nearest ECAL and HCAL clusters that within a set radius in the  $\eta - \phi$  plane. In the case of candidate electron tracks, tracker tracks and ECAL deposits consistent with electron radiative losses are also linked with the candidate electron track. ECAL and HCAL clusters are similarly linked together by proximity in the  $\eta - \phi$  plane. Due to the high granularity of CMS subdetectors, the number of tracks and clusters in a linked group is largely independent of the total number of particles in an event.

Each group of linked tracks and clusters is then processed by the PF particle identification and reconstruction algorithm. As in track reconstruction, particle reconstruction is an iterative process in which the tracks and clusters are masked after being associated with a particle. Figure 2.13 diagrams the basic concept used to identify muons, electrons, photons, and charged and neutral hadrons, and each step of the PF algorithm is summarized below.

Muons are reconstructed first from isolated global muon candidates, then non-isolated global muon candidates, and finally tracker muon (standalone muon) candidate tracks that are particularly well measured and consistent with hits in the muon system (tracker). Muon momentum is taken from the tracker track when  $p_T < 200 \text{ GeV}$  and from the combination of tracker and muon system hits yields the best fit otherwise.

Electrons and isolated photon reconstruction, which occur together after muon reconstruction, are necessarily interrelated by the high probability that an electron radiates a photon or a photon pair-produces electrons when interacting with tracker material. Electrons are identified from GSF tracks with a corresponding ECAL cluster while isolated photons are identified from isolated ECAL clusters. The total electron energy accounts for radiative losses that show up as ECAL clusters, and both electrons and isolated photons require a high ratio of ECAL cluster energy to nearby HCAL cluster energy.

Next, nonisolated photons and charged and neutral hadrons are reconstructed from the remaining tracks and clusters. Within the tracker acceptance ( $|\eta| < 2.5$ ), ECAL (HCAL) clusters without associated tracks are identified as photons (neutral hadrons). At higher  $\eta$ , nearby ECAL and HCAL clusters are assumed to arise from the same hadron shower and ECAL clusters without nearby HCAL clusters are identified as photons. Discrepancies between track momenta and associated HCAL cluster energy are also used to identify neutral hadrons and muons. Finally, a post-processing step corrects for rare failure modes that can potentially produce inaccurately large missing momentum.

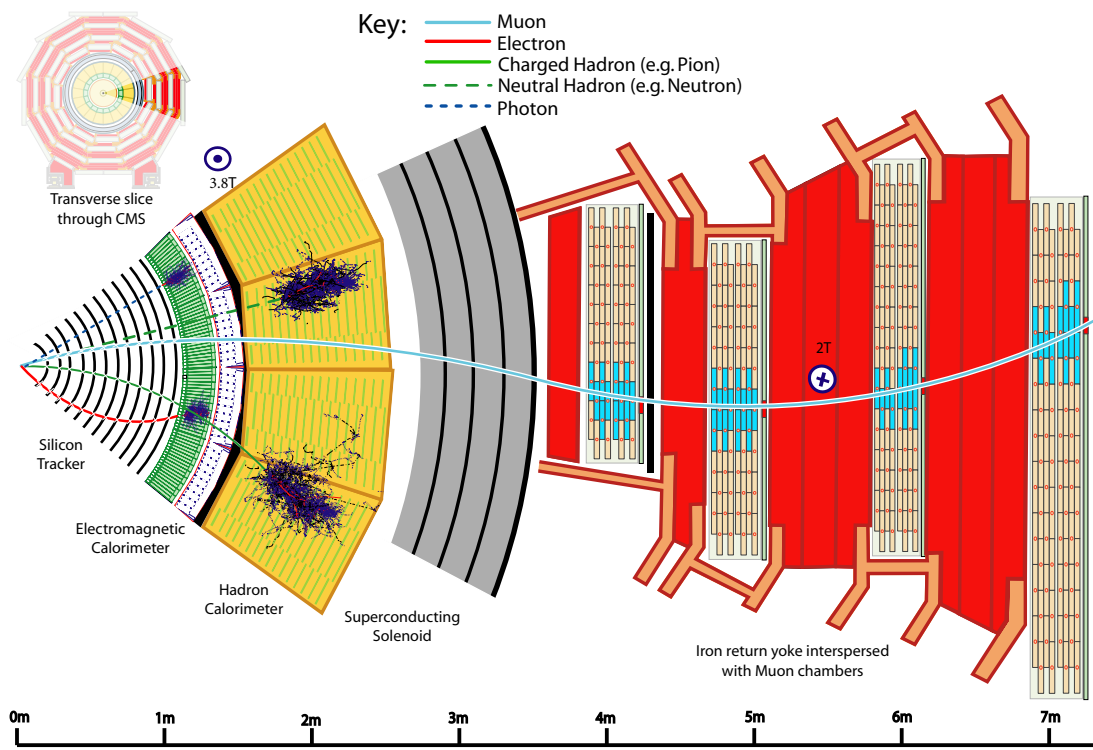


Figure 2.13: A sketch of a transverse slice of the CMS detector showing representative particle interactions [45].

## **Chapter 3: Search for displaced leptons**

### **3.1 Overview**

## 3.2 Data and simulated samples

### 3.2.1 Experimental data

This analysis uses pp collision data taken in 2016, 2017, and 2018 at a center-of-mass energy  $\sqrt{s} = 13$  TeV. In 2016, we use only the last two run periods due to lower displaced tracking efficiency caused by an analog pipeline voltage saturation problem in the silicon strip detector during the earlier run periods. In 2017, we use all run periods in the ee channel and all but the earliest run period in the  $e\mu$  and  $\mu\mu$  channels because the  $e\mu$  and  $\mu\mu$  triggers are not available in the earliest run period. In 2018, we use all available run periods in all three channels. Ultimately, this analysis uses an integrated luminosity of  $16.1 \pm 0.4 \text{ fb}^{-1}$  from 2016 in all three channels,  $41.5 \pm 1.0$  ( $36.7 \pm 0.8$ )  $\text{fb}^{-1}$  from 2017 in the ee channel ( $e\mu$  and  $\mu\mu$  channels), and  $59.7 \pm 1.5 \text{ fb}^{-1}$  from 2018 in all three channels.

### 3.2.2 Simulated background events

This analysis employs a fully data-driven background estimation technique that does not rely on simulated SM events. We do, however, use simulated SM events to study possible sources of background and verify the validity of the background estimation technique. The samples simulating Z+jets, W+jets, and  $t\bar{t}$  production are generated using MADGRAPH5\_aMC@NLO [12, 31, 14], while the samples simulating diboson and single-top-quark production are simulated with POWHEG v2 [33, 42, 32, 9, 10]. PYTHIA 8.2 [51] is used to simulate the parton showering and hadronization for all processes. The modeling of the underlying event is generated using the CUETP8M1 [38] and CP5 tunes [48] for simulated samples corresponding to the 2016 and 2017–18 data sets, respectively.

### 3.2.3 Simulated signal events

We use simulated signal events to guide the analysis strategy and interpret our results. Samples of simulated  $\text{pp} \rightarrow \tilde{t}\bar{t}$  events in which the top squarks decay to a lepton and a  $b$  quark or  $d$  quark, are produced at leading order using PYTHIA 8.2 [51]. For simplicity, all lepton flavors are generated with equal branching fractions. The top squarks can form strongly-produced hadronic states called R-hadrons, which are generated with PYTHIA. The interactions of the R-hadrons with matter are not simulated in GEANT4, but they are expected to have a negligible impact on the analysis because the lepton identification requirements effectively require the R-hadron to decay in the middle of the tracker volume. Each R-hadron therefore traverses  $\lesssim 1$  interaction length, making it unlikely to produce a high quality track, come to a stop in the detector, or flip its charge. To generate the samples, we start with a SUSY Les Houches Accord file [13] corresponding to Snowmass Points and Slopes point 1a [11] and modify the mass and width of the top squark according to the sample being produced. We generate samples with  $\tilde{t}$  masses from 100 GeV to 1800 GeV at 100 GeV intervals and with  $\tilde{t}$  lifetimes at each decade from 0.1 mm to 1 m. After producing these samples, we also employ a lifetime reweighting technique to effectively produce eight additional lifetime points between each pair of adjacent lifetimes. In the case of the 1 m samples, we also use an equivalent technique to effectively produce nine additional lifetime points between 1 and 10 m. The production cross sections for each  $\tilde{t}$  mass hypothesis are taken from the website of the LHC SUSY Cross Section Working Group. The signal samples are reconstructed in the same campaigns and with the same conditions as the SM background samples described in 3.2.2.

In addition to the signal samples described above, we also interpret our results with  $\text{pp} \rightarrow \tilde{l}\tilde{l} \rightarrow \bar{l}\tilde{G} l\tilde{G}$  and  $\text{pp} \rightarrow H \rightarrow \text{SS} \rightarrow l\bar{l} l\bar{l}$  processes. The simulated  $\text{pp} \rightarrow \tilde{l}\tilde{l} \rightarrow \bar{l}\tilde{G} l\tilde{G}$  samples are generated at leading order using `MADGRAPH5_aMC@NLO`, and the simulated  $\text{pp} \rightarrow H \rightarrow \text{SS} \rightarrow l\bar{l} l\bar{l}$  samples are generated using `POWHEG v2` and `PYTHIA 8.2` at next-to-leading order.

### 3.3 Event selection

#### 3.3.1 Triggers

The events are required to pass different triggers in each channel. Standard CMS electron and muon triggers are not designed for displaced objects, so we use non-standard triggers for both electrons and muons. For muons, we remove all trigger requirements relating to the muon transverse or longitudinal impact parameter or the vertex from which the muon originates. For electrons, we actually use photon triggers, which collect events with electrons as well as photons but do not rely on any tracking information.

In the  $e\mu$  channel, 2016 data and corresponding MC simulation events are required to pass the logical OR of two HLT paths (`HLT_Mu38NoFiltersNoVtx_Photon38_CaloIdL_v*` OR `HLT_Mu28NoFiltersNoVtxDisplaced_Photon28_CaloIdL_v*`) that were both designed for this analysis. These triggers require at least one L3 muon with  $p_T > 38(28)$  GeV without any constraints on the vertex or upper bound on the transverse or longitudinal impact parameter. The second trigger requires that the absolute value of the L3 muon transverse impact parameter is greater than 0.01. Each of these two triggers also requires at least one photon with loose calorimeter ID and  $E_T > 38(28)$  GeV. The HLT paths are seeded by `L1_Mu5_EG20` OR `L1_Mu20_EG15`. The signal efficiency with these dedicated triggers is significantly higher than that of standard muon-photon HLT paths.

2017 and 2018 data and corresponding MC simulation events in the  $e\mu$  channel are required to pass `HLT_Mu43NoFiltersNoVtx_Photon43_CaloIdL_v*`. The muon  $p_T$  and photon  $E_T$  thresholds were raised with respect to 2016 due to increased pileup.

Unlike in 2016, the version of this trigger that requires displaced muons was not available.

In the ee channel, 2016 data and corresponding MC simulation events are required to pass the logical OR of two HLT paths (`HLT_Diphoton30_18_R9Id_OR_IsoCaloId_AND_HE_R9Id_Mass90_v*` OR `HLT_DoublePhoton60_v*`). The first requires a leading photon with  $E_T > 30$  GeV and a subleading photon with  $E_T > 18$  GeV. Calorimeter identification, isolation,  $H/E$ , and  $R_9$  requirements are made on both photons, and the diphoton invariant mass must be  $> 90$  GeV. This HLT path is seeded by a suite of single-photon and double-photon L1 seeds. This path is highly efficient at low  $\tilde{t}$  mass. The second trigger simply requires at least two photons with  $E_T > 60$  GeV. This HLT path is seeded by a suite of nonisolated single-photon, double-photon, single-jet, and single-tau-jet L1 seeds. This path is highly efficient at large  $\tilde{t}$  mass and lifetime.

2017 and 2018 data and corresponding MC simulation events are required to pass `HLT_Diphoton30_22_R9Id_OR_IsoCaloId_AND_HE_R9Id_Mass90_v*` OR `HLT_DoublePhoton70_v*`. The photon  $E_T$  thresholds were raised with respect to 2016 due to increased pileup.

In the  $\mu\mu$  channel, 2016 data and corresponding MC simulation events are required to pass the logical OR of two HLT paths (`HLT_DoubleMu33NoFiltersNoVtx_v*` OR `HLT_DoubleMu23NoFiltersNoVtxDisplaced_v*`), that were both designed for this analysis. These triggers require at least two L3 muons with  $p_T > 33(23)$  GeV without any constraints on the vertex or upper bound on the transverse or longitudinal impact parameter. The second trigger requires that the L3 muon transverse impact parameter is greater than 0.01. The HLT paths are seeded by the lowest  $p_T$  threshold

unprescaled double-muon L1 seeds. The signal efficiency with these dedicated triggers is significantly higher than that of standard dimuon HLT paths.

2017 and 2018 data and corresponding MC simulation events are required to pass `HLT_DoubleMu43NoFiltersNoVtx_v*`. The muon  $p_T$  threshold was raised with respect to 2016 due to increased pileup. Unlike in 2016, the version of this trigger that requires displaced muons was not available.

### 3.3.2 Preselection

Starting from the events collected with the triggers described above, we next apply a preselection that selects the events to be analyzed. The preselection criteria vary by channel and year, but the fundamental goal is always to select events with at least one good offline reconstructed lepton of each flavor required by the channel.

The preselection selects events with at least one good particle flow (PF) electron and at least one good global PF muon [45] in the  $e\mu$  channel, events with at least two good PF electrons in the ee channel, and events with at least two good global PF muons in the  $\mu\mu$  channel. We set requirements on these electrons and muons as shown in Tables 3.1, 3.2 and 3.3. The electron and muon  $p_T$  requirements are chosen to be in the plateau of the trigger turn-on curve, and electron and muon  $|\eta|$  requirements are chosen to remove leptons with poorly measured transverse impact parameter, which are more common at large  $|\eta|$  (see Appendix B for further discussion). Electrons that traverse the gap between the endcap and barrel detectors are also rejected due to the known loss of reconstruction performance in this region.

We use tight cut-based identification (ID) on the electrons and muons to select well-reconstructed leptons, but unlike the standard ID definitions used in many CMS

Table 3.1: The  $e\mu$  preselection criteria. The electron and muon  $p_T$  thresholds increased in 2017 because the HLT electron and muon  $p_T$  thresholds increased.

Selection variable	Object-level selections		Event-level selections
	Electron	Muon	
Number	$\geq 1$	$\geq 1$	Zero $\mu\mu$ pairs with $\cos \alpha < -0.99$
$p_T$	$> 42 \text{ GeV}$ (2016) $> 45 \text{ GeV}$ (2017 and 2018)	$> 40 \text{ GeV}$ (2016) $> 45 \text{ GeV}$ (2017 and 2018)	Reject $\Delta t < -20$ , if both timing ndof $> 7$
$ \eta $	$< 1.5$	$< 1.5$	At least one $e\mu$ pair with $\Delta R(e, \mu) > 0.2$
	not in ECAL gap	-	Reject events where the candidate electron and muon form a good displaced vertex that overlaps with the tracker material
$\eta - \phi$ (pixel power supply issue)	veto ( $1.0 < \eta < 1.5$ and $\phi > 2.7$ ) (2017) veto ( $0.3 < \eta < 1.2$ and $0.4 < \phi < 0.8$ ) (2018)	veto ( $1.0 < \eta < 1.5$ and $\phi > 2.7$ ) (2017) veto ( $0.3 < \eta < 1.2$ and $0.4 < \phi < 0.8$ ) (2018)	
ID	Tight (cut-based)	Tight (cut-based)	
Custom isolation	Tight	Tight	

Table 3.2: The ee preselection criteria. The electron  $p_T$  threshold increased in 2017 and 2018 because the HLT electron  $p_T$  threshold increased at the start of 2017.

Selection variable	Object-level selections
Number	Event-level selections
$p_T$	$\geq 2$ $> 65 \text{ GeV (2016)}$ $> 75 \text{ GeV (2017 and 2018)}$
$ \eta $	$< 1.5$ not in ECAL gap
$\eta - \phi$ (pixel power supply issue)	veto ( $1.0 < \eta < 1.5$ and $\phi > 2.7$ ) (2017) veto ( $0.3 < \eta < 1.2$ and $0.4 < \phi < 0.8$ ) (2018)
ID	Tight (cut-based)
Custom isolation	Tight
	Event-level selections
	At least one ee pair with $\Delta R(e, e) > 0.2$
	Reject events where the candidate electrons form a good displaced vertex that overlaps with the tracker material
	Reject events with displaced muons in the $e\mu$ channel inclusive signal region

Table 3.3: The  $\mu\mu$  preselection criteria. The muon  $p_T$  threshold increased in 2017 and 2018 because the HLT muon  $p_T$  threshold increased at the start of 2017.

Selection variable		Object-level selections	
Number	Muon		
	$\geq 2$		
$p_T$		$> 35 \text{ GeV}$ (2016)	
		$> 45 \text{ GeV}$ (2017 and 2018)	
$ \eta $	$< 1.5$		
		veto ( $1.0 < \eta < 1.5$ and $\phi > 2.7$ ) (2017)	
		veto ( $0.3 < \eta < 1.2$ and $0.4 < \phi < 0.8$ ) (2018)	
ID		Tight (cut-based)	
Custom isolation	Tight		
		Event-level selections	
		Zero $\mu\mu$ pairs with $\cos\alpha < -0.99$	
		Reject $\Delta t < -20$ , if both timing ndof $> 7$	
		At least one $\mu\mu$ pair with $\Delta R(\mu, \mu) > 0.2$	
Reject events where the candidate muons form a good displaced vertex that overlaps with the tracker material			
Reject events with displaced electrons in the $e\mu$ channel inclusive signal region			

Table 3.4: The electron tight ID requirements. They are identical to the tight cut-based ID from the egamma POG, except we remove any requirements on  $d_0$  or the longitudinal impact parameter [27].

	Electron ID requirements	
	$ \eta_{\text{supercluster}}  \leq 1.479$	$ \eta_{\text{supercluster}}  > 1.479$
full5x5 $\sigma I\eta I\eta <$	0.0104 (2018, 2017) 0.00998 (2016)	0.0353 (2018, 2017) 0.0292 (2016)
$ \delta\eta_{\text{Seed}}  <$	0.00255 (2018) 0.00353 (2017) 0.00308 (2016)	0.00501 (2018) 0.00567 (2017) 0.00605 (2016)
$ \delta\phi_{\text{In}}  <$	0.022 (2018) 0.0499 (2017) 0.0816 (2016)	0.0236 (2018) 0.0165 (2017) 0.0394 (2016)
H/E <	0.026 + 1.15/E + 0.0324 $\rho$ /E (2018) 0.026 + 1.12/E + 0.0368 $\rho$ /E (2017) 0.0414 (2016)	0.0188 + 2.06/E + 0.18 $\rho$ (2018) 0.026 + 0.5/E + 0.201 $\rho$ (2017) 0.0641 (2016)
Rel. comb. PF iso with EA corr <	0.0287 + 0.506/ $p_T$ (2018) 0.0361 (2017) 0.0588 (2016)	0.0445 + 0.963/ $p_T$ (2018) 0.094 (2017) 0.0571 (2016)
$ 1/E - 1/p  <$	0.159 (2018) 0.0278 (2017) 0.0129 (2016)	0.0197 (2018) 0.0158 (2017) 0.0129 (2016)
expected missing inner hits $\leq$	1	1
pass conversion veto	yes	yes

analyses, we do not place any requirements on the transverse and longitudinal impact parameters. For electrons, the ID corresponds to the `egmGsfElectronIDs:cutBasedElectronID-Summer16-80X-V1-tight` in 2016, `egmGsfElectronIDs:cutBasedElectronID-Fall17-94X-V1-tight` in 2017, and `egmGsfElectronIDs:cutBasedElectronID-Fall17-94X-V2-tight` in 2018 [27]. The electron and muon tight ID requirements are summarized in Tables 3.4 and 3.5.

Table 3.5: The muon tight ID requirements. They are identical to the tight cut-based ID from the muon Physics Object Group, except we remove any requirements on  $d_0$  or  $d_z$  [41].

Muon ID requirements
Is a global muon
Is a PF muon
$\chi^2/n_{\text{dof}}$ of the global-muon track fit is $< 10$
At least one muon-chamber hit included in the global-muon track fit
Muon segments in at least two muon stations
At least 1 valid pixel hit
At least 6 tracker layers with hits

We require tight PF isolation on the electrons and muons. However, we use a modified isolation definition that accounts for the fact that displaced leptons may be associated with the wrong primary vertex. The standard PF isolation assumes all energy from primary vertices other than the leading primary vertex is due to pileup, which is not true when the primary vertex ordering is altered by an incorrectly associated lepton. We have therefore modified the pileup correction to be agnostic to the primary vertex ordering by allowing PF candidates from any primary vertex to contribute to the isolation sum and by using a simple  $\rho$ -based pileup correction, where  $\rho$  is the total transverse energy of all the PF candidates divided by the total detector area. Figure 3.1 shows how the size of the pileup correction term depends on lepton displacement in the standard isolation but not in the modified isolation described here. We use the modified isolation definition for both electrons and muons while keeping the original tight working point for electrons and slightly tightening the tight working point for muons. In the end, we require that the relative isolation is  $< 0.10$  for muons and  $< 0.0588$  (0.0571) for electrons in the barrel (endcap) in 2016

and  $< 0.0287 + 0.506/p_T$  ( $0.0445 + 0.963/p_T$ ) for electrons in the barrel (endcap) in 2017 and 2018. As shown in Fig. 3.2 and Fig. 3.3, this modified PF isolation rejects substantially more background when the leptons are displaced without significantly altering the signal yield. We note, however, that there may still be some minor dependence on the primary vertex selection in the PF muon requirement because the PF muon selection includes some loose isolation requirements where the charged hadron component is constrained to the selected primary vertex.

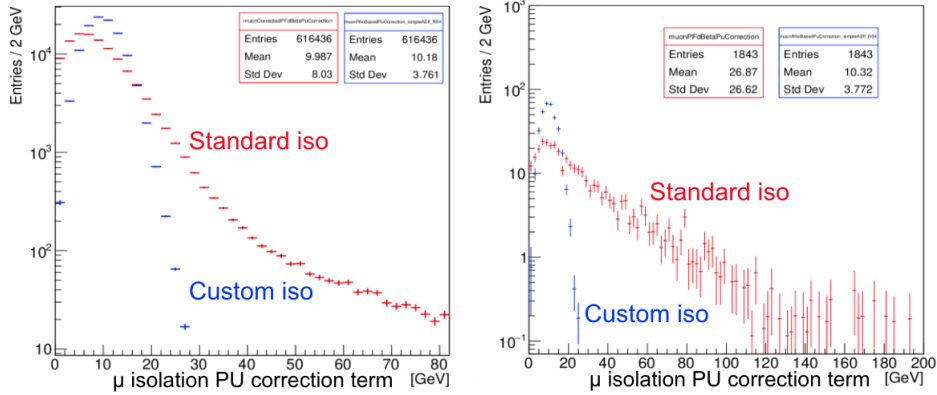


Figure 3.1: The muon isolation pileup correction term, for the standard muon isolation and the modified muon isolation in simulated  $t\bar{t}$  events that pass the  $e\mu$  preselection in 2018 conditions. The plot on the left is for muon  $|d_0| < 100 \mu\text{m}$ , and the plot on the right is for muon  $500 < |d_0| < 1000 \mu\text{m}$ .

We also reject electrons and muons in certain regions of the  $\eta-\phi$  plane where lepton  $|d_0|$  is more likely to be mismeasured. We identify these regions as highly populated bins in the electron  $\eta-\phi$  distribution in a prompt-muon, displaced-electron control region in 2017 and 2018 data. No such bins are present in 2016 data. The identified regions coincide with regions found by a previous CMS analysis [49] to be affected by power supply issues in the pixel detector. The  $\eta - \phi$  variation is more

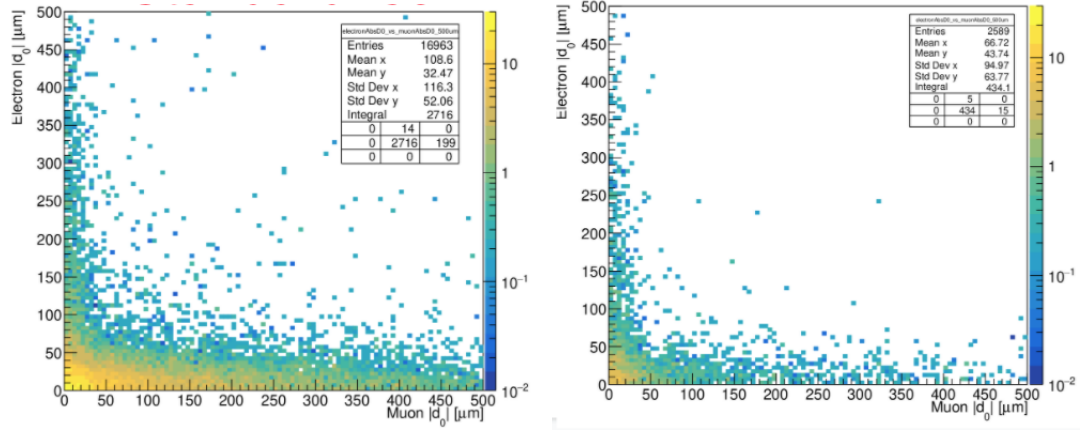


Figure 3.2: The electron  $|d_0|$  versus the muon  $|d_0|$ , for  $t\bar{t}$  simulated events that pass the  $e\mu$  preselection and where at least one lepton comes from a heavy-flavor meson. The plot on the left uses the standard isolation, and the plot on the right uses the modified isolation.

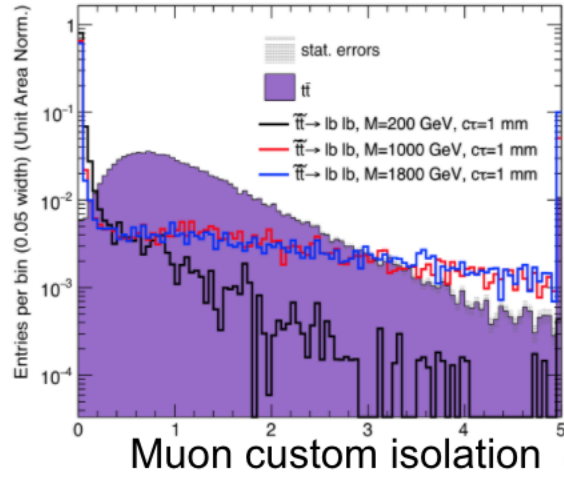


Figure 3.3: The muon custom isolation distribution for  $t\bar{t}$  background simulation and signal simulation in 2018 conditions.

apparent for displaced electrons than displaced muons, so we use data in a prompt muon ( $|d_0| < 40 \mu\text{m}$ ), displaced electron ( $100 < |d_0| < 500 \mu\text{m}$ ) control region to define the regions used for both electrons and muons. In 2017, the rejected region is  $1.0 < \eta < 1.5$ ,  $\phi > 2.7$ , and in 2018 the rejected region is  $0.3 < \eta < 1.2$ ,  $0.4 < \phi < 0.8$ .

In addition to these object-level selections, we also impose a few event-level selections designed to remove potential backgrounds from cosmic rays, material interactions, and displaced decays of SM hadrons. To remove cosmic-ray muons in the  $\mu\mu$  and  $e\mu$  channels, we require there be zero pairs of muons with  $\cos \alpha < -0.99$ , where  $\alpha$  is the 3D angle between the muons, and that the relative time between the leading two muons is inconsistent with the timing of cosmic-ray muons. To do this, we look at the muon time as measured at the IP from the DTs and CSCs, assuming the muons are traveling outwards from the center of the detector. We then use the muon  $\phi$  measurements to determine which muon is above the other and find  $\Delta t$ , the time of the lower muon subtracted from the time of the upper muon. We reject events with  $\Delta t < -20$  if the number of degrees of freedom of the timing measurements for both muons is greater than seven. To remove leptons from decays of SM hadrons, we require that the candidate leptons not be too close together in the  $\eta$ - $\phi$  plane. Specifically, we find that requiring  $\Delta R > 0.2$  significantly reduces the contribution from SM hadrons without noticeably affecting the signal acceptance. To remove leptons from material interactions, we reject events in which the candidate leptons form a good displaced vertex that overlaps with the tracker material. The vertices are reconstructed with the Kalman Vertex Fitter, and a “good” vertex is one with  $\chi^2/\text{n}_{\text{dof}} < 20$ . The tracker material map is obtained from the tracker material budget measurements [47, 24].

See Section 3.4.6 for tests in data that involve inverting the criteria described in this paragraph.

Finally, to ensure that the signal regions of all three channels are orthogonal to one another, we reject events in the ee ( $\mu\mu$ ) channel with at least one muon (electron) that passes the  $e\mu$  channel preselection and has  $|d_0| > 100 \mu\text{m}$ .

In contrast to the 2015 analysis [20], we allow for the possibility of more than one lepton of each type in a given channel and set no requirements on the charge product of the lepton pair. These changes were made at the request of several theorists, including the authors of Ref. [29].

### 3.3.3 Prompt control region

In order to verify the implementation of our selection and corrections to simulation (see Section 3.5), we define a prompt control region that is dominated by SM background events. Events in each channel’s prompt control region are selected by requiring that they pass all of the criteria defined in Section 3.3.2 as well as the requirement that the candidate leptons have  $|d_0| < 50 \mu\text{m}$ . We define this region in each channel in order to check for reasonable agreement between simulated SM events and data after applying the corrections described in Section 3.5. Some examples are shown in Figures 3.4, 3.5, and 3.6, which show the  $p_{\text{T}}$ ,  $\eta$ , and  $|d_0|$  distributions of the leptons in the  $e\mu$ , ee, and  $\mu\mu$  prompt control regions, respectively, for 2016 data and MC simulation. The data-driven background estimation technique employed in this analysis removes the need for exact agreement between data and simulation, but the absence of any significant discrepancies gives us confidence that we are accounting

for the correct sources of prompt SM leptons and that our selection and corrections are functioning as intended.

### 3.3.4 Inclusive signal region

Finally, we define inclusive signal region, which is the region in which new physics may contribute significantly. The inclusive signal region is populated by events that pass all of the criteria defined in Section 3.3.2 as well as the requirement that the candidate leptons each have  $100 \mu\text{m} < |d_0| < 10 \text{ cm}$ . We do not select leptons with  $|d_0| > 10 \text{ cm}$  because the tracking efficiency drops sharply after this point, as shown in Section C. This requirement also ensures that the leptons originate within the pixel volume, which is effectively required by the pixel hit requirement of the tight lepton IDs. To ensure sensitivity to a wide range of new particle masses and lifetimes, we further subdivide the inclusive signal region into bins defined by the  $|d_0|$  of each candidate lepton and the  $p_{\text{T}}$  of one candidate lepton. The exact binning is described in Section 3.4.2.

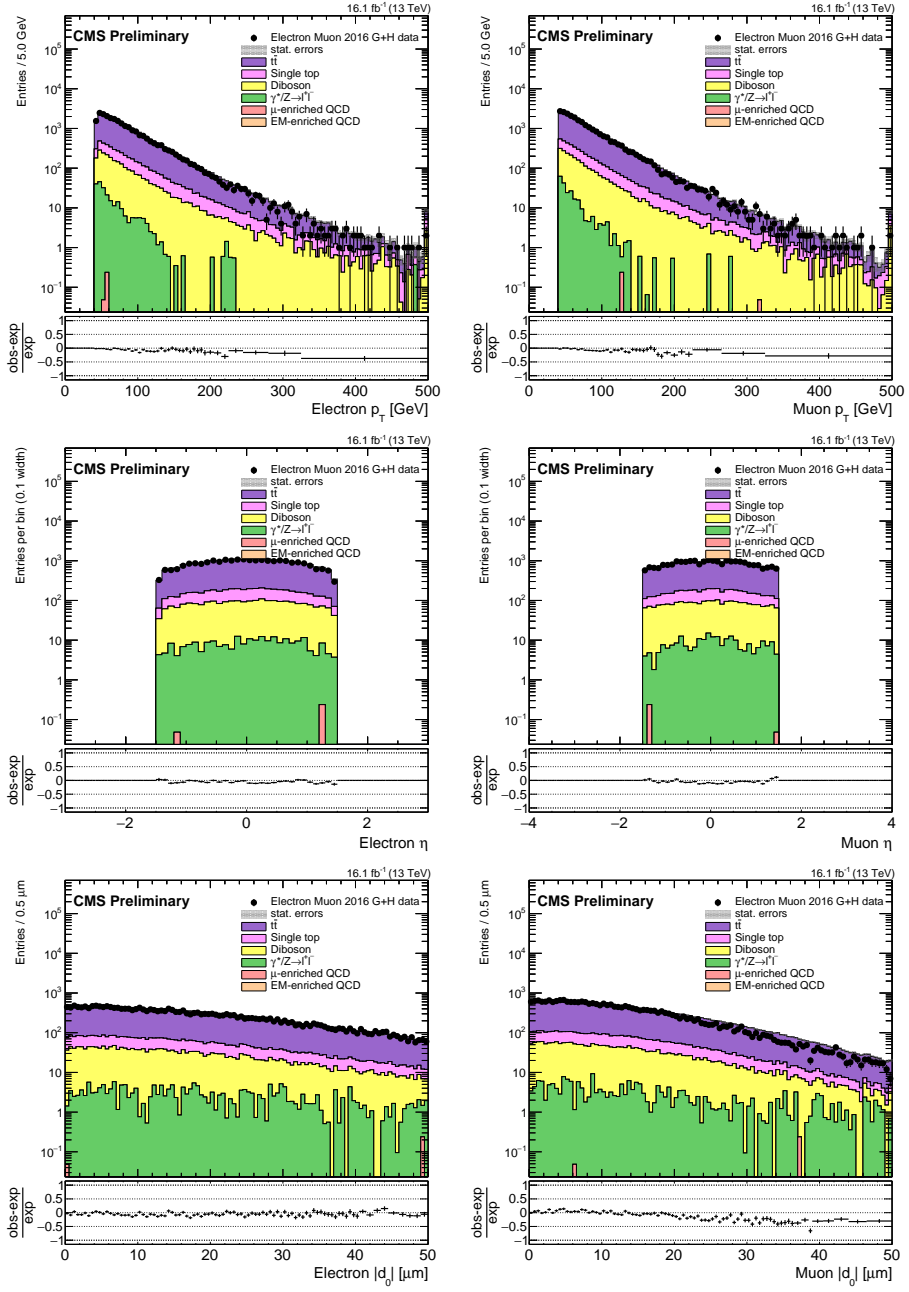


Figure 3.4: The lepton  $p_T$  (upper),  $\eta$  (middle), and  $|d_0|$  (lower) distributions in the  $e\mu$  prompt control region, for electrons (left) and muons (right), for 2016 data and MC simulation. The rightmost bin in each plot contains the overflow entries.

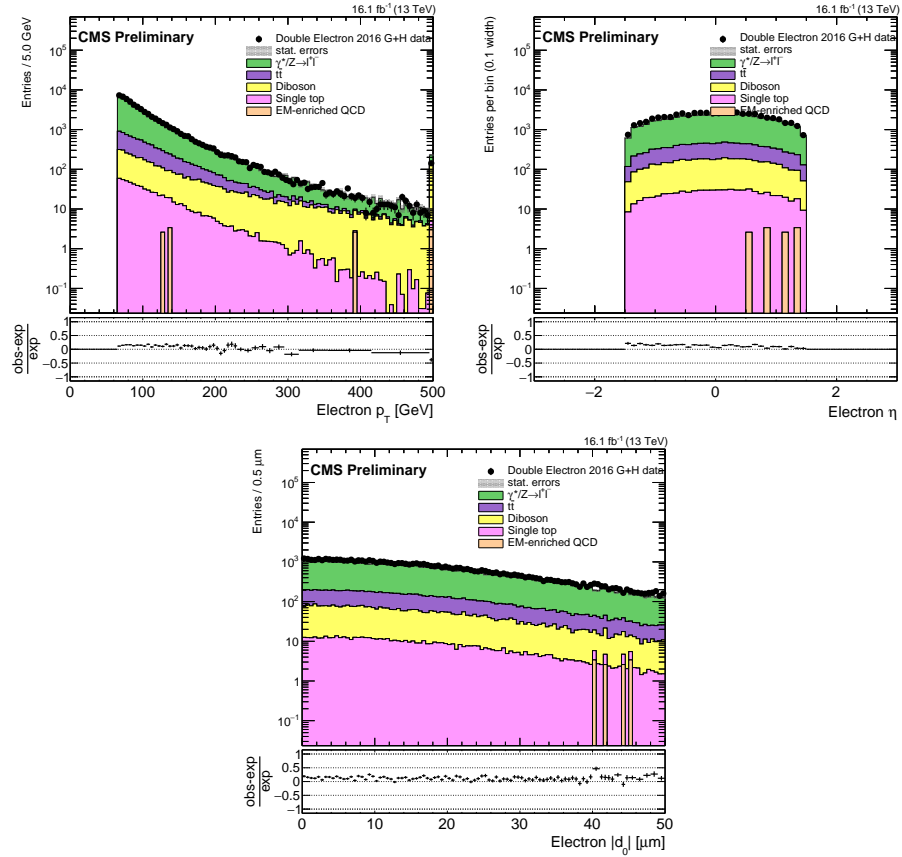


Figure 3.5: The electron  $p_T$  (left),  $\eta$  (lower), and  $|d_0|$  (right) distributions in the ee prompt control region for 2016 data and MC simulation. The rightmost bin in each plot contains the overflow entries.

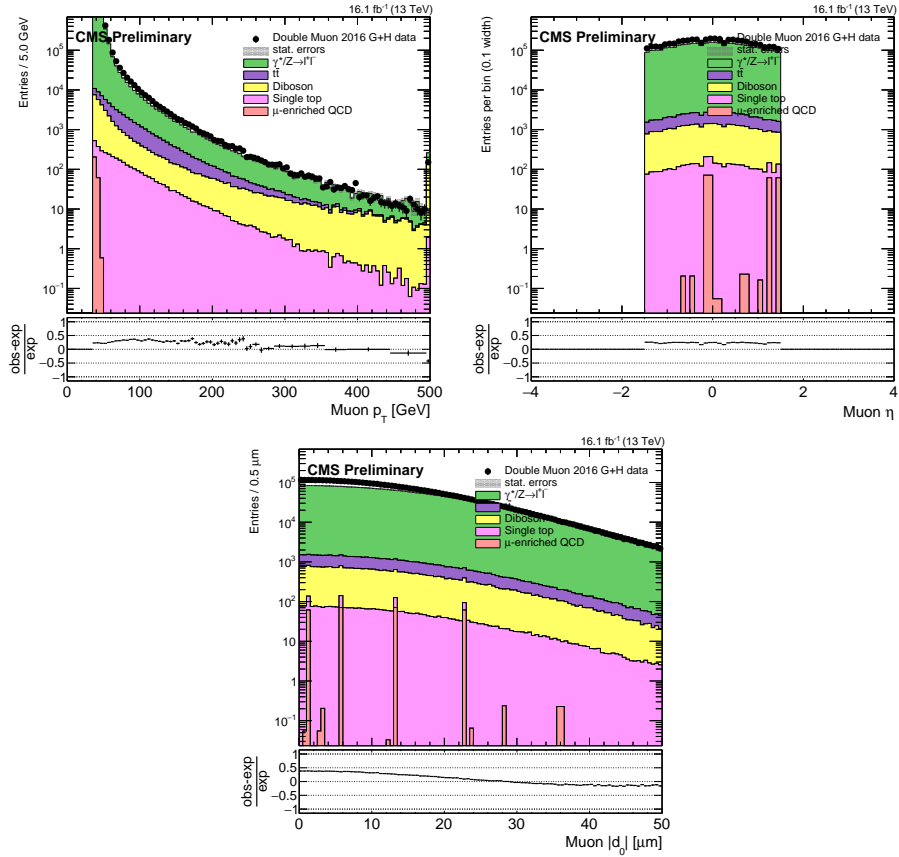


Figure 3.6: The muon  $p_T$  (left),  $\eta$  (lower), and  $|d_0|$  (right) distributions in the  $\mu\mu$  prompt control region for 2016 data and MC simulation. The rightmost bin in each plot contains the overflow entries.

## 3.4 Background estimation

### 3.4.1 Background sources

The vast majority of leptons from SM processes are prompt. There are, however, a few notable processes that produce leptons with large  $|d_0|$  values that may pass our selection: (1) leptons from prompt decays whose  $|d_0|$  is poorly measured ("mismeasurements"), (2) leptons from decays of tau leptons ("taus"), and (3) leptons from decays of B or D mesons ("HF"). Note that the leptons from these processes generally do not share a common displaced vertex. We perform several cross checks to ensure that processes in which leptons share a common displaced vertex do not contribute significantly in the SRs. Section 3.4.6 presents several additional studies that confirm that the SR contribution of leptons from material interactions, cosmic rays, and SM hadrons are either negligible or already accounted for by the background estimation procedure.

The  $|d_0|$  distributions of leptons from the three main background sources vary both by lepton flavor and parent particle. Tau leptons have a lifetime of  $87\,\mu\text{m}$ , B mesons have a lifetime around  $500\,\mu\text{m}$ , and D mesons have a lifetime of around  $100\,\mu\text{m}$ , so leptons from taus will generally have smaller  $|d_0|$  values than leptons from HF. Furthermore, mismeasurements are more common for electrons than for muons due to the superior muon  $d_0$  resolution. Figure 3.7, which shows the relative contribution of each source of leptons as a function of  $|d_0|$  in simulated  $t\bar{t}$  events that pass the  $e\mu$  channel preselection, shows how mismeasurements dominate at all  $|d_0|$  values for electrons while taus and HF contribute meaningfully for muons with  $\gtrsim 100\,\mu\text{m}$ .

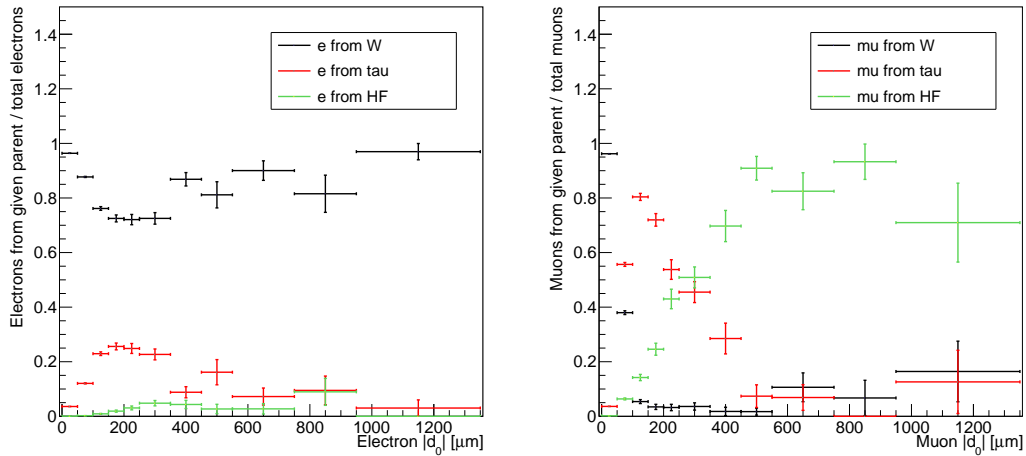


Figure 3.7: The fraction of electrons (left) and muons (right) from different parents as a function of lepton  $|d_0|$ , for simulated  $t\bar{t}$  events that pass the 2018  $e\mu$  channel preselection.

In the  $\mu\mu$  channel, it is worth examining which long-lived SM parents will contribute to  $|d_0|$ - $|d_0|$  correlation. The correlation specifically comes from DY-type processes in which the parentage is correlated between muons. Figure 3.8, which shows the fraction of muons from different background sources in DY simulation, indicates that tau lepton decays are the main source of muons that may be correlated in this way, and that the heavy-flavor contribution is negligible. This is reasonable because while tau leptons and heavy-flavor mesons both produce displaced muons, the isolation criteria rejects the vast majority of muons from heavy-flavor mesons. Muons from tau leptons contribute significantly from about 100 to 500  $\mu\text{m}$ , so we expect the most significant  $|d_0|$ - $|d_0|$  correlation to appear in this range and peak around 200  $\mu\text{m}$ . Furthermore, the correlation will be most pronounced in the regions where the  $|d_0|$  measurements are the best.

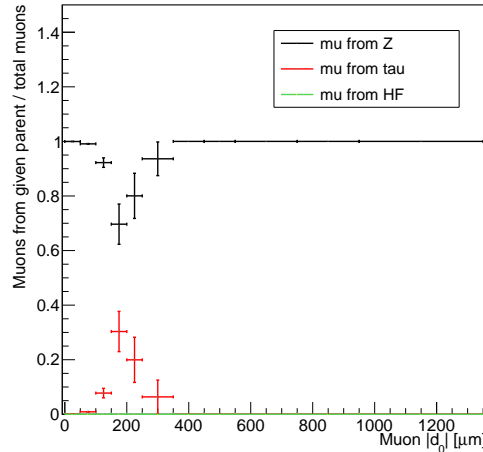


Figure 3.8: The fraction of muons from different parents as a function of muon  $|d_0|$ , for simulated DY events that pass the 2018  $\mu\mu$  channel preselection.

### 3.4.2 Data-driven ABCD method

We estimate the SR background yields with a data-driven method in which the lepton  $|d_0|$  distributions serve as composite models of all background processes. Specifically, we employ an ABCD method using the  $|d_0|$  of two leptons. We label the two  $|d_0|$  values in each channel as  $|d_0^a|$  and  $|d_0^b|$ , which correspond to the leading e and leading  $\mu$  in the  $e\mu$  channel, the leading and subleading e in the ee channel, and the leading and subleading  $\mu$  in the  $\mu\mu$  channel. As a first step, we categorize the events that pass the preselection criteria into four regions (A, B, C, and D) of the  $|d_0^a|-|d_0^b|$  plane, as shown in Fig. 3.9.

We then use the number of events in regions A, B, and C to estimate the expected background in each SR. The basic estimation procedure depends on the assumption that  $|d_0^a|$  and  $|d_0^b|$  are uncorrelated. If this assumption holds, then  $N_B/N_A = N_D/N_C$  and the number of background events in D is equal to  $N_B N_C / N_A$ , where  $N_X$  is the

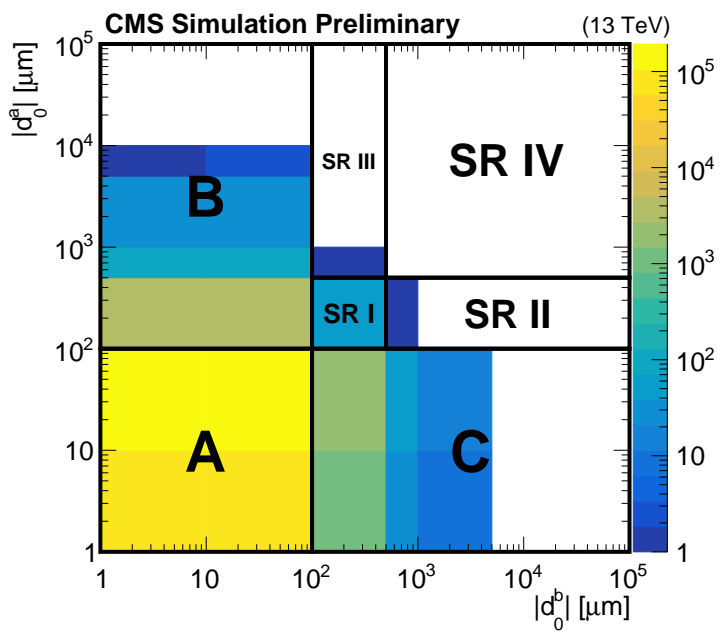


Figure 3.9: A diagram of the ABCD method overlaid on simulated background events passing the 2018  $e\mu$  preselection. A, B, and C are control regions, and D is the inclusive SR, which includes SRs I, II, III, and IV. Underflow events are included in the bins along the left and bottom edges.

number of background events in the given region. We find that  $|d_0^a|$  and  $|d_0^b|$  are indeed uncorrelated over much of the  $|d_0|$ - $|d_0|$  plane, but the correlation discussed in Section 3.4.1 renders the basic ABCD method insufficient to estimate the background in SR I. After quantifying the degree of correlation in Section 3.4.3, we define a procedure to correct the basic ABCD estimate in Section 3.4.4.

In order to maximize sensitivity to a wide range of new particle lifetimes, we further subdivide region D into the following four signal regions (SRs):

- SR I:  $100 \leq \text{both } |d_0| < 500 \mu\text{m}$
- SR II:  $100 \leq |d_0^a| < 500 \mu\text{m}$ ,  $500 \mu\text{m} < |d_0^b| < 10 \text{ cm}$
- SR III:  $500 \mu\text{m} \leq |d_0^a| < 10 \text{ cm}$ ,  $100 < |d_0^b| < 500 \mu\text{m}$
- SR IV:  $500 \mu\text{m} \leq \text{both } |d_0| < 10 \text{ cm}$

The exact boundaries between the four SR are motivated by the expected contributions of the different background sources, as explained in 3.4.1. This approach also necessitates that the definitions of regions B and C vary in accordance with the SR for which a given estimate is performed (e.g. only the events in the  $100 \leq |d_0^a| < 500 \mu\text{m}$  range of region B are considered when estimating the yields of SR I and II). Finally, we subdivide SR I into two bins using one lepton's  $p_T$  to further increase sensitivity to high-mass, low-lifetime new physics. Table 3.17 lists the  $p_T$  boundary in each channel and year.

When performing the background estimate and closure tests, we treat the 2016 data and simulation separately from the 2017–2018 data and simulation to avoid any correlations between  $|d_0^a|$  and  $|d_0^b|$  that may arise from the differences between the

Phase 0 and Phase 1 trackers employed by CMS in 2016 and 2017–2018, respectively (see Section 2.2.2).

### 3.4.3 Closure tests in control regions

We perform several closure tests of the background estimation procedure in data and simulation to test the method and quantify the degree of  $|d_0^a|$ - $|d_0^b|$  correlation from the processes discussed in 3.4.1. Two series of tests are performed, the first in the 100–500  $\mu\text{m}$  subregions of regions B and C and the second in the 500  $\mu\text{m}$ –10 cm subregions of regions B and C.

#### 100–500 $\mu\text{m}$ tests

We perform closure tests in subregions of regions B and C where one lepton is more prompt (20–100  $\mu\text{m}$ ) and the other is more displaced (100–500  $\mu\text{m}$ ). In these closure tests, we estimate the background yield using the simple ABCD method and then use the ratio of the actual number of events to the estimated number of events as the measure of nonclosure (and therefore  $|d_0^a|$ - $|d_0^b|$  correlation). With this approach, a ratio of 1 corresponds to closure and no  $|d_0^a|$ - $|d_0^b|$  correlation while ratios greater than 1 correspond to nonclosure and positive  $|d_0^a|$ - $|d_0^b|$  correlation. Using the procedure outlined in 3.4.4, we estimate the corresponding degree of nonclosure in SR I by fitting the resulting ratios and extrapolating from the closure test regions to SR I. We perform identical procedures in regions B and C and then average the resulting extrapolated ratios.

Table 3.6 shows the average extrapolated ratios for three rounds of closure tests: one in background simulation with the  $Z \rightarrow \tau\tau \rightarrow ll$  events removed, one in the full background simulation, and one in data. The average extrapolated ratios are always

compatible with one in background simulation without  $Z \rightarrow \tau\tau \rightarrow ll$  events, but they generally increase when the  $Z \rightarrow \tau\tau \rightarrow ll$  events are included. Furthermore, the average extrapolated ratios from the full background simulation generally describe the average extrapolated ratios in data. From these results, we conclude that within our statistical uncertainties,  $Z \rightarrow \tau\tau \rightarrow ll$  events are the only meaningful source of correlation and that the degree of correlation observed in data is modeled reasonably well in simulation. We also observe that the variation in the degree of correlation across channels matches our expectations: correlation increases with the number of muons in the final state and is greater in 2017–2018 than 2016 because of the improved  $d_0$  resolution made possible by the Phase 1 tracker upgrade (see Section 2.2.2).

Table 3.6: Closure test results in background simulation (with and without  $Z \rightarrow \tau\tau \rightarrow ll$  events) and in data, in the 100–500  $\mu\text{m}$  region. The average extrapolated ratios and their statistical uncertainties are given. The A, B, C, and D regions are defined as follows: A is 20–30  $\mu\text{m}$  in prompt lepton  $|d_0|$  and 20–100  $\mu\text{m}$  in displaced lepton  $|d_0|$ , B is 20–30  $\mu\text{m}$  in prompt-lepton  $|d_0|$  and 100–500  $\mu\text{m}$  in displaced lepton  $|d_0|$ , C is always 20–100  $\mu\text{m}$  in displaced lepton  $|d_0|$ , D (the test region) is always 100–500  $\mu\text{m}$  in displaced lepton  $|d_0|$ , and we perform repeated tests while simultaneously varying the C and D prompt lepton  $|d_0|$ s within the 30–100  $\mu\text{m}$  range.

	Bkg. simulation without $Z \rightarrow \tau\tau \rightarrow ll$	Full bkg. simulation	Data
2016 e $\mu$	$0.9 \pm 0.3$	$1.6 \pm 0.6$	$0.9 \pm 1.3$
2017+2018 e $\mu$	$1.1 \pm 0.4$	$1.6 \pm 0.7$	$3.0 \pm 1.0$
2016 ee	$0.8 \pm 0.5$	$0.8 \pm 0.5$	$0.6 \pm 0.6$
2017+2018 ee	$0.8 \pm 1.0$	$1.6 \pm 0.9$	$1.5 \pm 0.4$
2016 $\mu\mu$	$1.1 \pm 0.8$	$2.0 \pm 0.8$	$2.5 \pm 1.0$
2017+2018 $\mu\mu$	$2.6 \pm 2.8$	$7.8 \pm 3.7$	$4.2 \pm 1.8$
Average	$1.2 \pm 0.5$	$2.6 \pm 0.7$	$2.1 \pm 0.5$

### **500 $\mu\text{m}$ –10 cm tests**

We next perform closure tests in subregions of regions B and C where one lepton is more prompt ( $20\text{--}100\,\mu\text{m}$ ) and the other is more displaced ( $500\,\mu\text{m}$ –10 cm). We again use the ratio of the actual number of events to the estimated number of events as the measure of nonclosure, but in these tests we expect the ratio to be consistent with one because  $Z \rightarrow \tau\tau \rightarrow ll$  events do not contribute meaningfully beyond  $500\,\mu\text{m}$ . Table 3.7 shows that this is indeed the case for background simulation (with and without  $Z \rightarrow \tau\tau \rightarrow ll$  events) and for data. These results imply that  $|d_0^a|$  and  $|d_0^b|$  are uncorrelated beyond  $500\,\mu\text{m}$ , which means that a simple ABCD procedure will be adequate for estimating the background yields in SRs II, II, and IV.

#### **3.4.4 ABCD correction and systematic uncertainty**

The closure tests of Section 3.4.3 show that  $|d_0^a|$  and  $|d_0^b|$  are frequently positively correlated in the  $100\text{--}500\,\mu\text{m}$  region but are uncorrelated otherwise. To account for this correlation as well as other possible unforeseen sources of nonclosure, we define a procedure to correct the simple ABCD estimate in SR I and assign a systematic uncertainty to the simple ABCD estimate in all SRs.

#### **100–500 $\mu\text{m}$ correction and systematic uncertainty**

Figures 3.10, 3.11, and 3.12 show the results of the closure tests in the  $e\mu$ ,  $ee$ , and  $\mu\mu$  channels, respectively, in the one-prompt ( $20\text{--}100\,\mu\text{m}$ )/one-displaced ( $100\text{--}500\,\mu\text{m}$ ) sidebands in the  $100\text{--}500\,\mu\text{m}$  region, in data. These plots show the ratio of the actual to the estimated number of events as a function of the prompt lepton  $|d_0|$ . In all of these plots, the binning of the prompt lepton axis is initially  $10\,\mu\text{m}$  wide. Starting from most-displaced bin, we test to see if any bin has fewer than 5 events,

and if so, we combine it with whichever neighboring bin has fewer events, repeating until all bins have at least 5 events.

We then fit the data with a straight line, where the slope and y-intercept are allowed to vary. This fit is used to find the ratio at  $200\,\mu\text{m}$  (the extrapolation into SR I), which is where we expect the largest contribution from tau lepton decays, as was shown in Section 3.4.1.  $200\,\mu\text{m}$  also happens to be approximately the center-of-mass of the  $100\text{--}500\,\mu\text{m}$  bin in background simulation. We average the two extrapolated ratios and derive a correction and systematic uncertainty from this average extrapolated ratio.

If the average extrapolated ratio is  $> 1.0$ , we take the central value as a multiplicative correction to the background estimate and the uncertainty in the average as a systematic uncertainty in the background estimate. In this case, we also vary the  $200\,\mu\text{m}$  extrapolation point by  $\pm 50\,\mu\text{m}$ , as we find that the width of the tau lepton contribution as a function of  $|d_0|$  is about  $50\,\mu\text{m}$ . We apply the difference from this variation in extrapolation point as an additional systematic uncertainty in the background estimate. If the average is  $\leq 1.0$ , we set the correction equal to 1.0 and use the uncertainty in the average as a symmetric systematic uncertainty about 1.0. Table 3.8 shows the resulting correction factors along with the uncorrected and corrected SR I background estimate.

### 500 $\mu\text{m}$ –10 cm systematic uncertainty

As shown above, no correction to the background estimate is needed in the  $500\,\mu\text{m}$ –10 cm region, since the tau lepton contribution is negligible here. In this region, we derive a systematic uncertainty in the background estimate from the data closure tests shown in Section 3.4.3. We take the largest deviation from 1 that occurs

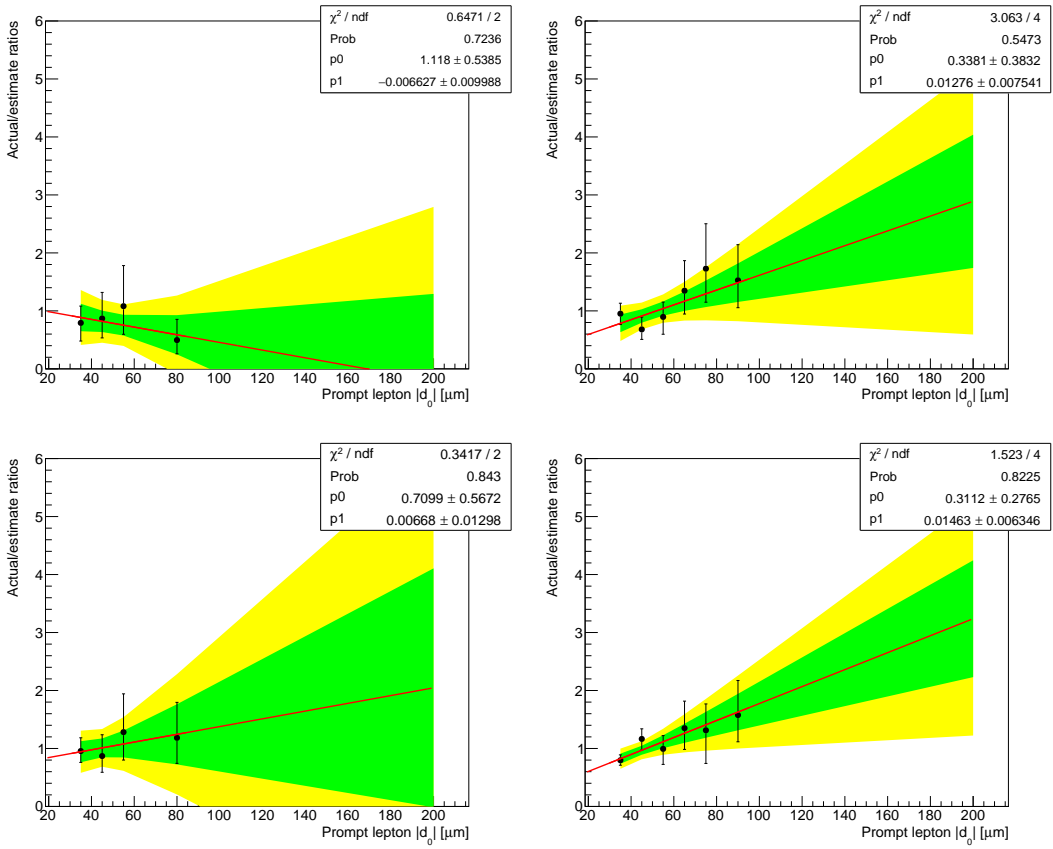


Figure 3.10: Background estimation closure tests in data, in the one-prompt (20–100  $\mu\text{m}$ )/one-displaced (100–500  $\mu\text{m}$ ) sidebands, in the  $e\mu$  channel. The prompt leading electron/ displaced leading muon sideband is shown in the upper row, and the prompt leading muon/ displaced leading electron sideband is shown in the lower row. The plots on the left show the results for 2016 data, and the plots on the right are for combined 2017 and 2018 data. The plots show the ratio of the actual to the estimated number of events as a function of the prompt lepton  $|d_0|$ . The data are fitted with a straight line, where the slope and y-intercept are allowed to vary. The  $1\sigma$  and  $2\sigma$  confidence intervals are shown in the green and yellow bands, respectively.

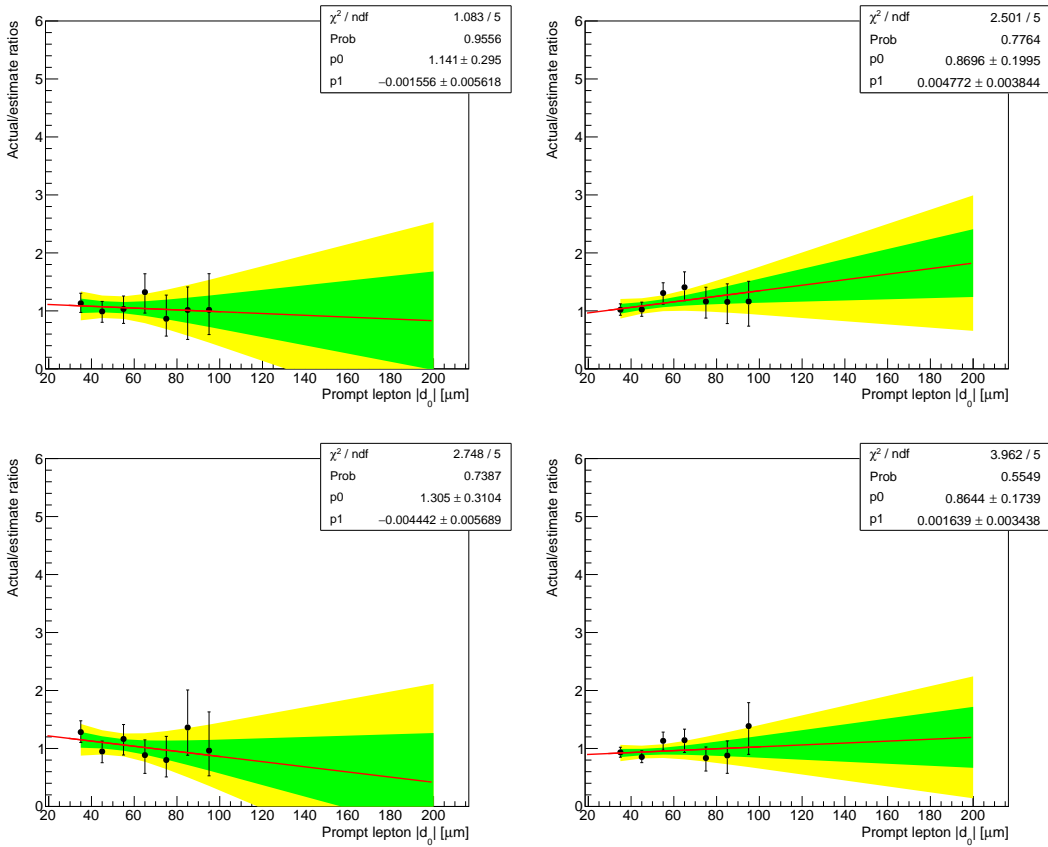


Figure 3.11: Background estimation closure tests in data, in the one-prompt (20–100  $\mu\text{m}$ )/one-displaced (100–500  $\mu\text{m}$ ) sidebands, in the ee channel. The prompt leading electron/ displaced subleading electron sideband is shown in the upper row, and the prompt subleading electron/ displaced leading electron sideband is shown in the lower row. The plots on the left show the results for 2016 data, and the plots on the right are for combined 2017 and 2018 data. The plots show the ratio of the actual to the estimated number of events as a function of the prompt lepton  $|d_0|$ . The data are fitted with a straight line, where the slope and y-intercept are allowed to vary. The  $1\sigma$  and  $2\sigma$  confidence intervals are shown in the green and yellow bands, respectively.

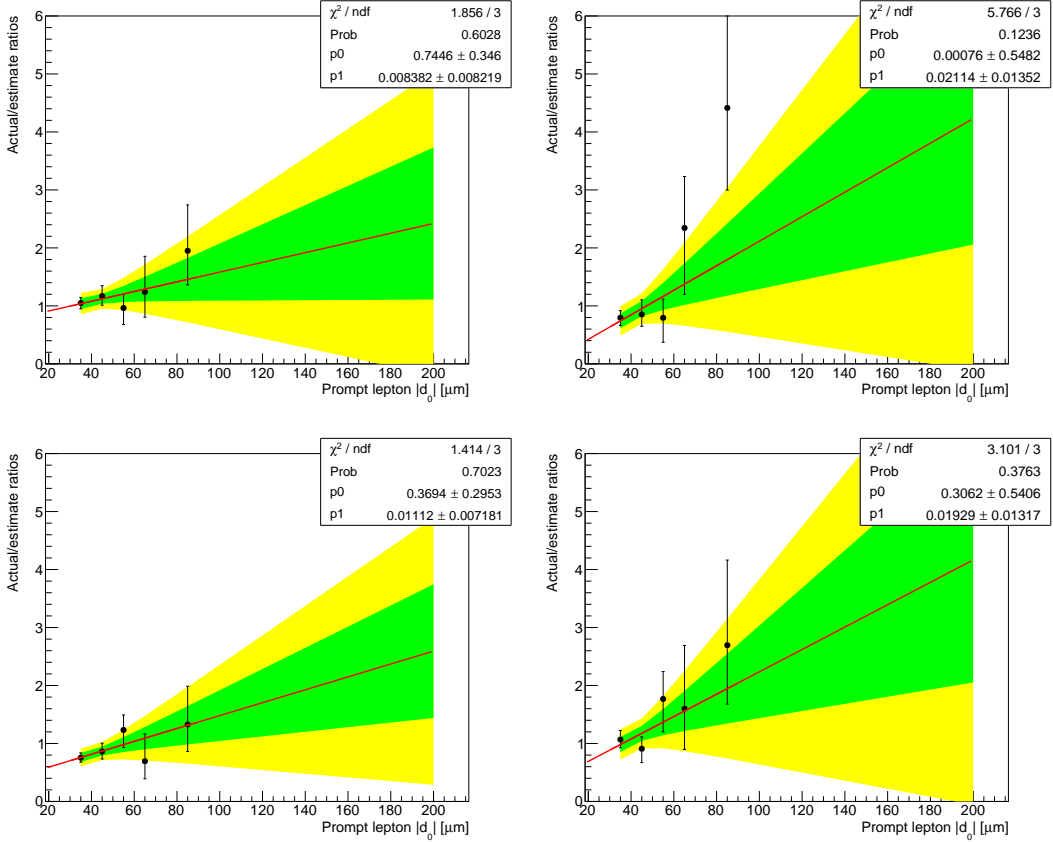


Figure 3.12: Background estimation closure tests in data, in the one-prompt (20–100  $\mu\text{m}$ )/one-displaced (100–500  $\mu\text{m}$ ) sidebands, in the  $\mu\mu$  channel. The prompt leading muon/ displaced subleading muon sideband is shown in the upper row, and the prompt subleading muon/ displaced leading muon sideband is shown in the lower row. The plots on the left show the results for 2016 data, and the plots on the right are for combined 2017 and 2018 data. The plots show the ratio of the actual to the estimated number of events as a function of the prompt lepton  $|d_0|$ . The data are fitted with a straight line, where the slope and y-intercept are allowed to vary. The  $1\sigma$  and  $2\sigma$  confidence intervals are shown in the green and yellow bands, respectively.

in the ratio of the actual to the estimated number of events plus its uncertainty, in either of the two closure tests that correspond to a given SR, as a systematic uncertainty. This is a conservative approach that produces a large systematic uncertainty in the small background yields that we predict in these regions. Table 3.9 shows the systematic uncertainty and the predicted number of events in SRs II, III, and IV.

### 3.4.5 Testing full background estimation procedure

Having defined the full background estimation procedure and seen that the  $|d_0^a|$ - $|d_0^b|$  correlation observed in data is also present in simulated background events, we now perform a final closure test of the full background estimation method using simulated background events in SRs I–IV.

Table 3.10 shows the estimated and actual number of simulated background events in SRs I–IV. The listed estimates include all corrections and statistical and systematic uncertainties as discussed in 3.4.4. The uncertainties in the actual values are purely statistical. The general agreement between estimated and actual yields leads us to conclude that the background estimation procedure is valid and the assigned systematic uncertainties are sufficient to cover any potential sources of nonclosure that we have not explicitly considered.

### 3.4.6 Additional background checks

We perform a few additional studies to check for other potential sources of background. We find that their SR contributions are either negligible or already covered by the background estimation method described above.

## Material interactions

In order to further study the material interactions, we invert the preselection criterion that rejects good vertices in the material. In data, we find seven events, across all channels and years, that pass the preselection with this inverted criterion. As shown in Table 3.11, Three of these events are in the Prompt Control Region, and four are in region B or region C. The lepton vertices in these events coincide with the material as we expect: two are in the beampipe, one is in the BPIX inner shield, and four are in BPIX layer 1. To summarize, even with the material interaction veto inverted, we find no SR events resulting from material interactions and therefore conclude that material interactions are not a significant background after the full selection is applied.

## Cosmic-ray muons

To estimate the SR contribution of cosmic-ray muons, we perform a study in which we invert the  $\Delta t$  and  $\cos \alpha$  criteria in the  $\mu\mu$  preselection and then check how many of these events in data are in the SRs. We find three events in data with these criteria (one event per year, all in SR IV). We find the efficiency to pass the  $\Delta t$  and  $\cos \alpha$  criteria in NoBPTX data, which is predominantly cosmic-ray muon events, on top of the rest of the  $\mu\mu$  preselection criteria. Zero events in NoBPTX data pass all of the preselection criteria, and 3736 events in NoBPTX data pass all of the preselection criteria except these two cosmic rejection selections. To conservatively estimate the efficiency, we fluctuate the 0 events up to 1 and find an efficiency of 1/3736. We therefore find the approximate upper bound on the SR contribution of cosmic ray

muons to be  $3 \times 1/3736 = 0.0008$ , which is negligible compared to the background estimation in each SR.

### Heavy-flavor mesons

To estimate an upper limit on the SR contribution of leptons from heavy-flavor mesons, we perform two studies.

First, we estimate SR yields with a simple ABCD method in 2018  $\mu\mu$  preselection data while additionally requiring at least one medium CSVv2  $b$ -tagged jet. The test is performed in the  $\mu\mu$  channel because it contains the smallest relative SR contribution from mismeasurements and should therefore be most sensitive to heavy flavor. As shown in Table 3.12, the background estimates are about an order of magnitude smaller than when no  $b$  jet is required in our usual preselection.

Next, we look at samples in 2018 data and simulated QCD events that pass the  $\mu\mu$  preselection with the isolation criterion inverted. These samples are dominated by muons from B meson decays, and the QCD simulation describes the data well in the region outside of the 1 boson peak, as can be seen in Fig. 3.13. We use this QCD sample to test the heavy-flavor background in two ways. First, we perform a simple ABCD estimate in the simulated QCD events to check for  $|d_0^a| - |d_0^b|$  correlation. As shown in Table 3.13, we find no evidence of correlation, which indicates that the background estimation already accounts for the heavy-flavor background. Second, we estimate the approximate heavy-flavor background in the SRs by taking the ratio of SR to prompt control region events in QCD simulation from the anti-isolated region and the normalization from the number of simulated QCD events that pass the  $\mu\mu$  preselection. Using this approach, we estimate that the heavy-flavor background to

be  $0.06^{+0.13}_{-0.05}$  events in SR I and  $0.0015^{+0.0034}_{-0.0012}$  events in SR IV, which is small relative to the nominal prediction shown in the first row of Table 3.12.

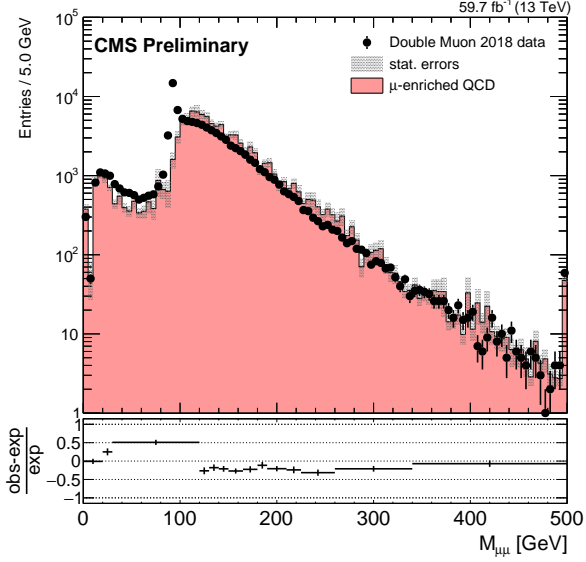


Figure 3.13: The dimuon invariant mass distribution in the  $\mu\mu$  channel with the muon isolation criterion inverted, for 2018 data and QCD simulation.

We therefore conclude that the heavy-flavor SR contribution is small and already accounted for in our background estimates.

### Low-mass SM hadrons

To estimate an upper limit on the SR contribution of leptons from decays of low-mass SM hadrons, we examine 2018 data and QCD simulation in the  $\mu\mu$  channel with both the muon isolation and the  $\Delta R$  requirements inverted. As shown in Fig. 3.14, this region is dominated low-mass  $\mu\mu$  pairs, with clear  $J/\psi$ ,  $\psi'$ , and  $\Upsilon$  mass peaks. Many of these leptons are displaced, especially those in the  $J/\psi$  mass range. To estimate the fraction of such leptons that will be displaced, we take the ratio of SR

to prompt control region events of SM hadrons that decay to leptons from data in this region.

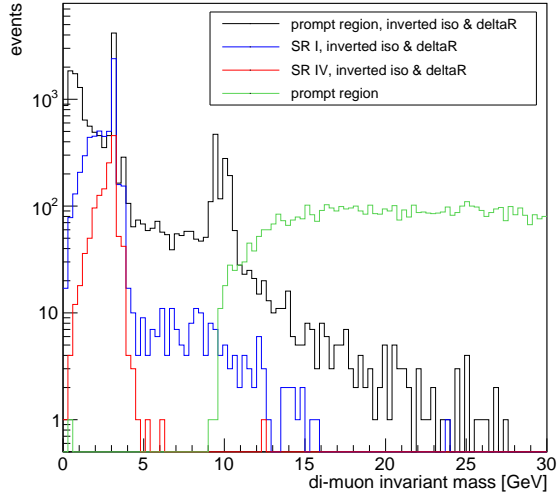


Figure 3.14: The dimuon invariant mass distribution in 2018 data in the  $\mu\mu$  channel, in the prompt control region (black), SR I (blue), SR IV (red), with the muon isolation and  $\Delta R$  criteria inverted. The equivalent distribution from the prompt control region is also shown in green.

Even though the inverted-isolation region is dominated by low-mass muon pairs, the only QCD simulation event that survives the 2018  $\mu\mu$  preselection has a di-muon invariant mass of approximately 300 GeV. Furthermore, the muons are not near each other in the  $\eta-\phi$  plane ( $\Delta R \approx 3$ ), which is inconsistent with the low-mass SM hadron events that dominate the region with the inverted isolation and  $\Delta R$  criteria. To find a normalization from which to estimate the low-mass SM hadron SR contribution, we therefore turn to the inverted-isolation sample used above in the heavy-flavor meson cross check. In this sample, the ratio of events with  $\Delta R < 0.5$  to events

with  $2.8 < \Delta R < 3.2$  is about 0.1. We find 0.2 QCD simulated events that pass the nominal preselection, and so we estimate that of the events passing the 2018  $\mu\mu$  preselection, about 0.02 contain pairs of muons produced in low-mass SM hadron decays. We estimate the SR contributions using this preselection normalization and the ratio of SR to prompt control region events from the sample of SM hadrons that decay to leptons in data. We find this contribution is less than  $0.006^{+0.013}_{-0.005}$  events in SR I and less than  $0.001^{+0.002}_{-0.001}$  events in SR IV, which, if compared with the nominal prediction shown in the first row of Table 3.13, are respectively negligible and covered by the 140% systematic uncertainty already applied in this region.

## 3.5 Corrections to simulation

Several corrections are applied to the simulated background and signal events in order to account for known differences between simulation and data. Each correction is described individually in the following sections.

### 3.5.1 Event pileup

The simulation is corrected so that its distribution of the number of pileup interactions matches that of 2016, 2017, and 2018 data. Each simulated sample is reweighted, event-by-event, by scale factors derived by dividing the pileup distribution in data by the pileup distribution in the given simulated sample.

### 3.5.2 Lepton ID

We apply scale factors provided by the CMS Physics Object Groups to correct for known differences in the lepton reconstruction and tight ID performance between data and simulation. Although our lepton ID differs from the standard tight ID in that we do not set requirements on  $|d_0|$  or  $|d_z|$ , the standard scale factors are still sufficient for our case because the leptons from Z decays from which they are derived are representative of leptons in the bulk of the  $|d_0|$  distribution and we apply additional systematic uncertainties to account for possible differences at larger  $|d_0|$  (see Section 3.6).

### 3.5.3 Lepton $d_0$ resolution

As shown in Fig. 3.15, the agreement between data and simulation in the 2017 and 2018 electron and muon  $|d_0|$  distributions was initially poor. We found that the average muon and electron  $d_0$  fluctuated periodically with respect to  $\phi$  in 2017

and 2018 data but not in background simulation, as can be seen in Fig. 3.16. This periodic fluctuation in data but not in simulation indicates that the tracker alignment is overly optimistic in simulation, which produces an unrealistically narrow simulated  $d_0$  distribution.

To account for the overly optimistic alignment in simulation, we smear the electron and muon  $d_0$  in 2017 and 2018 background MC simulation in each channel’s prompt control region to match that of data. To do this, we first fit the central regions of the background simulation and data  $d_0$  distributions with Gaussian functions in each channel’s prompt control region and then compare the widths of the Gaussian fits. The fitted distributions are shown in Figs. 3.17 and 3.18 for the  $e\mu$  channel. Assuming that the width of each Gaussian fit is mostly determined by the  $d_0$  resolution, we define  $\sigma_{data}^2 = \sigma_{bgd}^2 + \sigma_{align}^2$ , where  $\sigma_{data}$  is the data Gaussian width,  $\sigma_{bgd}$  is the uncorrected background simulation Gaussian width, and  $\sigma_{align}$  is the additional component that is needed to make up the difference in  $d_0$  resolution between background simulation and data. We find  $\sigma_{data}$  and  $\sigma_{bgd}$  from the fits and compute  $\sigma_{align}$ . The fit results are similar in the  $e\mu$  channel shown here and in the same-flavor channels. We average the  $\sigma_{align}$  derived in the  $ee$  channel and the  $e\mu$  channel for electrons, and in the  $\mu\mu$  channel and the  $e\mu$  channel for muons. The average  $\sigma_{align}$  is shown in Table 3.14. We then smear the simulation  $d_0$  values with values drawn from a Gaussian distribution centered at 0 and with a width of the average  $\sigma_{align}$ . The smearing is applied to both background and signal MC simulation. The corrected  $|d_0|$  distributions are shown in Section 3.3.3.

This  $d_0$  smearing has a minimal effect on the final result because the width of the Gaussian distribution from which the smearing values are drawn is small relative to

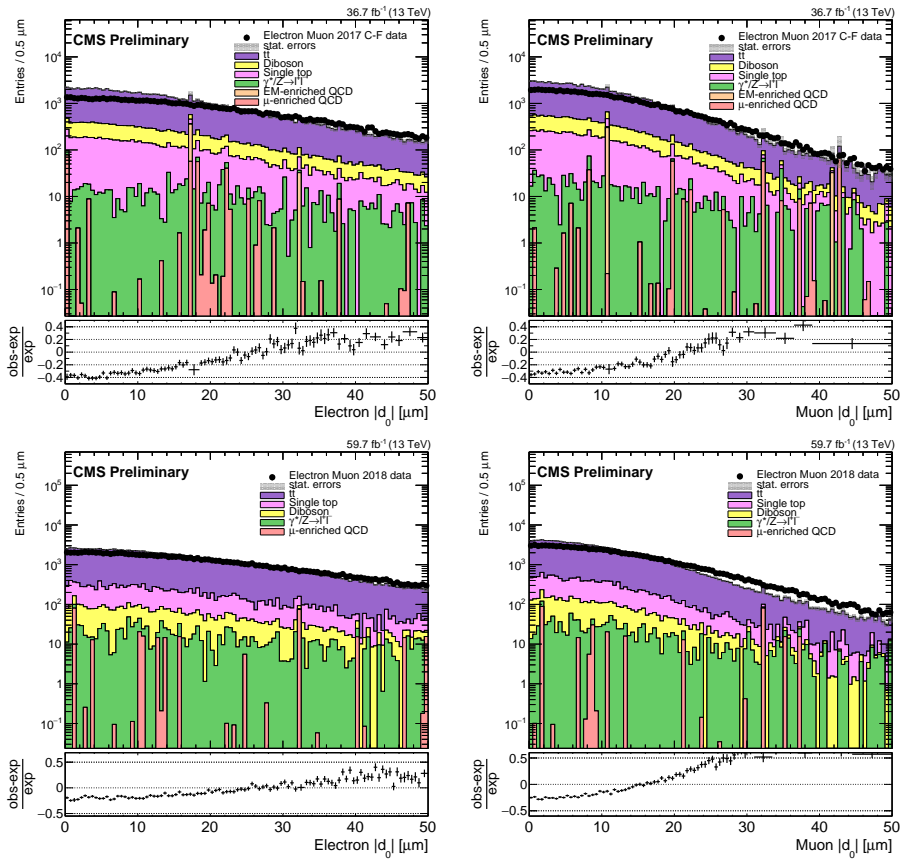


Figure 3.15: The uncorrected lepton  $|d_0|$  distributions in the  $e\mu$  prompt control region, for electrons (left) and muons (right), for 2017 data and simulation (upper), and 2018 data and simulation (lower). The rightmost bin in each plot contains the overflow entries.

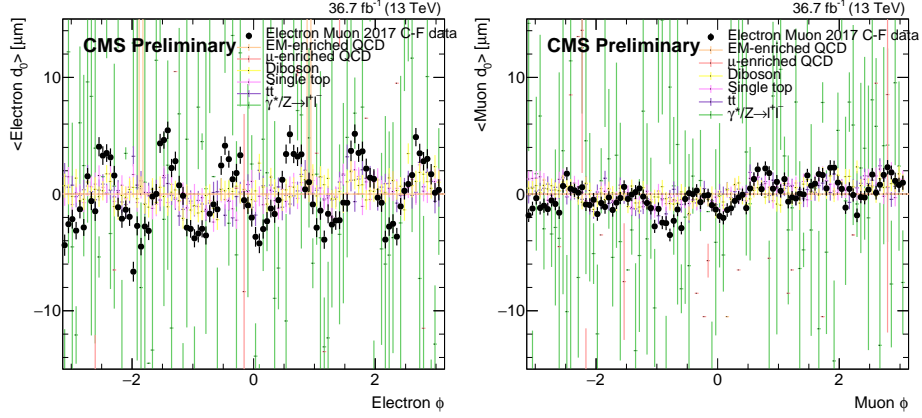


Figure 3.16: The average lepton  $|d_0|$  as a function of  $\phi$  in the  $e\mu$  prompt control region, for electrons (left) and muons (right), for 2017 data and simulation.

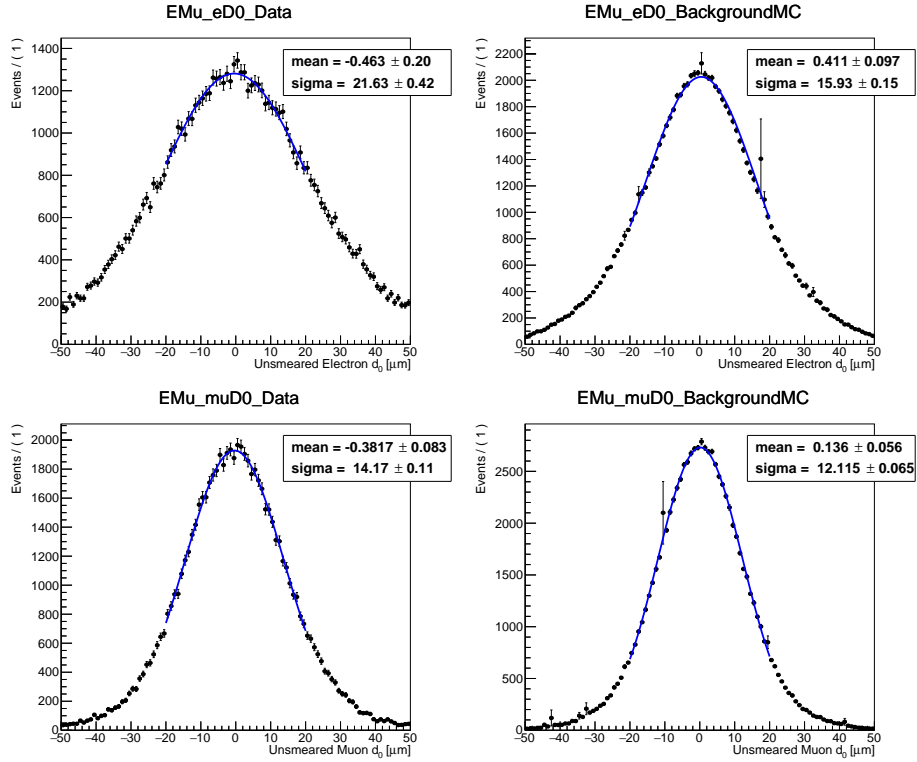


Figure 3.17: The lepton  $d_0$  distributions with Gaussian fits in data (left) and background simulation (right) for electrons (upper) and muons (lower) in the 2017  $e\mu$  prompt control region. The widths of the Gaussian fits are used to determine the width of the Gaussian distribution used to smear the  $d_0$ .

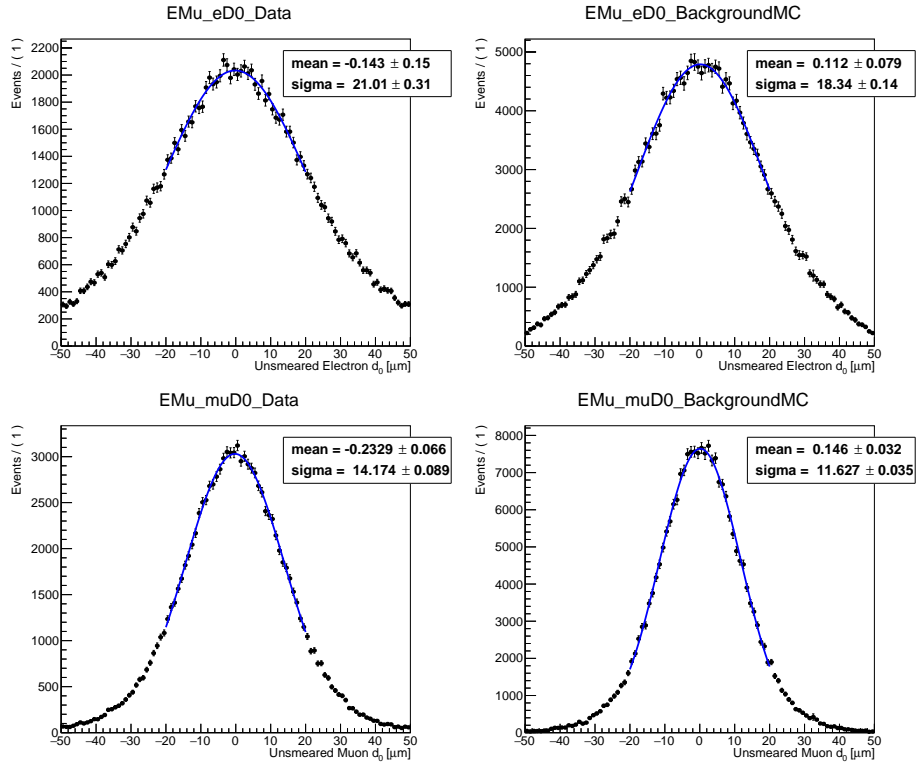


Figure 3.18: The lepton  $d_0$  distributions with Gaussian fits in data (left) and background (right) for electrons (upper) and muons (lower) in the 2018  $e\mu$  prompt control region. The widths of the Gaussian fits are used to determine the width of the Gaussian distribution used to smear the  $d_0$ .

the size of the signal region bins, but understanding the source of the poor agreement between data and simulation was important to validate our understanding of the SM background.

### 3.5.4 Trigger efficiency

We also apply scale factors to the simulated background and signal events to correct for differences in trigger efficiency between data and simulation. To measure the trigger efficiency, we first require that events pass an OR of several unprescaled MET triggers (see Table 3.15) and the preselection criteria with the lepton  $p_T$  requirement excluded. The MET triggers provide a sample of dilepton events that is unbiased with respect to the main triggers used in the analysis, and excluding the lepton  $p_T$  requirement allows us to study the trigger efficiency as a function of lepton  $p_T$ . In the  $e\mu$  channel, the electron (muon)  $p_T$  is required to be greater than 50 GeV when plotting against the muon (electron)  $p_T$  to disentangle the effect from the other leg of the muon-photon trigger. Data events are taken from the MET primary dataset and simulated background events are taken from  $t\bar{t}$  simulation for the  $e\mu$  channel and DY simulation for the same-flavor channels. When calculating the efficiency, the numerator is the lepton  $p_T$  distribution in events that pass the main triggers in addition to the OR of MET triggers and the preselection, and the denominator is the lepton  $p_T$  distribution in events that pass the OR of MET triggers and the preselection. The scale factor is the ratio of the efficiency in data to the efficiency in simulation in the plateau of the efficiency distribution.

## 3.6 Systematic uncertainties

### 3.6.1 Integrated luminosity

The integrated luminosities of the 2016, 2017, and 2018 data-taking periods are individually known with uncertainties in the 2.3–2.5% range [21, 22, 23], while the total Run 2 (2016–2018) integrated luminosity has an uncertainty of 1.8%, the improvement in precision reflecting the uncorrelated time evolution of some systematic effects. The full table of 2016–2018 integrated luminosity uncertainties are taken from [39], with the correlations specified therein.

### 3.6.2 Pileup

The simulation of pileup events assumes a total inelastic pp cross section of 69.2 mb with an associated uncertainty of 5% [46]. The systematic uncertainty arising as a result of the modeling of pileup events is estimated by varying the cross section of the minimum bias events by 5% when generating the target pileup distributions. The pileup weights are recomputed with these new distributions and applied to the simulated events to obtain the variation in the yields in the inclusive signal region. The average uncertainty is between 1 and 2%. We treat these uncertainties as 100% correlated across the three years of data taking.

### 3.6.3 Trigger efficiency

The trigger efficiency systematic uncertainty is given by the uncertainty in the measured trigger efficiency scale factors (see Section 3.5.4). These uncertainties are 1% or less for the  $e\mu$  and  $\mu\mu$  channels and about 10% for the ee channel.

In addition, we have studied the trigger efficiency in signal as a function of  $|d_0|$ , as shown in Fig. 3.19, for events in the trigger  $p_T$  plateau. To cover the change observed in the muon trigger efficiency over the full  $|d_0|$  range, we assign an additional 20% uncertainty.

We treat the trigger efficiency uncertainties as 100% correlated across the three years of data taking.

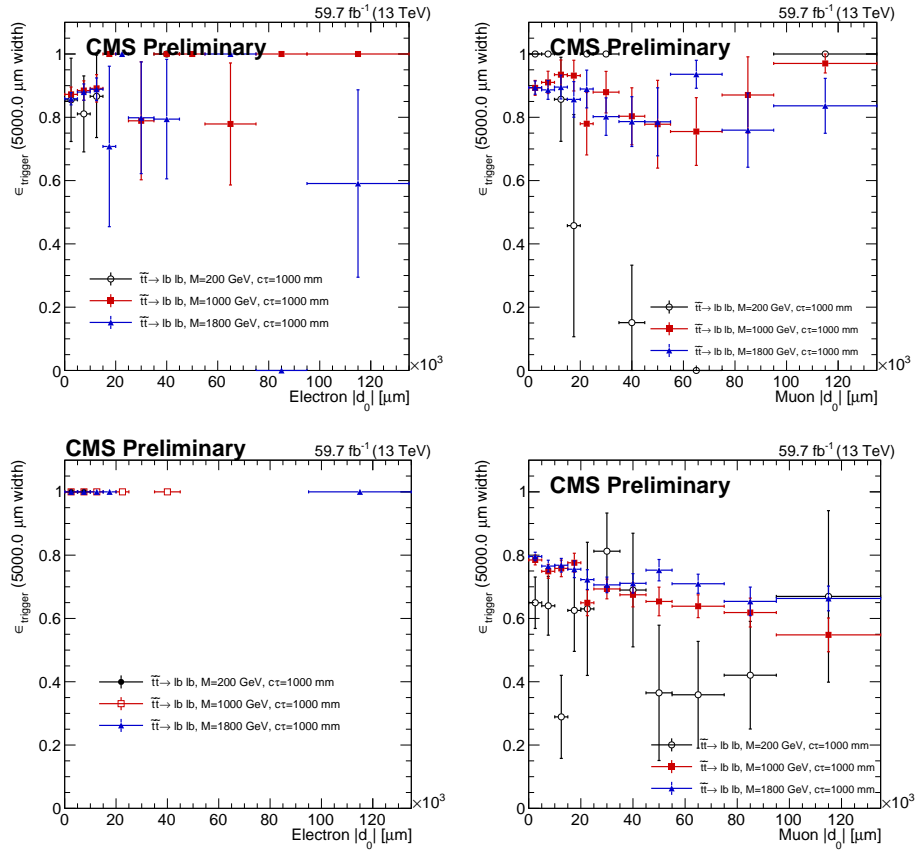


Figure 3.19: Trigger efficiency as a function of lepton  $|d_0|$ , for the  $e\mu$  channel (upper row), the  $ee$  channel (lower left), and the  $\mu\mu$  channel (lower right) in 2018 signal, for events in the trigger  $p_T$  plateau.

### 3.6.4 Lepton ID and isolation

To find the systematic uncertainty associated with the corrections to the lepton ID and isolation, we fluctuate the lepton scale factors up and down by their uncertainty and observe the change in the event yields in the inclusive signal region. The average uncertainty for electrons is about 3% in the  $e\mu$  channel and about 7% in the ee channel, while the average uncertainty for muons is  $< 1\%$ . We treat these uncertainties as 100% correlated across the three years of data taking.

### 3.6.5 Muon pixel hit efficiency

The requirement in the muon ID that muons have at least one pixel hit could in principle have some appreciable  $|d_0|$  dependence, so we perform a dedicated study to ensure that we account for any differences in  $|d_0|$  dependence between data and simulation. Figure 3.20 shows the efficiency of this requirement in cosmic simulation and NoBPTX data as a function of muon  $|d_0|$ . For events in the denominator of these plots, we require that at least 2 global, PF muons have  $|\eta| < 1.0$ ,  $p_T > 25 \text{ GeV}$ , no displaced vertices in the tracker material,  $|z_0| < 15$ , and that they pass all the tight ID criteria except the pixel hit requirement. We also require the muons to be separated by  $\Delta R > 0.2$ . The events in the numerator must pass the same requirements in addition to the requirement that the muons have at least one pixel hit. Using this plot, the mean efficiency to identify the muons in the simulated signal events is evaluated in the same way as done for the displaced tracking efficiency systematic uncertainty. That is, we find the efficiency to identify muons that pass the pixel hit requirement in cosmic simulation and in NoBPTX data, and using the ratio of these two efficiencies, we derive the relative systematic uncertainty in the signal. The average uncertainty

is about 16% (32%) in the  $e\mu$  ( $\mu\mu$ ) channel. As the pixel detector was upgraded after 2016, the 2017 and 2018 systematic uncertainties are treated as fully correlated, while the 2016 uncertainty is treated as uncorrelated with the 2017 and 2018 uncertainties.

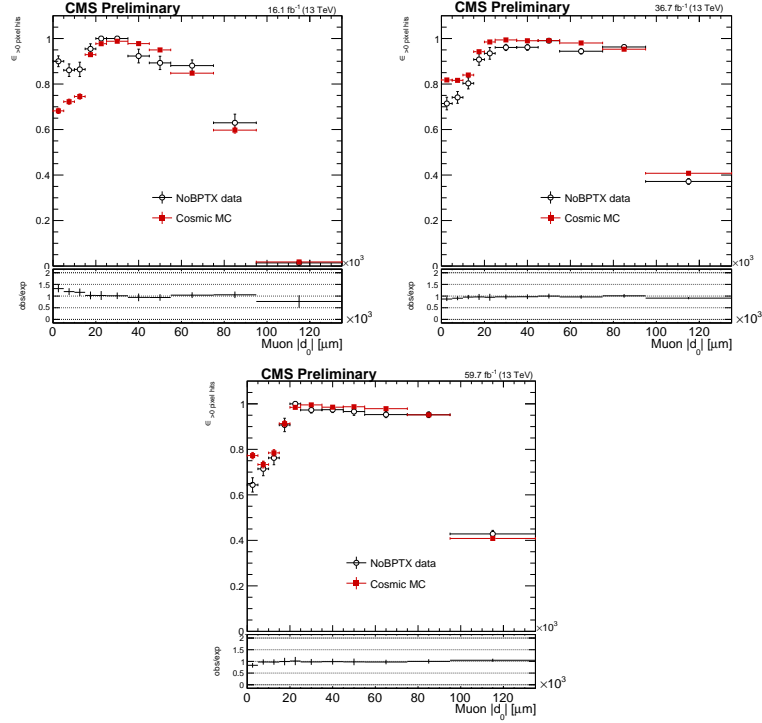


Figure 3.20: The pixel hit efficiency as a function of muon  $|d_0|$ , for cosmic simulation and NoBPTX data in 2016 (left), 2017 (middle), and 2018 (right) conditions.

### 3.6.6 Lepton $d_0$ resolution

To find the systematic uncertainty associated with the corrections to the lepton  $d_0$  (see Section 3.5.3), we fluctuate the lepton  $d_0$  corrections up and down by their uncertainty and observe the change in the event yields in the inclusive signal region. The average uncertainty is  $< 1\%$ . We treat these uncertainties as 100% correlated

in 2017 and 2018. No  $d_0$  correction or systematic uncertainty is needed for 2016 simulation.

### 3.6.7 Summary of systematic uncertainties in the signal efficiency

The systematic uncertainties in the signal efficiency are summarized in Table 3.16.

### 3.7 Results

Table 3.17 shows the expected number of background events and the observed data in each SR and  $p_T$  bin, for each channel. We split SR I into two bins. In the  $e\mu$  and  $\mu\mu$  channels, these bins are in the leading muon  $p_T$ , and in the ee channel, these bins are in the leading electron  $p_T$ . The  $p_T$  bins are chosen such that the high- $p_T$  bin contains  $<1$  background event, which increases the sensitivity to small lifetimes and large masses. The observed number of events are consistent with the predicted amount of background.

Figure 3.21 shows two-dimensional  $|d_0|$  distributions of data events that pass the preselection, and Fig. 3.22 shows the same but for data events in the inclusive SR. Figure 3.23 shows the the same along with a representative signal point.

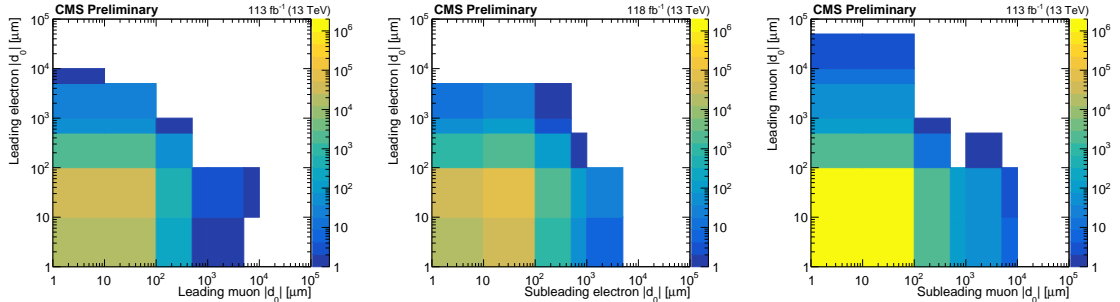


Figure 3.21: Two-dimensional distributions of  $|d_0^a|$  and  $|d_0^b|$ , for the events in data that pass the  $e\mu$  (left), ee (middle), and  $\mu\mu$  (right) preselection. If a  $|d_0|$  value is less than unity, it is set to unity in order to plot in log scale. The inclusive signal region covers the region between  $100 \mu\text{m}$  and  $10 \text{ cm}$  in each  $|d_0|$  variable shown.

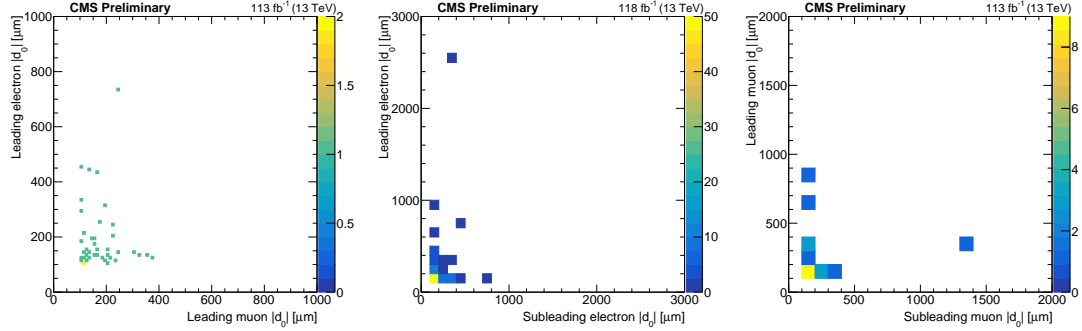


Figure 3.22: Two-dimensional distributions of  $|d_0^a|$  and  $|d_0^b|$ , for data events in the inclusive SR in the  $e\mu$  (left),  $ee$  (middle), and  $\mu\mu$  (right) channels.

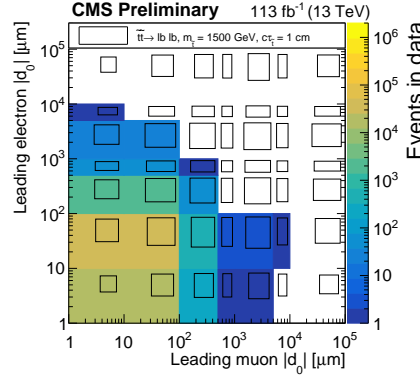


Figure 3.23: The two-dimensional distribution of the leading electron and leading muon  $|d_0|$ , for the events in data (colors) and signal (black boxes) that pass the  $e\mu$  preselection. The size of the black boxes are proportional to the size of the bin content. If a  $|d_0|$  value is less than unity, it is set to unity in order to plot in log scale. The inclusive signal region covers the region between  $100 \mu\text{m}$  and  $10 \text{ cm}$  in each  $|d_0|$  variable shown.

### 3.7.1 Observed events

This section provides a summary of observations recorded while examining event displays of the signal region events.

In general, the SR events appear to be SM events from the pp collision. Specifically, we see no evidence of leptons from cosmic rays, material interactions, or signal.

In the  $e\mu$  channel, the SR events tend to have several jets and often have significant MET. Many events have muon  $\phi$  values such that the muon system hits are all near the edges of detector sections or muon  $\eta$  values such that the muon is near the barrel/endcap transition in the muon system. There are also a few events in which the electron and/or muon are associated with different primary vertex than their associated track.

In the ee channel, the majority of SR events contain at least one electron with  $|eta| > 1.1$ , where increases the probability that their  $d_0$  is poorly measured. Across all three years, most events fall into one of three categories:

1. Events with two electrons that appear to be from a boosted 1 boson, with an invariant mass between 80 and 100 GeV, opposite one or two jets
2. Events with two electrons approximately back-to-back in  $\phi$  with an invariant mass greater than 100 GeV and MET usually between 10 and 40 GeV
3. Events that are similar to type 2 but with at least one jet and frequently MET between 70 and 110 GeV

In the  $\mu\mu$  channel, many events have an invariant mass consistent with the mass of the 1 boson and MET less than about 60 GeV. Most of the events found in 2017 and 2018 have an invariant mass higher than than the 1 boson mass and could be  $t\bar{t}$

events. Eight of the sixteen SR events in 2016 have two muons with  $\phi$  values of about  $\pm\pi/2$ . All of the muon pairs in these eight events have an invariant mass consistent with a 1 boson. Furthermore, the  $\cos(\alpha)$  and timing distributions of these muons imply that they are not from cosmic rays. Thirteen of the sixteen muons in these eight events have only one valid pixel hit, and event displays of these events show that the muon track often passes between or at the edge of pixel modules near the place where the two halves of the pixel detector barrel are joined. We believe that this feature causes the muon  $d_0$  values to be poorly measured.

### 3.7.2 Limits

The data show no significant excess over background, so we set upper limits on the product of the signal production cross section ( $\sigma$ ) and branching fraction ( $\mathcal{B}$ ) using the “Combine” tool developed by the CMS Higgs working group with HybridNew limits [37, 43, 25, 53]. The ABCD estimate is performed in Combine, which has the advantage that any signal contamination in the control regions is automatically accounted for. We perform a simultaneous counting experiment in each signal region bin. Figure 3.24 shows the 95% confidence level (C.L.) upper limits on the top squark mass as a function of its lifetime.

The variation in the size and shape of the exclusion regions between the three channels is mostly explained by variation in signal yields between the three channels. Looking at the high- $p_T$  bin of SR I, which is the most sensitive bin for top squarks with large masses and small lifetimes, we find that the simulated signal yield is highest in the  $e\mu$ . This difference between the  $e\mu$  and same-flavor channels is a result of simple combinatorics: the two independent top squark decays will result in an  $e\mu$  final state

twice as often as an ee or  $\mu\mu$  final state. In this bin, the ee and  $\mu\mu$  channel signal yields are similar. In SR IV, which drives the sensitivity for top squarks with large lifetimes, the  $\mu\mu$  channel has the largest simulated signal yield when considering top squarks with lifetimes  $\gtrsim 10$  cm. This difference is due to the better muon reconstruction than electron reconstruction of CMS. For this same reason, the ee channel has the smallest signal yield out of the three channels in SR IV when considering top squark lifetimes  $\gtrsim 10$  cm. Taking all of these effects together, we find that the  $e\mu$  channel is the most sensitive for lifetimes  $\lesssim 10$  cm while the  $\mu\mu$  channel is the most sensitive for lifetimes  $\gtrsim 10$  cm

Figure 3.25 shows the 95% C.L. upper limits for the combination of the three channels. The top squark limits assume  $\mathcal{B}(\tilde{t} \rightarrow bl) = \mathcal{B}(\tilde{t} \rightarrow dl) = 100\%$ , and each  $l$  has an equal probability of being an electron, a muon, or a tau lepton.

### 3.7.3 Additional likelihood tests

We also perform several statistical tests to help assess the significance of the differences between the observed and predicted SR yields and to ensure that the likelihood is handling the observed yields in a reasonable way.

We first compare the best-fit background yields under the background-only hypothesis while masking the signal regions with the best-fit background yields under the signal+background hypothesis using the full information from all signal and control regions. For simplicity, we refer to the first quantity as the pre-fit prediction and the second as the post-fit prediction. Table 3.18 lists the pre- and post-fit predictions for each channel and SR, and Fig. 3.26 shows associated pull distribution. We find

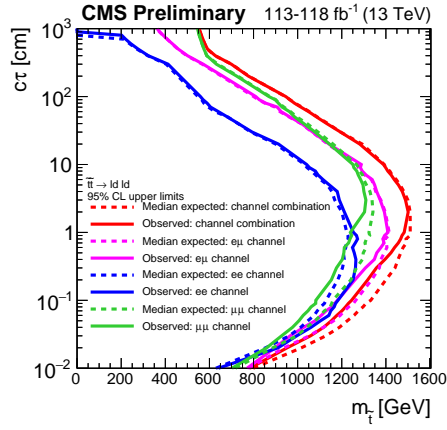
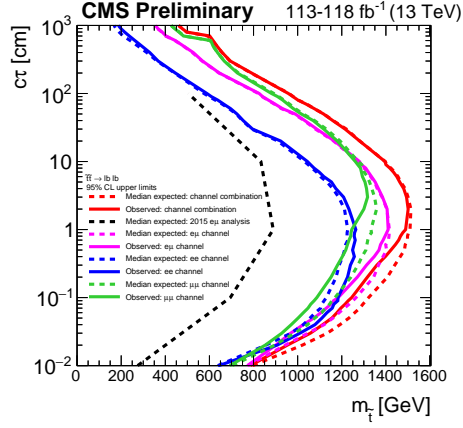


Figure 3.24: The 95% C.L. upper limits on the long-lived particle mass ( $m_{\tilde{t}}$ ) as a function of its lifetime ( $c\tau$ ), for the  $e\mu$ ,  $ee$ , and  $\mu\mu$  channels. The  $\tilde{t}\bar{t} \rightarrow \bar{l}b \bar{l}b$  (left) and  $\tilde{t}\bar{t} \rightarrow \bar{l}1 \bar{l}1$  (right) processes are shown.

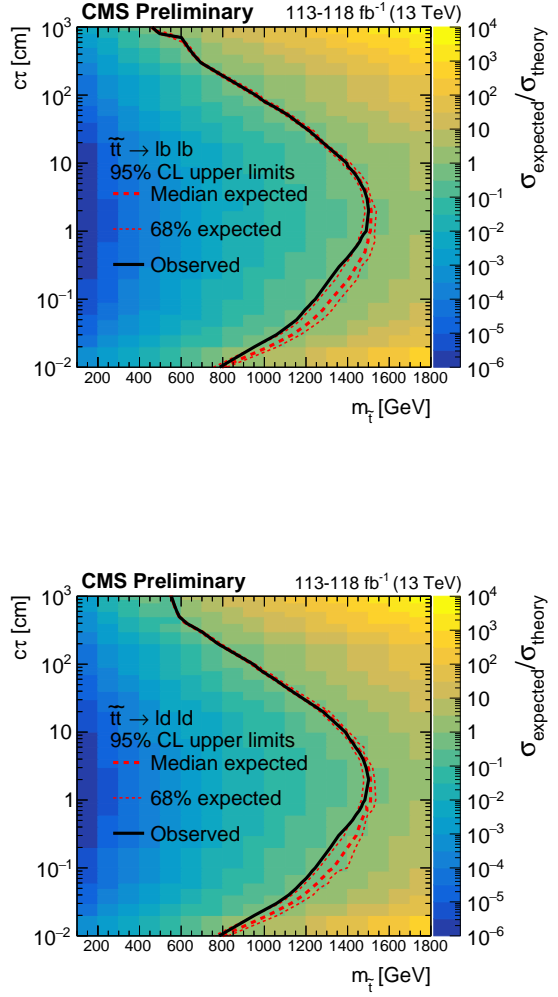


Figure 3.25: The 95% C.L. upper limits on the long-lived particle mass ( $m_{\tilde{t}}$ ) as a function of its lifetime ( $c\tau$ ). The colors indicate the expected cross section divided by the theoretical cross section ( $\sigma_{\text{expected}}/\sigma_{\text{theory}}$ ). The  $\tilde{t}\tilde{t} \rightarrow \bar{l}b\bar{l}b$  (left) and  $\tilde{t}\tilde{t} \rightarrow \bar{l}_1\bar{l}_1$  (right) processes are shown.

that the differences between the pre- and post-fit predictions are consistent with the variation one would expect from purely statistical effects.

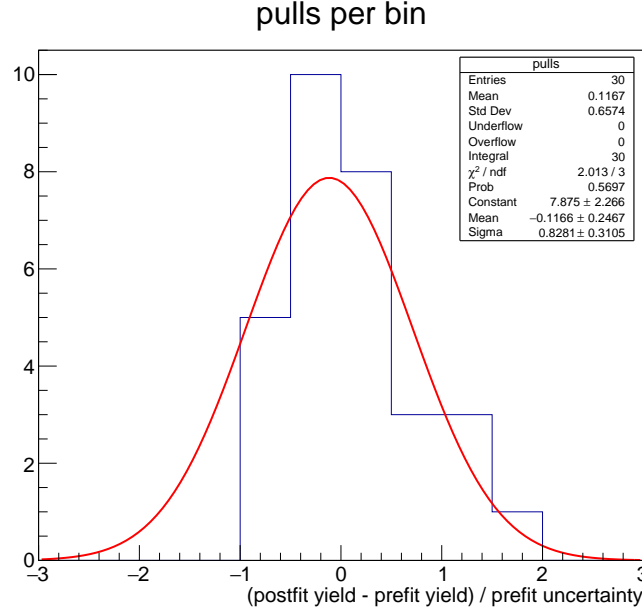


Figure 3.26: The distribution of pulls for each signal region bin. Pulls are calculated as the difference between the post-fit background yield and the pre-fit background yield divided by the pre-fit background uncertainty.

Next, we examine the equivalent pull distribution for background yield nuisance parameters. Figure 3.27 shows that the differences in nuisance parameter values before and after the fit are also consistent with the variation one would expect from purely statistical effects.

Finally, we check the observed asymptotic significance of the  $\tilde{t}\tilde{t} \rightarrow \bar{l}b l\bar{b}$  signal model. As shown in Fig. 3.28, the observed significance is less than two for all signal points we consider. We therefore conclude that the observed yields do not constitute a significant excess.

### Post-fit nuisance pull distribution

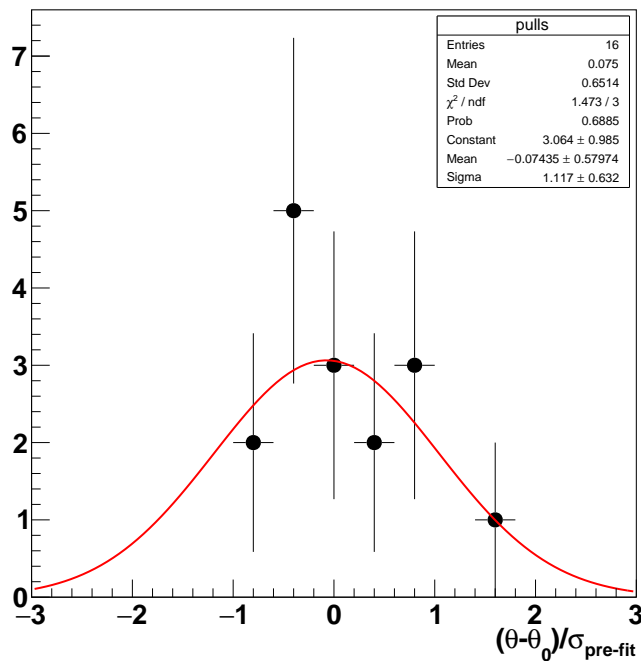


Figure 3.27: The distribution of pulls for each background nuisance parameter. Pulls are calculated as the difference between the post-fit value and the pre-fit value divided by the pre-fit uncertainty.

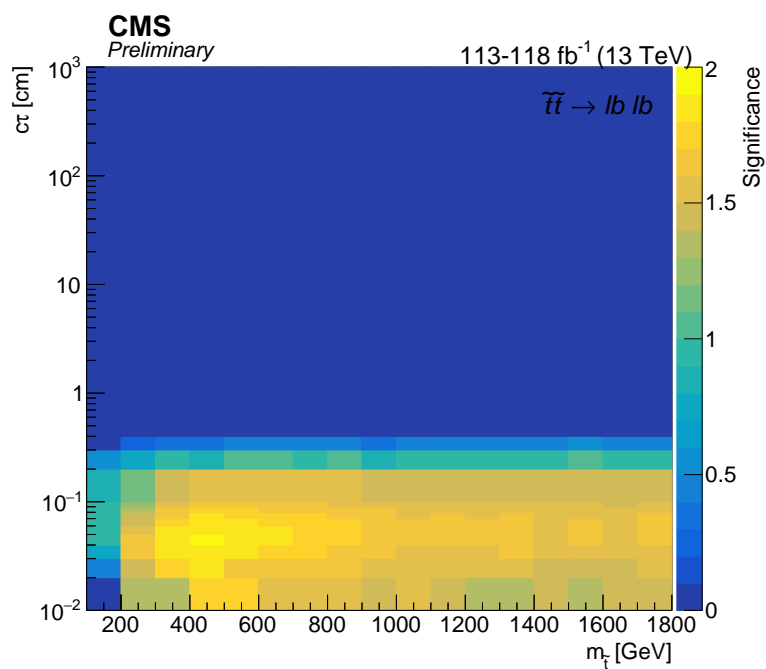


Figure 3.28: The observed asymptotic significances for the  $\tilde{t}\bar{t} \rightarrow \bar{l}b l\bar{b}$  process as a function of  $\tilde{t}$  mass and lifetime.

Table 3.7: Closure test results in data and background simulation (with and without  $Z \rightarrow \tau\tau \rightarrow ll$  events), in the  $500 \mu\text{m} - 10 \text{ cm}$  region. The ratios of the actual yield to the estimated yield and their statistical uncertainties are given. The A, B, C, and D regions are defined as follows: A is  $20 - 30 \mu\text{m}$  in prompt lepton  $|d_0|$  and  $20 - 100 \mu\text{m}$  in displaced lepton  $|d_0|$ , B is  $20 - 30 \mu\text{m}$  in prompt lepton  $|d_0|$  and  $500 \mu\text{m} - 10 \text{ cm}$  in displaced lepton  $|d_0|$ , C is  $30 - 100 \mu\text{m}$  in prompt lepton  $|d_0|$  and  $20 - 100 \mu\text{m}$  in displaced lepton  $|d_0|$ , and D (the test region) is  $30 - 100 \mu\text{m}$  in prompt lepton  $|d_0|$  and  $500 \mu\text{m} - 10 \text{ cm}$  in displaced lepton  $|d_0|$ .

Region B			
	Bkg. simulation w/o $Z \rightarrow \tau\tau \rightarrow ll$	Bkg. simulation	Data
2016 $e\mu$	$1.1 \pm 0.3$	$1.1 \pm 0.3$	$0.4^{+1.0}_{-0.4}$
2017+2018 $e\mu$	$0.9^{+0.3}_{-0.2}$	$0.9^{+0.3}_{-0.2}$	$0.7 \pm 0.3$
2016 ee	$0.4^{+0.6}_{-0.3}$	$0.4^{+0.6}_{-0.3}$	$1.4^{+1.6}_{-0.9}$
2017+2018 ee	$0.5^{+0.8}_{-0.4}$	$0.3^{+0.4}_{-0.2}$	$1.0 \pm 0.3$
2016 $\mu\mu$	$0.7 \pm 0.3$	$0.7 \pm 0.3$	$0.8 \pm 0.3$
2017+2018 $\mu\mu$	$0.8^{+1.8}_{-0.7}$	$0.4^{+1.0}_{-0.4}$	$1.8^{+0.6}_{-0.7}$

Region C			
	Bkg. simulation w/o $Z \rightarrow \tau\tau \rightarrow ll$	Bkg. simulation	Data
2016 $e\mu$	$0.8^{+0.4}_{-0.3}$	$0.8^{+0.4}_{-0.3}$	$1.0$ (0 vs 0)
2017+2018 $e\mu$	$0.8^{+0.3}_{-0.2}$	$0.8^{+0.3}_{-0.2}$	$0.7^{+1.3}_{-0.7}$
2016 ee	$4.0^{+5.8}_{-3.1}$	$4.0^{+5.8}_{-3.1}$	$0.7^{+1.0}_{-0.6}$
2017+2018 ee	$3.5^{+2.6}_{-1.8}$	$2.1^{+2.6}_{-1.5}$	$1.0 \pm 0.3$
2016 $\mu\mu$	$1.2^{+0.5}_{-0.4}$	$1.3^{+0.6}_{-0.4}$	$0.6^{+0.4}_{-0.3}$
2017+2018 $\mu\mu$	$0.4^{+0.4}_{-0.3}$	$0.5^{+0.5}_{-0.3}$	$0.5^{+0.3}_{-0.2}$

Table 3.8: The correction factors and the uncorrected and corrected background estimates in SR I . The correction factor uncertainty includes both the uncertainty in the average and the additional uncertainty obtained from varying the fit extrapolation point. The total uncertainty (statistical plus systematic) is given for the corrected background estimate.

	Correction factor	Uncorrected estimate	Corrected estimate
2016 $e\mu$	$1.0^{+1.3}_{-1.0}$	$4.21^{+0.38}_{-0.40}$	$4.2^{+5.4}_{-4.2}$
2017+2018 $e\mu$	$3.0 \pm 1.0$	$12.53^{+0.64}_{-0.61}$	$38 \pm 13$
2016 ee	$1.00 \pm 0.60$	$18.30^{+0.94}_{-0.91}$	$18 \pm 11$
2017+2018 ee	$1.51^{+0.43}_{-0.42}$	$41.6 \pm 1.3$	$63^{+18}_{-17}$
2016 $\mu\mu$	$2.5 \pm 1.0$	$3.07 \pm 0.08$	$7.7 \pm 3.1$
2017+2018 $\mu\mu$	$4.2 \pm 1.8$	$1.00 \pm 0.04$	$4.2 \pm 1.8$

Table 3.9: The systematic uncertainty and the background estimates in SRs II, III, and IV. The total uncertainty (statistical plus systematic) is given for each estimate.

	Systematic uncertainty	SR II	SR III	SR IV
2016 $e\mu$	98%	$0.15 \pm 0.15$	$0.09^{+0.12}_{-0.09}$	$0.003^{+0.004}_{-0.003}$
2017+2018 $e\mu$	106%	$0.71^{+0.76}_{-0.71}$	$0.23^{+0.27}_{-0.23}$	$0.01^{+0.02}_{-0.01}$
2016 ee	199%	$0.51^{+1.02}_{-0.51}$	$0.43^{+0.85}_{-0.43}$	$0.01^{+0.02}_{-0.01}$
2017+2018 ee	37%	$3.6 \pm 1.4$	$2.8 \pm 1.1$	$0.24^{+0.10}_{-0.09}$
2016 $\mu\mu$	64%	$0.17 \pm 0.11$	$0.19 \pm 0.12$	$0.01 \pm 0.01$
2017+2018 $\mu\mu$	140%	$0.14^{+0.19}_{-0.14}$	$0.08^{+0.12}_{-0.08}$	$0.01^{+0.02}_{-0.01}$

Table 3.10: Closure test results in background simulation in the SRs, with the correction applied. The estimated number of events, the actual number of events, and their total uncertainties (statistical plus systematic) are given. For cases where an uncertainty is not listed, it is negligibly small ( $<0.005$ ).

	SR I	SR II	SR III	SR IV
2016 $e\mu$ estimated	$7.4^{+4.5}_{-3.8}$	$0.07 \pm 0.01$	$0.10^{+0.05}_{-0.03}$	0.001
2016 $e\mu$ actual	$5.0^{+1.5}_{-1.2}$	$0.07^{+0.09}_{-0.05}$	$0.00^{+0.01}_{-0.00}$	0
2017+2018 $e\mu$ estimated	$13.5 \pm 5.7$	$0.37^{+0.08}_{-0.07}$	$0.34 \pm 0.04$	0.01
2017+2018 $e\mu$ actual	$19.1^{+11.4}_{-7.6}$	$0.52^{+0.41}_{-0.25}$	0	0
2016 $ee$ estimated	$9.3 \pm 5.0$	$0.11^{+0.04}_{-0.03}$	$0.14^{+0.05}_{-0.04}$	0.002
2016 $ee$ actual	$13.4^{+3.4}_{-2.8}$	$0.15^{+0.19}_{-0.09}$	$1.03^{+1.36}_{-0.67}$	0
2017+2018 $ee$ estimated	$18 \pm 11$	$0.59^{+0.16}_{-0.13}$	$0.45^{+0.13}_{-0.11}$	$0.02 \pm 0.01$
2017+2018 $ee$ actual	$8.2^{+6.5}_{-3.9}$	$0.17^{+0.23}_{-0.11}$	0	0
2016 $\mu\mu$ estimated	$1.33 \pm 0.53$	0.04	0.03	0.002
2016 $\mu\mu$ actual	$3.3^{+1.8}_{-1.2}$	$0.11^{+0.14}_{-0.07}$	$0.06^{+0.14}_{-0.05}$	0
2017+2018 $\mu\mu$ estimated	$2.7^{+1.3}_{-1.2}$	$0.04 \pm 0.01$	0.02	0.002
2017+2018 $\mu\mu$ actual	$7.1^{+6.9}_{-3.8}$	0	0	$0.08^{+0.18}_{-0.06}$

Table 3.11: Some properties of the seven events found in data with the material interactions selection inverted.

Channel, year	$ d_0^a ,  d_0^b $ [ $\mu\text{m}$ ]	vertex position (x, y, z) [ cm ]
$e\mu$ 2017C	-14, -10 (A)	(-2.5, 1.4, 6.8) (BPIX L1)
$e\mu$ 2018D	46, -14 (A)	(0.9, 2.1, 0.1) (beampipe)
$ee$ 2018D	198, -34 (B)	(-1.9, 0.5, 2.7) (beampipe)
$\mu\mu$ 2016G	407, -8 (B)	(-1.4, 4.0, 6.3) (BPIX L1)
$\mu\mu$ 2016G	-17, -2215 (C)	(-2.6, 3.1, 6.6) (BPIX L1)
$\mu\mu$ 2016H	2, 0 (A)	(-1.6, -3.5, 12) (BPIX inner shield)
$\mu\mu$ 2017F	522, -13 (B)	(-1.1, -3.0, -7.5) (BPIX L1)

Table 3.12: Background estimates in data while applying the 2018  $\mu\mu$  preselection and the additional requirement of at least one medium  $b$ -tagged jet. The estimates with at least one  $b$  jet are about an order of magnitude below the nominal prediction.

	SR I	SR II	SR III	SR IV
2018 $\mu\mu$ preselection (corrected)	$2.6 \pm 1.0$	$0.09^{+0.12}_{-0.09}$	$0.05^{+0.07}_{-0.05}$	$0.007^{+0.010}_{-0.007}$
2018 $\mu\mu$ preselection + 1 $b$ jet	$0.19 \pm 0.03$	$0.008^{+0.007}_{-0.004}$	$0.005^{+0.004}_{-0.002}$	$0.0002^{+0.0002}_{-0.0001}$

Table 3.13: A closure test of the ABCD method in 2018 QCD simulation in the  $\mu\mu$  channel with the muon isolation criterion inverted. The estimates from the ABCD method, the actual yields in simulation, and the ratios of the actual to the estimated yields are shown.

Region	Estimated yield	Actual yield	Ratio of actual to estimate
SR I	$9500 \pm 1100$	$11000 \pm 1000$	$1.2 \pm 0.2$
SR II	$1740^{+310}_{-280}$	$2200^{+330}_{-290}$	$1.3 \pm 0.3$
SR III	$1450^{+280}_{-240}$	$1500^{+180}_{-160}$	$1.0 \pm 0.2$
SR IV	$265^{+62}_{-54}$	$268^{+61}_{-50}$	$1.0 \pm 0.3$

Table 3.14: The average  $\sigma_{align}$  for electrons and muons, for the 2017 and 2018 analyses.

	2017	2018
Electrons	$14.75 \pm 0.36 \mu\text{m}$	$9.18 \pm 0.41 \mu\text{m}$
Muons	$7.57 \pm 0.12 \mu\text{m}$	$8.11 \pm 0.08 \mu\text{m}$

Table 3.15: The unprescaled MET triggers used to create an orthogonal data sample for the trigger efficiency calculation.

---

<b>2016</b>
HLT_MET200
HLT_MonoCentralPFJet80_PFMETNoMu110_PFMHTNoMu110_IDTight
HLT_PFMET120_PFMHT120_IDTight
HLT_PFMET170_HBHECleaned
HLT_PFMET300
HLT_PFMETNoMu120_PFMHTNoMu120_IDTight
<b>2017</b>
HLT_CaloMET350_HBHECleaned
HLT_MonoCentralPFJet80_PFMETNoMu120_PFMHTNoMu120_IDTight
HLT_PFMET120_PFMHT120_IDTight
HLT_PFMET250_HBHECleaned
HLT_PFMETNoMu120_PFMHTNoMu120_IDTight
<b>2018</b>
HLT_CaloMET350_HBHECleaned
HLT_MonoCentralPFJet80_PFMETNoMu120_PFMHTNoMu120_IDTight
HLT_PFMET120_PFMHT120_IDTight
HLT_PFMET200_HBHE_BeamHaloCleaned
HLT_PFMET250_HBHECleaned
HLT_PFMETNoMu120_PFMHTNoMu120_IDTight

---

Table 3.16: Systematic uncertainties in the signal efficiency for all three years and the three channels. The mean is provided in cases where the uncertainty varies by signal sample. Uncertainties in the same row are treated as correlated among the years of data taking, except for the displaced tracking and muon pixel hit efficiencies, where the 2016 uncertainty is treated as uncorrelated with the 2017 and 2018 uncertainties.

Systematic uncertainty	2016	2017	2018
<i>Integrated luminosity</i>	1.8%	1.8%	1.8%
<i>Pileup</i>			
- $e\mu$ channel	0.5%	0.6%	0.5%
- ee channel	0.5%	0.9%	0.8%
- $\mu\mu$ channel	0.2%	0.1%	0.2%
<i>Displaced tracking efficiency</i>	14%	5.8%	2.4%
<i>Trigger efficiency</i>			
- $e\mu$ channel, electrons	1.6%	1.3%	1.2%
- $e\mu$ channel, muons	1.6%	1.4%	1.2%
- ee channel	10%	13%	19%
- $\mu\mu$ channel	1.2%	1.0%	1.1%
<i>Muon trigger efficiency at large <math> d_0 </math></i>			
- $e\mu$ channel, muons	20%	20%	20%
- $\mu\mu$ channel	20%	20%	20%
<i>Lepton identification and isolation</i>			
- $e\mu$ channel, electrons	1.2%	3.6%	3.5%
- $e\mu$ channel, muons	0.05%	0.07%	0.06%
- ee channel	2.4%	7.2%	7.0%
- $\mu\mu$ channel	0.10%	0.14%	0.12%
<i>Muon pixel hit efficiency</i>			
- $e\mu$ channel, muons	32%	12%	16%
- $\mu\mu$ channel	73%	23%	30%
<i>Lepton <math> d_0 </math> correction</i>			
- $e\mu$ channel, electrons	—	0.001%	0.001%
- $e\mu$ channel, muons	—	0.003%	0.001%
- ee channel	—	0.11%	0.11%
- $\mu\mu$ channel	—	0.11%	0.11%

Table 3.17: The number of estimated background and observed events in each channel and SR. For each estimate, the total uncertainty is given.

	SR I $p_T$ boundary [GeV]	SR I, low $p_T$ bin	SR I, high $p_T$ bin	SR II	SR III	SR IV
<i>2016 e<math>\mu</math></i>						
- estimated	90	$3.8^{+4.8}_{-3.8}$	$0.41^{+0.53}_{-0.41}$	$0.09^{+0.12}_{-0.09}$	$0.15 \pm 0.15$	$0.003^{+0.004}_{-0.003}$
- observed	90	8	1	0	0	0
<i>2017+2018 e<math>\mu</math></i>						
- estimated	140	$38 \pm 13$	$0.75^{+0.41}_{-0.34}$	$0.23^{+0.27}_{-0.23}$	$0.71^{+0.76}_{-0.71}$	$0.01^{+0.02}_{-0.01}$
- observed	140	28	3	0	1	0
<i>2016 ee</i>						
- estimated	300	$18 \pm 11$	$0.22^{+0.17}_{-0.16}$	$0.51^{+1.02}_{-0.51}$	$0.43^{+0.85}_{-0.43}$	$0.01^{+0.02}_{-0.01}$
- observed	300	40	0	0	1	0
<i>2017+2018 ee</i>						
- estimated	400	$62^{+18}_{-17}$	$0.85^{+0.33}_{-0.35}$	$2.8 \pm 1.1$	$3.6 \pm 1.4$	$0.24^{+0.10}_{-0.09}$
- observed	400	48	0	1	4	0
<i>2016 <math>\mu\mu</math></i>						
- estimated	100	$7.4 \pm 3.0$	$0.25 \pm 0.11$	$0.17 \pm 0.11$	$0.19 \pm 0.12$	$0.01 \pm 0.01$
- observed	100	15	0	0	1	0
<i>2017+2018 <math>\mu\mu</math></i>						
- estimated	100	$3.5 \pm 1.5$	$0.69 \pm 0.31$	$0.08^{+0.12}_{-0.08}$	$0.14^{+0.19}_{-0.14}$	$0.01^{+0.02}_{-0.01}$
- observed	100	1	1	1	1	0

Table 3.18: The pre- and post-fit predictions for each signal region bin.

	SR I, low $p_T$ bin	SR I, high $p_T$ bin	SR II	SR III	SR IV
<i>2016 e<math>\mu</math></i>					
- pre-fit prediction	$3.8 \pm 3.9$	$0.40 \pm 0.45$	$0.09 \pm 0.11$	$0.15 \pm 0.13$	$0.003 \pm 0.003$
- post-fit prediction	$7.1 \pm 2.0$	$0.76 \pm 0.31$	$0.08 \pm 0.08$	$0.14 \pm 0.14$	$0.003 \pm 0.003$
<i>2017+2018 e<math>\mu</math></i>					
- pre-fit prediction	$38 \pm 14$	$0.75 \pm 0.40$	$0.23 \pm 0.37$	$0.71 \pm 0.90$	$0.01 \pm 0.02$
- post-fit prediction	$31 \pm 5$	$0.68 \pm 0.25$	$0.20 \pm 0.17$	$0.65 \pm 0.48$	$0.01 \pm 0.01$
<i>2016 ee</i>					
- pre-fit prediction	$18 \pm 11$	$0.22 \pm 0.17$	$0.51 \pm 2.41$	$0.43 \pm 2.06$	$0.01 \pm 0.06$
- post-fit prediction	$35 \pm 5$	$0.40 \pm 0.14$	$0.50 \pm 0.75$	$0.44 \pm 0.53$	$0.01 \pm 0.02$
<i>2017+2018 ee</i>					
- pre-fit prediction	$62 \pm 17$	$0.85 \pm 0.31$	$2.8 \pm 0.9$	$3.6 \pm 1.2$	$0.25 \pm 0.09$
- post-fit prediction	$50 \pm 6$	$0.65 \pm 0.19$	$2.5 \pm 0.7$	$3.2 \pm 0.9$	$0.22 \pm 0.06$
<i>2016 <math>\mu\mu</math></i>					
- pre-fit prediction	$7.4 \pm 3.3$	$0.25 \pm 0.11$	$0.17 \pm 0.11$	$0.19 \pm 0.12$	$0.01 \pm 0.01$
- post-fit prediction	$11 \pm 2$	$0.37 \pm 0.10$	$0.19 \pm 0.10$	$0.21 \pm 0.12$	$0.01 \pm 0.01$
<i>2017+2018 <math>\mu\mu</math></i>					
- pre-fit prediction	$3.4 \pm 1.6$	$0.69 \pm 0.32$	$0.08 \pm 0.12$	$0.14 \pm 0.18$	$0.01 \pm 0.02$
- post-fit prediction	$2.5 \pm 1.1$	$0.51 \pm 0.22$	$0.14 \pm 0.36$	$0.23 \pm 0.63$	$0.02 \pm 0.05$

## **Chapter 4: Conclusion**

## **Appendix A: Impact of APV saturation on displaced tracking**

## Appendix B: Poorly measured lepton $|d_0|$ at large $|\eta|$

We require muons to have  $|\eta| < 1.5$  due to the observed increase in width of the muon  $d_0$  distribution at large  $|\eta|$  in DY simulation with  $Z \rightarrow \tau\tau \rightarrow ll$  events removed (see Fig. B.1 (left)). The width visibly increases at large  $|\eta|$  in all three years but is less pronounced in 2017 and 2018 due to the improved performance of the Phase 1 pixel detector. The upgraded pixel detector is also responsible for the overall difference in  $d_0$  width between years. Requiring muon  $|\eta| < 1.5$  has two effects: (1) it dramatically reduces the mismeasurement background in 2016 data in the  $\mu\mu$  channel, and (2) it removes a possible source of  $|d_0^a| - |d_0^b|$  correlation in which the correlation between muons in  $\eta$  leads to correlation between muons in  $|d_0|$ . As shown in Fig. B.1 (right), muons from  $\tilde{t}\tilde{t} \rightarrow \bar{l}b \bar{l}b$  events tend to have small  $|\eta|$ , so requiring muon  $|\eta| < 1.5$  has a minimal effect on the signal acceptance.

Electron  $d_0$  resolution also worsens at large  $|\eta|$ . Furthermore, Fig. B.2 (left) shows that electrons from SM mesons are particularly concentrated  $|\eta| > 1.5$ . As in the muon case, electrons from  $\tilde{t}\tilde{t} \rightarrow \bar{l}b \bar{l}b$  events tend to have  $|\eta| < 1.5$  (see Fig. B.2), which implies that requirement electron  $|\eta| < 1.5$  will reduce the mismeasurement and SM meson backgrounds without significantly reducing signal acceptance.

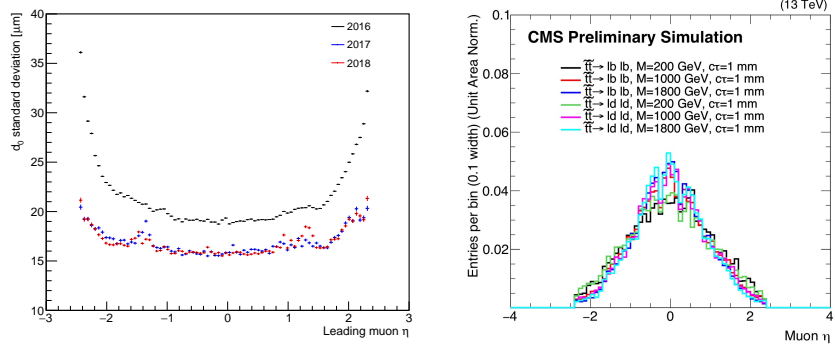


Figure B.1: Left: The standard deviation of the leading muon  $d_0$  as a function of the leading muon  $\eta$  for simulated background events. To ensure that the variation in width is purely due to  $d_0$  resolution effects, we use a sample of simulated DY events from which the  $Z \rightarrow \tau\tau \rightarrow ll$  events have been removed. Right: Muon  $\eta$  distribution for simulated  $t\bar{t} \rightarrow l\bar{b} l\bar{b}$  events. The  $\mu\mu$  preselection with a loosened  $|\eta|$  requirement is applied in both plots.

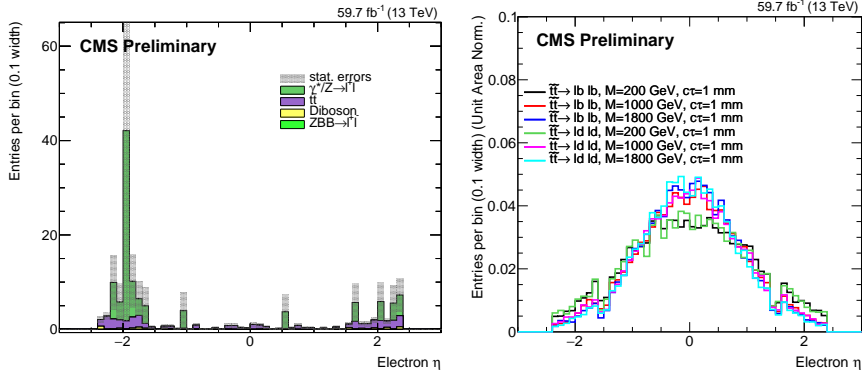


Figure B.2: Left: electron  $\eta$  distribution for simulated background events in which the electron parent particles are required to be SM mesons. Right: Electron  $\eta$  distribution for simulated  $t\bar{t} \rightarrow l\bar{b} l\bar{b}$  events. The  $e\mu$  preselection with a loosened  $\eta$  requirement is applied in both plots.

## **Appendix C: Displaced tracking efficiency**

## Bibliography

- [1] Cms collaboration. <https://cms.cern/collaboration>. Accessed: 2021-03-28.
- [2] Proton Synchrotron. 1959.
- [3] Linear accelerator 2. Sep 2012.
- [4] The Proton Synchrotron Booster. Jul 2012.
- [5] The Super Proton Synchrotron. Jan 2012.
- [6] Georges Aad et al. Observation of a new particle in the search for the standard model Higgs boson with the ATLAS detector at the LHC. *PLB*, 716:1, 2012.
- [7] W. Adam. The CMS Phase-1 Pixel Detector Upgrade. *JINST*, 16(02):P02027, 2021.
- [8] W Adam, R Frühwirth, A Strandlie, and T Todorov. Reconstruction of electrons with the gaussian-sum filter in the CMS tracker at the LHC. *Journal of Physics G: Nuclear and Particle Physics*, 31(9):N9–N20, jul 2005.
- [9] Simone Alioli, Paolo Nason, Carlo Oleari, and Emanuele Re. NLO vector-boson production matched with shower in POWHEG. *JHEP*, 07:060, 2008.
- [10] Simone Alioli, Paolo Nason, Carlo Oleari, and Emanuele Re. A general framework for implementing NLO calculations in shower Monte Carlo programs: the POWHEG BOX. *JHEP*, 06:043, 2010.
- [11] B.C. Allanach, M. Battaglia, G.A. Blair, Marcela S. Carena, A. De Roeck, et al. The Snowmass points and slopes: Benchmarks for SUSY searches. *EPJC*, 25:113, 2002.
- [12] J. Alwall, R. Frederix, S. Frixione, V. Hirschi, F. Maltoni, O. Mattelaer, H. S. Shao, T. Stelzer, P. Torrielli, and M. Zaro. The automated computation of tree-level and next-to-leading order differential cross sections, and their matching to parton shower simulations. *JHEP*, 07:079, 2014.

- [13] Johan Alwall, A. Ballestrero, P. Bartalini, S. Belov, E. Boos, et al. A standard format for Les Houches event files. *Comput. Phys. Commun.*, 176:300, 2007.
- [14] Johan Alwall et al. Comparative study of various algorithms for the merging of parton showers and matrix elements in hadronic collisions. *Eur. Phys. J. C*, 53:473, 2008.
- [15] G. L. Bayatian et al. CMS Physics: Technical Design Report Volume 1: Detector Performance and Software. 2006. There is an error on cover due to a technical problem for some items.
- [16] G. L. Bayatian et al. CMS Physics: Technical Design Report Volume 2: Physics Performance. *J. Phys. G*, 34(CERN-LHCC-2006-021. CMS-TDR-8-2):995–1579. 669 p, 2007. revised version submitted on 2006-09-22 17:44:47.
- [17] L. Cadamuro. The cms level-1 trigger system for lhc run ii. *Journal of Instrumentation*, 12(03):C03021, 2017.
- [18] Serguei Chatrchyan et al. The CMS experiment at the CERN LHC. The Compact Muon Solenoid experiment. *JINST*, 3:S08004. 361 p, 2008. Also published by CERN Geneva in 2010.
- [19] Serguei Chatrchyan et al. Observation of a new boson at a mass of 125 GeV with the CMS experiment at the LHC. *PLB*, 716:30, 2012.
- [20] CMS Collaboration. Search for displaced leptons in the e-mu channel. *CMS-PAS-EXO-16-022*, 2016.
- [21] CMS Collaboration. CMS luminosity measurements for the 2016 data taking period. CMS Physics Analysis Summary CMS-PAS-LUM-17-001, 2017.
- [22] CMS Collaboration. CMS luminosity measurements for the 2017 data-taking period at  $\sqrt{s} = 13$  TeV. CMS Physics Analysis Summary CMS-PAS-LUM-17-004, 2018.
- [23] CMS Collaboration. CMS luminosity measurements for the 2018 data-taking period at  $\sqrt{s} = 13$  TeV. CMS Physics Analysis Summary CMS-PAS-LUM-18-002, 2018.
- [24] CMS Collaboration. Precision measurement of the structure of the CMS inner tracking system using nuclear interactions with data collected in 2018. *CMS-DP-2019-001*, 2019.
- [25] Glen Cowan, Kyle Cranmer, Eilam Gross, and Ofer Vitells. Asymptotic formulae for likelihood-based tests of new physics. *Eur. Phys. J. C*, 71:1554, 2011.

- [26] A et al. Dominguez. CMS Technical Design Report for the Pixel Detector Upgrade. Technical Report CERN-LHCC-2012-016. CMS-TDR-11, Sep 2012. Additional contacts: Jeffrey Spalding, Fermilab, Jeffrey.Spalding@cern.ch Didier Contardo, Universite Claude Bernard-Lyon I, didier.claude.contardo@cern.ch.
- [27] EGamma POG. Cut Based Electron ID for Run 2, Tight Electron. <https://twiki.cern.ch/twiki/bin/view/CMS/CutBasedElectronIdentificationRun2>.
- [28] F. Englert and R. Brout. Broken symmetry and the mass of gauge vector mesons. *Phys. Rev. Lett.*, 13:321–323, Aug 1964.
- [29] Jared A. Evans and Jessie Shelton. Long-lived staus and displaced leptons at the LHC. *JHEP*, 04:056, 2016.
- [30] Lyndon Evans and Philip Bryant. LHC machine. *Journal of Instrumentation*, 3(08):S08001–S08001, aug 2008.
- [31] Rikkert Frederix and Stefano Frixione. Merging meets matching in MC@NLO. *JHEP*, 12:061, 2012.
- [32] Stefano Frixione, Paolo Nason, and Carlo Oleari. Matching NLO QCD computations with Parton Shower simulations: the POWHEG method. *JHEP*, 11:070, 2007.
- [33] Stefano Frixione and Bryan R. Webber. Matching NLO QCD computations and parton shower simulations. *JHEP*, 06:029, 2002.
- [34] Jeffrey Goldstone, Abdus Salam, and Steven Weinberg. Broken symmetries. *Phys. Rev.*, 127:965–970, Aug 1962.
- [35] G. S. Guralnik, C. R. Hagen, and T. W. B. Kibble. Global conservation laws and massless particles. *Phys. Rev. Lett.*, 13:585–587, Nov 1964.
- [36] Peter Ware Higgs. Broken symmetries, massless particles and gauge fields. *Phys. Lett.*, 12:132–133, 1964.
- [37] Thomas Junk. Confidence level computation for combining searches with small statistics. *Nucl. Instrum. Meth. A*, 434:435, 1999.
- [38] Vardan Khachatryan et al. Event generator tunes obtained from underlying event and multiparton scattering measurements. *Eur. Phys. J.*, C76(3):155, 2016.
- [39] Lumi POG. Luminosity POG Twiki. <https://twiki.cern.ch/twiki/bin/view/CMS/TWikiLUM#LumiComb>.
- [40] Esma Mobs. The CERN accelerator complex - 2019. Complexe des accélérateurs du CERN - 2019. Jul 2019. General Photo.

- [41] Muon POG. Baseline muon selections for Run-II, Tight Muon. [https://twiki.cern.ch/twiki/bin/view/CMS/SWGuideMuonIdRun2#Tight\\_Muon](https://twiki.cern.ch/twiki/bin/view/CMS/SWGuideMuonIdRun2#Tight_Muon).
- [42] Paolo Nason. A New method for combining NLO QCD with shower Monte Carlo algorithms. *JHEP*, 11:040, 2004.
- [43] A. L. Read. Presentation of search results: the  $CL_s$  technique. In *Durham IPPP Workshop: Advanced Statistical Techniques in Particle Physics*, page 2693, Durham, UK, March 2002. [J. Phys. G 28 (2002) 2693].
- [44] Tai Sakuma. 3D SketchUp images of the CMS detector (120918). May 2016.
- [45] Albert M Sirunyan et al. Particle-flow reconstruction and global event description with the CMS detector. *JINST*, 12:P10003, 2017.
- [46] Albert M Sirunyan et al. Measurement of the inelastic proton-proton cross section at  $\sqrt{s} = 13$  TeV. *JHEP*, 07:161, 2018.
- [47] Albert M Sirunyan et al. Precision measurement of the structure of the CMS inner tracking system using nuclear interactions. *JINST*, 13:P10034, 2018.
- [48] Albert M Sirunyan et al. Extraction and validation of a new set of CMS PYTHIA8 tunes from underlying-event measurements. *EPJC*, 80:4, 2020.
- [49] Albert M Sirunyan et al. Search for disappearing tracks in proton-proton collisions at  $\sqrt{s} = 13$  TeV. *PLB*, 806:135502, 2020.
- [50] A.M. Sirunyan, A. Tumasyan, W. Adam, F. Ambrogi, E. Asilar, T. Bergauer, J. Brandstetter, E. Brondolin, M. Dragicevic, J. Erö, and et al. Performance of the cms muon detector and muon reconstruction with proton-proton collisions at  $\sqrt{s} = 13$  tev. *Journal of Instrumentation*, 13(06):P06015–P06015, Jun 2018.
- [51] Torbjörn Sjöstrand, Stefan Ask, Jesper R. Christiansen, Richard Corke, Nishita Desai, Philip Ilten, Stephen Mrenna, Stefan Prestel, Christine O. Rasmussen, and Peter Z. Skands. An introduction to PYTHIA 8.2. *Comput. Phys. Commun.*, 191:159, 2015.
- [52] AC Team. Diagram of an LHC dipole magnet. Schéma d'un aimant dipôle du LHC. Jun 1999.
- [53] The ATLAS Collaboration, The CMS Collaboration, The LHC Higgs Combination Group. Procedure for the LHC Higgs boson search combination in Summer 2011. Technical Report CMS-NOTE-2011-005, ATL-PHYS-PUB-2011-11, 2011.
- [54] Jorg Wenninger. Operation and Configuration of the LHC in Run 2. Mar 2019.